Universidad Politécnica de Madrid

Escuela Técnica Superior de Ingenieros de Caminos, Canales y Puertos

Fatigue behavior and fatigue crack initiation micromechanisms of rolled AZ31 Mg alloy

TESIS DOCTORAL

SeyedAbbas Jamali

Ingeniero Materiales

Supervised by

Professor Francisco Javier LLorca Martinez

Doctor Anxin Ma

2023

UNIVERSIDAD POLITECNICA DE MADRID

Tribunal nombrado por el Mgfco. y Excmo. Sr. Rector de la Universidad Politécnica de Madrid, el día ___ de ___, de 2023.

Presidente D. _____

Vocal D. _____

Vocal D. _____

Vocal D. _____

Secretario D. _____

Realizado el acto de defensa y lectura de la Tesis el día ..... de ..... de 2023

en la *E.T.S. de Ingenieros de Caminos, Canales y Puertos de la U.P.M.*

Calificación: .....

EL PRESIDENTE LOS VOCALES

EL SECRETARIO

Departamento de Ciencia de Materiales

Escuela Técnica Superior de Ingenieros de Caminos,

Canales y Puertos

Universidad Politécnica de Madrid

Fatigue behavior and fatigue crack initiation micromechanisms of rolled AZ31 Mg alloy

TESIS DOCTORAL

SeyedAbbas Jamali

Ingeniero Materiales

Directores de Tesis

Prof. Javier LLorca

Universidad Politécnica de Madrid & IMDEA Materials Institute

Dr. Anxin Ma

IMDEA Materials Institute

2023

ACKNOWLEDGMENTS

I would like to dedicate a few words to those who made this study possible during my stay at the IMDEA Materials Institute.

Firstly, I sincerely thank Professor Javier Llorca and Dr. Anxin Ma for their constant trust and incommensurable patience.

Secondly, I also want to acknowledge Dr. Manuel Avella, Dr. Vanesa Martinez, José Luis Jiménez, Amalia San Roman, and Miguel De La Cruz for their time and assistance with the equipment.

I want to thank my friends and family for always being there when I needed them and encouraging me every day. Without their support, this work would not be possible.

I desire to make a passionate mention to my parents. I want to thank them for helping me to be the good person I am today, guiding me in the worst moments, and showing me never to back down.

Above all, I would like to thank my wife Sahar for her love and constant support, for all the late nights and early mornings, and for keeping me sane over the past few months. Thank you for being my muse, editor, proofreader, and sounding board. But most of all, thank you for being my best friend. I owe you everything. I hope you are proud of me. My success is yours, and this work is for you.

RESUMEN

Las aleaciones de Mg son populares en las industrias automotriz y aeroespacial debido a su ligereza y alta rigidez específica. Se utilizan en carcasas, cubiertas, piezas de acabado y secciones de carga, y como resultado, su comportamiento ante la fatiga es crítico para su rendimiento óptimo. Estudios anteriores sobre el comportamiento de la fatiga de las aleaciones de Mg no proporcionaron un análisis estadístico confiable del efecto de los mecanismos de deformación dominantes, incluyendo el deslizamiento basal, el maclado/desmaclado y el deslizamiento piramidal, en la iniciación de grietas de fatiga. Además, utilizar esta información para predecir la vida útil de la fatiga de las aleaciones de Mg a partir de los parámetros indicadores de fatiga aún no ha sido explorado.

En este trabajo se estudió el comportamiento de la fatiga de una aleación de Mg AZ31B-O con fuerte textura basal sometida a deformación cíclica totalmente invertida a lo largo de las direcciones de laminación, normal y a 45° entre las direcciones de laminación y normal a $\Delta\varepsilon/2 = 0.4\%$, 0.8% y 2%. Las muestras fueron deformadas en tres orientaciones que condujeron a curvas de esfuerzo-deformación cíclicas simétricas y no simétricas debido a la activación de diferentes mecanismos de deformación. Se realizaron pruebas de fatiga interrumpidas para obtener resultados estadísticamente significativos sobre los mecanismos de deformación e iniciación de grietas de fatiga. Los resultados mostraron que las grietas de fatiga más dañinas se nucleaban a lo largo de las maclas en granos grandes si los mecanismos de deformación dominantes eran el deslizamiento basal y el maclado/desmaclado a tracción. Además, las grietas de fatiga más largas se nucleaban a lo largo de bandas de deslizamiento piramidal en granos grandes si los principales mecanismos de deformación eran el maclado/desmaclado a tracción y el deslizamiento piramidal. Las grietas en los límites de grano alrededor de los granos pequeños estaban presentes pero no eran críticas para la falla por fatiga.

En paralelo, se simuló la respuesta mecánica de la aleación de magnesio AZ31 mediante homogeneización computacional en tres orientaciones. Se utilizó un modelo fenomenológico de plasticidad cristalina para modelar el comportamiento de los granos de Mg, teniendo en cuenta el deslizamiento basal, prismático y piramidal (incluyendo endurecimiento isotrópico y cinemático) y el maclado. Los parámetros del modelo se

calibraron utilizando las curvas de esfuerzo-deformación cíclicas a diferentes amplitudes y orientaciones de deformación cíclica. Las simulaciones numéricas se utilizaron para comprender los mecanismos de deformación dominantes y predecir la vida útil de la fatiga a través de un parámetro indicador de fatiga basado en la acumulación de deformación plástica por distintos mecanismos en cada ciclo de fatiga.

ABSTRACT

Mg alloys are popular in automotive and aerospace industries due to their lightweight and high specific stiffness. They are used in casings, housings, trim pieces, and load-bearing sections, and as a result, their fatigue behavior is critical for their optimal performance. Previous studies on the fatigue behavior of Mg alloys did not provide a reliable statistical analysis of the effect of dominant deformation mechanisms, including basal slip, twinning/detwinning, and pyramidal slip, on fatigue crack initiation. Additionally, using this information to predict Mg alloys' fatigue life based on fatigue indicator parameters is still unexplored.

In this work, the fatigue behavior of a textured AZ31B-O Mg alloy subjected to fully-reversed cyclic deformation along the rolling, normal, and 45° between rolling and normal directions at $\Delta\varepsilon/2$ = 0.4%, 0.8%, and 2% was studied. Samples were deformed in three orientations leading to symmetric and non-symmetric cyclic stress-strain curves due to the activation of different deformation mechanisms. Interrupted fatigue tests were conducted to obtain statistically significant results about deformation and fatigue crack initiation mechanisms. Results showed that the most damaging fatigue cracks were nucleated along twins in large grains if the dominant deformation mechanisms were basal slip and tensile twinning/detwinning. Moreover, the longest fatigue cracks were nucleated along pyramidal slip bands in large grains if the main deformation mechanisms were tensile twinning/detwinning and pyramidal slip. Grain boundary cracks around small grains were present but not critical for fatigue failure.

Furthermore, the AZ31 magnesium alloy's mechanical response was simulated through computational homogenization in three orientations. A phenomenological crystal plasticity model was used to model the behavior of the Mg grains, accounting for basal, prismatic, and pyramidal slip (including isotropic and kinematic hardening) and twining. The model parameters were calibrated using the cyclic stress-strain curves at different cyclic strain amplitudes and orientations. Numerical simulations were used to understand the dominant deformation mechanisms and to predict the fatigue life through a fatigue indicator parameter based on the accumulated plastic shear strain in each fatigue cycle as a result of the different deformation mechanisms.

Contents

List of Figures

List of Tables

1. INTRODUCTION

1.1. Mg Alloys

Reduction of mass has recently become an important strategy in the automotive and aerospace sectors [1–3] due to the rising global energy consumption and growing awareness of human-caused pollution, such as CO2 emissions [1,4]. According to different reports, the fuel consumption of passenger vehicles can decrease by 6-8% for every 10% reduction in weight [5]. Mg and its alloys, the lightest structural metallic materials, are being increasingly considered in the automotive sector to reduce the weight of vehicles [6]. In addition, they are considered in the biomedical sector to manufacture biodegradable implants for bone tissue regeneration because of their excellent biocompatibility [7,8]. However, pure Mg cannot be used for structural applications due to its low strength and limited ductility and formability at low temperatures [9]. These properties can be improved by alloying with aluminum, zinc, manganese, and rare earth (RE) elements. Aluminum and zinc are used to increase strength. Zinc is superior in improving strength compared to aluminum. However, a mixture of zinc and aluminum is preferred because zinc decreases the corrosion resistance in Mg alloys [9]. The presence of RE enhances the mechanical properties of Mg due to their relatively high solubility at the eutectic temperature and the formation of precipitates like Mg_5RE (Gd, Y) [10,11].

Mg alloys with aluminum and zinc elements are designated with two letters, AZ, followed by two numbers referring to the nominal compositions of the alloying elements. Aluminum is the main alloying element in AZ alloys up to 9 wt. %. Zinc is added up to 1 wt. %. Increasing the aluminum content in the AZ series increases the material density to an average of 1.8 g/cm^3 and decreases the melting point. In addition, zinc does not change the c/a ratio of the Mg HCP (*hexagonal closed-pack*) lattice, while aluminum increases this ratio [12]. AZ31B is a commercially available Mg alloy that can be supplied in the as-cast, sheet, or as-extruded condition. The primary alloying elements of the alloy are aluminum (Al), zinc (Zn), and manganese (Mn). The Al and Zn serve to improve room temperature strength, while Mn facilitates grain refinement and improves corrosion

resistance by trapping iron [13]. The proportions of these elements are included in Table 1.1.

Table 1.1 – Alloying elements of Mg alloy AZ31B [13].

Alloying Element	Content (%)
Aluminum	2.5-3%
Zinc	0.7-1.3%
Manganese	0.2-1%
Magnesium	Balance

1.2. Deformation Mechanisms of Magnesium Alloys

The elastic modulus of Mg alloys at room temperature is ≈45 GPa [14], and the elastic constants of Mg lead to an almost isotropic behavior. The plastic deformation mechanisms in Mg alloys can be divided into dislocation slip and twinning. Slip is the sliding of crystal blocks over one other along definite crystallographic planes, called slip planes. Twinning is the plastic deformation mechanism that accommodates shear by lattice reorientation around a crystallographic plane associated with an eigenstrain. Each twinning system can be defined by the twinning plane and the shear direction. However, twinning is a polar mechanism that allows shear in only one direction.

A summary of the common slip and twin systems in Mg and its alloys is shown in Fig 1.1. The component of shear stress, resolved in the direction of slip, necessary to initiate slip along a crystallographic plane is denominated the critical resolved shear stress (CRSS). The CRSS for prismatic $\langle a \rangle$ (50-60 MPa) and pyramidal $\langle a \rangle$ and $\langle c+a \rangle$ slip (50-70 MPa) in Mg are much higher than that for basal $\langle a \rangle$ slip (0.5-10 MPa) at room temperature [15–17]. Therefore, basal $\langle a \rangle$ slip is the softest available slip mode in Mg alloys at room temperature and it is always present during plastic deformation. However, basal slip alone is not enough to accommodate the plastic deformation in Mg alloys because it does not provide the necessary slip systems to fulfil the von Mises or Taylor criterion for uniform deformation [18]. As a result, twinning, which is the softest available deformation mode after the basal slip in Mg alloys, will be activated.

Mg has two twinning modes, denominated $\{10\bar{1}2\}\langle 10\bar{1}1\rangle$ tensile and $\{10\bar{1}1\}\langle 10\bar{1}2\rangle$ compression twins. Tensile twinning ($\{10\bar{1}2\}\langle 10\bar{1}1\rangle$) is very easily activated at room temperature when applied stress causes to extend the c-axis of the Mg crystal because the CRSS for tension twinning (30 MPa) is much lower than pyramidal slip [17,19]. The occurrence of tension twins results in an 86° rotation of the c-axis toward the $\langle 1\bar{2}10\rangle$ axis [19–21], and compression twinning leads to a lattice reorientation of 56°±7° along the $\langle 1\bar{2}10\rangle$ axis [22]. It should be noted that the CRSS for compression twinning is much higher than that associated with other deformation mechanisms, and compression twins are not often found in Mg and its alloys.

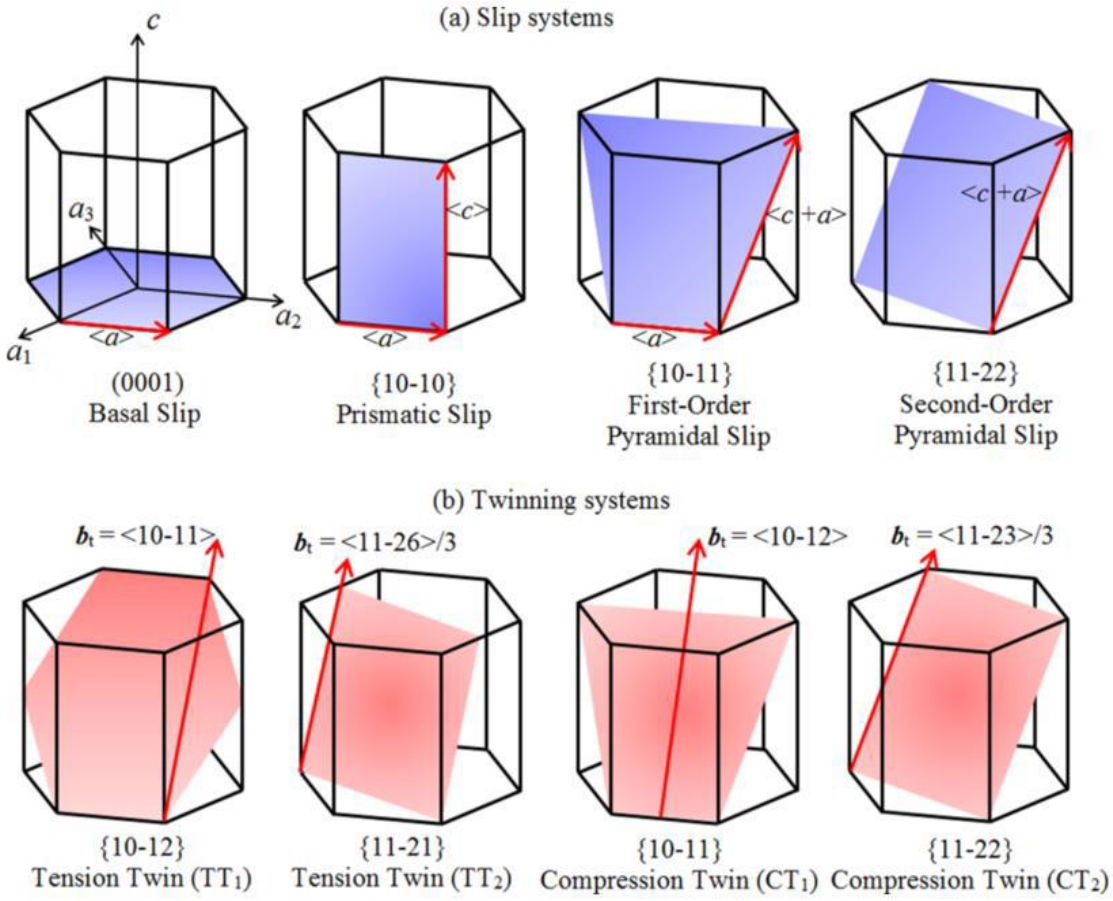

Figure 1.1 – Schematic illustration of slip and twinning systems in Mg alloys [23].

Thermo-mechanical processes (such as hot rolling or extrusion) result in a preferred HCP unit cell orientation or "*texture*" in wrought Mg alloys, with the c-axis typically aligned perpendicular to the deformation direction [24]. For example, extruded Mg alloy

displays a fiber texture such that the basal planes are aligned parallel to the extrusion direction [25]. Moreover, rolled Mg alloy shows a strong basal texture with the basal plane virtually parallel to the rolling direction [26]. As a result, either pyramidal slip or twinning has to be activated because the basal slip alone does not permit the accommodation of deformation along the c-axis in the HCP unit cell. Herrera-Solaz et al. [27] performed monotonic tensile and compression tests in different directions of a hot-rolled AZ31 Mg alloy with a thickness of 25.4 mm. The typical strong basal texture pole figure of the as-rolled material is illustrated in Fig. 1.2a (with *c* axis parallel to the normal direction), and the average grain size was 25 μm. Additionally, the prismatic poles spread along rolling and transverse directions. Samples for tension and compression tests were taken from the rolled plate in various orientations, as shown in Fig. 1.2b. The stress-strain curves in tension and compression in the normal direction (ND) and in tension in the rolling direction (RD), as well as the ones corresponding to the tensile tests in the RD-ND plane at 45° from both orientations, are plotted in Fig. 1.2c. These curves demonstrate the Mg alloys show a large plastic anisotropy, which is brought about by the limited number of slip systems and the polar nature of extension twinning, which is only active when deformation causes the c-axis to extend. As a result, tensile twinning cannot be activated when the specimen is loaded in tension along the RD or compression along ND, and the high CRSS for pyramidal slip leads to a very high value of yield strength. In contrast, tensile twinning occurs at low stress in the samples loaded in tension along ND or the RD-ND plane at 45° from both orientations, leading to much lower yield strength. Thus, the deformation of wrought Mg alloys is noticeably dependent on the orientation and different slip systems [27]. These deformation mechanisms (basal slip, pyramidal slip, twinning) and texture development are responsible for the anisotropic mechanical response in compression and tension of wrought Mg alloys, which is shown in Fig. 1.2 [17,27,28].

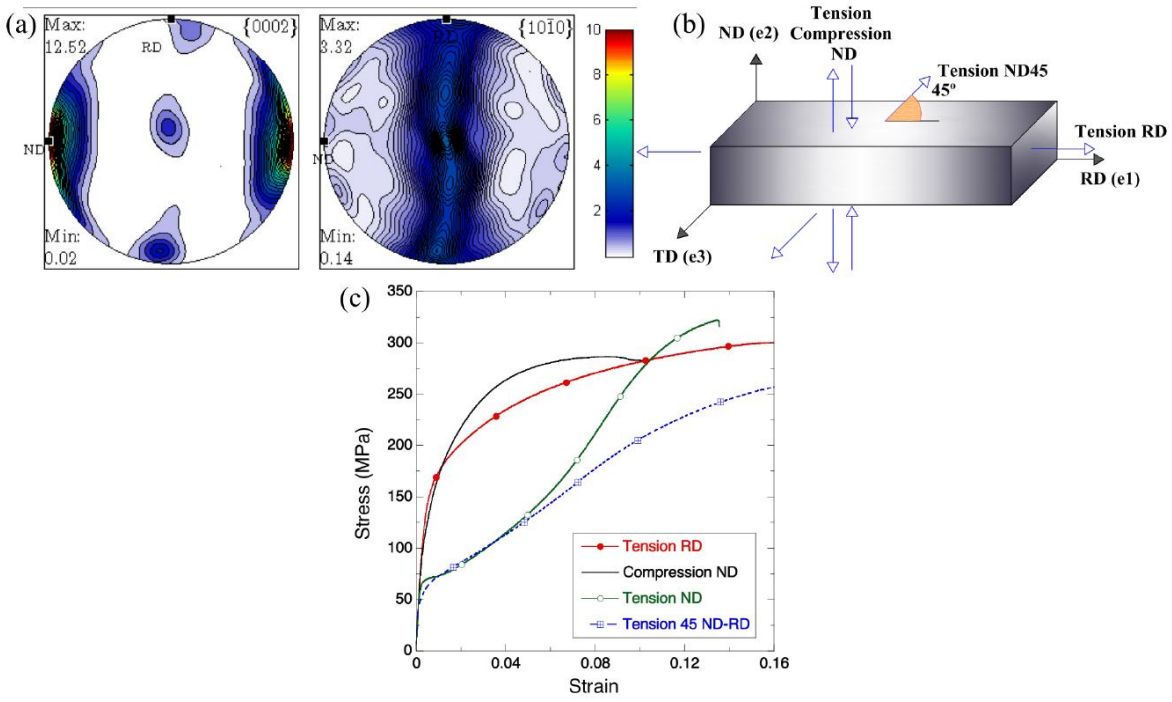

Figure 1.2 – (a) Pole figures of rolled AZ31 Mg alloy. (b) Schematic of the loading directions for the mechanical tests of the rolled plate of AZ31 Mg alloy. (c) The stress-strain curves of the rolled AZ31 Mg alloy along different orientations show plastic anisotropy [27].

1.3. Fatigue Behavior of Magnesium Alloys

The mechanical behavior of Mg alloys during cyclic deformation is essential to ensure the performance of Mg components that will have to support cyclic loads in cars and airplanes, leading to fatigue failure [29–31]. Fabrication of cast and wrought Mg components with enhanced fatigue behavior is essential due to the considerable increase in the use of Mg alloys in the engines, powertrain, chassis, and body regions [31–33]. Therefore, the most recent studies on the fatigue behavior of the as-cast and wrought Mg alloys will be summarized and discussed in sections 1.3.1 and 1.3.2.

1.3.1. As-Cast Mg Alloys

The cyclic stress-strain curves in fatigue of as-cast Mg alloys at moderate strain amplitudes (≤1%) are shown in Fig. 1.3a. They are symmetric due to their random grain orientations [32,34,35], in contrast to the noticeably asymmetrical stress-strain curves of textured wrought Mg alloys [36–42]. It should be noted that some studies have reported

slightly asymmetric cyclic stress-strain curves for the cast Mg alloys due to the mild activity of twinning/detwinning when the strain amplitude is high (≥1%) [34,43].

Both {0001}<11$\bar{2}$0> basal slip and <10$\bar{1}$2> twinning are generally acknowledged as the two primary deformation mechanisms of cast Mg alloys at room temperature [44]. Cast Mg alloy experiences twinning/detwinning during cyclic deformation [32,45,46]. The twinned regions formed in the loading part will shrink, and in some cases, the twinned region disappears during unloading, a phenomenon commonly known as detwinning [47,48].

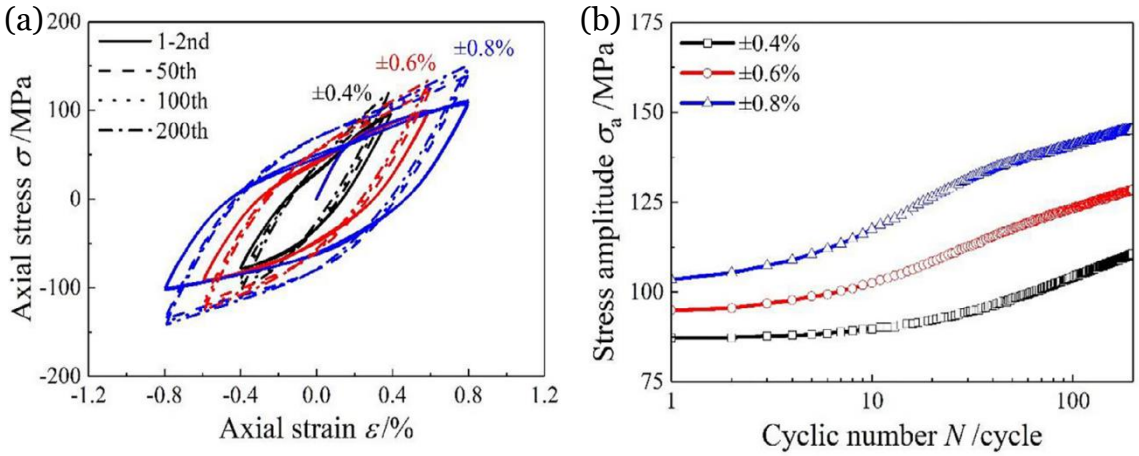

Figure 1.3 – (a) Hysteresis loops with different strain amplitudes, and (b) Evolution of tensile stress as a function of fatigue cycles at different strain amplitudes in the fatigue of as-cast AZ91 Mg alloy [32].

Apparent cyclic hardening with the number of fatigue cycles has been reported during fatigue of cast Mg alloys (Fig. 1.3b) [32,34,35]. The amount of cyclic hardening depends on the applied cyclic strain amplitude. Cyclic hardening is limited at relatively small strain semi-amplitudes ($\Delta\varepsilon/_2$ = 0.4%) because the main hardening mechanism is the interaction of basal dislocations with twins but full detwinning takes place during reversed deformation in each fatigue cycle (residual twins were hardly observed in the experiments). Detwinning does not occurs completely at higher values of the cyclic strain semi-amplitude, leading to more noticeable hardening due to the interaction of basal dislocations with residual twins that are gradually accumulated in the grains [32,49].

The fatigue life of as-cast Mg alloys is strongly related to the casting defects and microstructural features [50–54]. Casting defects act as stress concentration locations that nucleate fatigue cracks under cyclic loading and the largest casting defects determines the fatigue life of cast Mg alloys, like cast aluminum alloys [52–56]. However, the microstructural features (twin boundaries and persistent slip bands at or near the free surface of materials) have a significant impact on the fatigue life of cast Mg alloys when casting defects are smaller than a critical size or there are no casting defects [44,51,57–62]. Two kinds of fatigue crack nucleation features are found in as-cast Mg alloys when there are no casting defects. One feature is parallel lines on basal planes led by localization of basal slip, leading to the formation of persistent slip bands (PSBs), and another are lens-shaped, thicker defects, which are associated with the formation of twins [62]. Moreover, microcracks can be initiated within a surface grain since they deform plastically under low stresses due to the lack of constraints on the surface. Therefore, fatigue cracks of as-cast Mg alloys mostly nucleate from the free-surface or subsurface in the absence of casting defects or when the casting defect is smaller than a critical size [44,63]. It should be noted that there is no statistically reliable report on the fatigue crack initiation mechanisms of cast Mg alloys.

1.3.2. Wrought Magnesium Alloys

The fatigue behavior of wrought Mg alloys has received a lot of attention in recent years, i.e., AZ31 [30,64–66], AZ61 [67], AZ80 [68,69], AM30 [70,71], AM50 [72], AM60 [73], GW83 [74], ZA81M [75], and ZK60 [76]. Fully reversed ($R\varepsilon$=-1) strain-controlled low cycle fatigue (LCF) leads to high-stresses and low number of cycles to failure [64,65,76,77,66–69,71,72,74,75]. Under these conditions, wrought Mg alloys usually show a strong tension-compression asymmetry due to their strong basal texture (Figs. 1.4a, c), while wrought Mg alloys containing rare earth (RE) elements show limited tension-compression asymmetry due to their weak basal texture [74]. Basal slip and tensile twinning are the dominant deformation mechanisms in the tensile part of the cycle in wrought specimens with strong basal texture deformed along the ND or in compression along the RD (Figs. 1.4a, c). Detwinning mainly occurs during unloading and at the beginning of the compression along ND or tension along RD, and the deformation is controlled by <a> basal and <c+a> pyramidal slip at large strain amplitudes in these

conditions (Figs. 1.4, c) [65,68,85–87,76,78–84]. At low strain amplitudes, basal slip is enough to accommodate the plastic deformation and the asymmetry is more limited. Most twins formed during cyclic deformation will be removed when the load is reversed, but the residual twin volume fraction gradually increases with the number of cycles [47,88].

The tension-compression asymmetry decreases at low cyclic strain amplitudes because the activation of <c+a>pyramidal slip is limited because stresses are not enough to reach the CRSS for <c+a> pyramidal slip [30,36,65,67,68,83,89,90]. Moreover, it also decreases if the textured wrought Mg alloys are deformed under fully reversed cyclic deformation in an orientation between 20°-70° between rolling and normal directions [65,68], reaching a mean stress close to 0 at 45° [65]. In this orientation, plastic deformation takes place by basal slip and tensile twinning/detwinning during the tensile and compressive parts of the fatigue cycle. Similarly, the tension-compression asymmetry disappears in wrought Mg alloys with weak texture [91–93].

The evolution of the peak stress in tension and compression during fatigue of wrought Mg alloys for different cyclic strain amplitudes in Figs. 1.4b and 1.4d for specimens deformed along ND and RD, respectively. It has been shown that strongly textured AZ31 Mg alloy demonstrates cyclic hardening in both tension and compression for RD and ND conditions at room temperature. However, the cyclic hardening rate differs in compression and tension for RD and ND conditions (Fig. 1.4b, d) [80]. Specimens deformed along the ND direction show much larger cyclic hardening in the compressive peak stress than in the tensile peak stress, and the opposite behavior is found in the RD orientation [80]. The most likely explanation for this behavior is that the slip (basal and non-basal) mainly accommodates the deformation in these conditions, as a result, the interaction of slip and twinning is important.

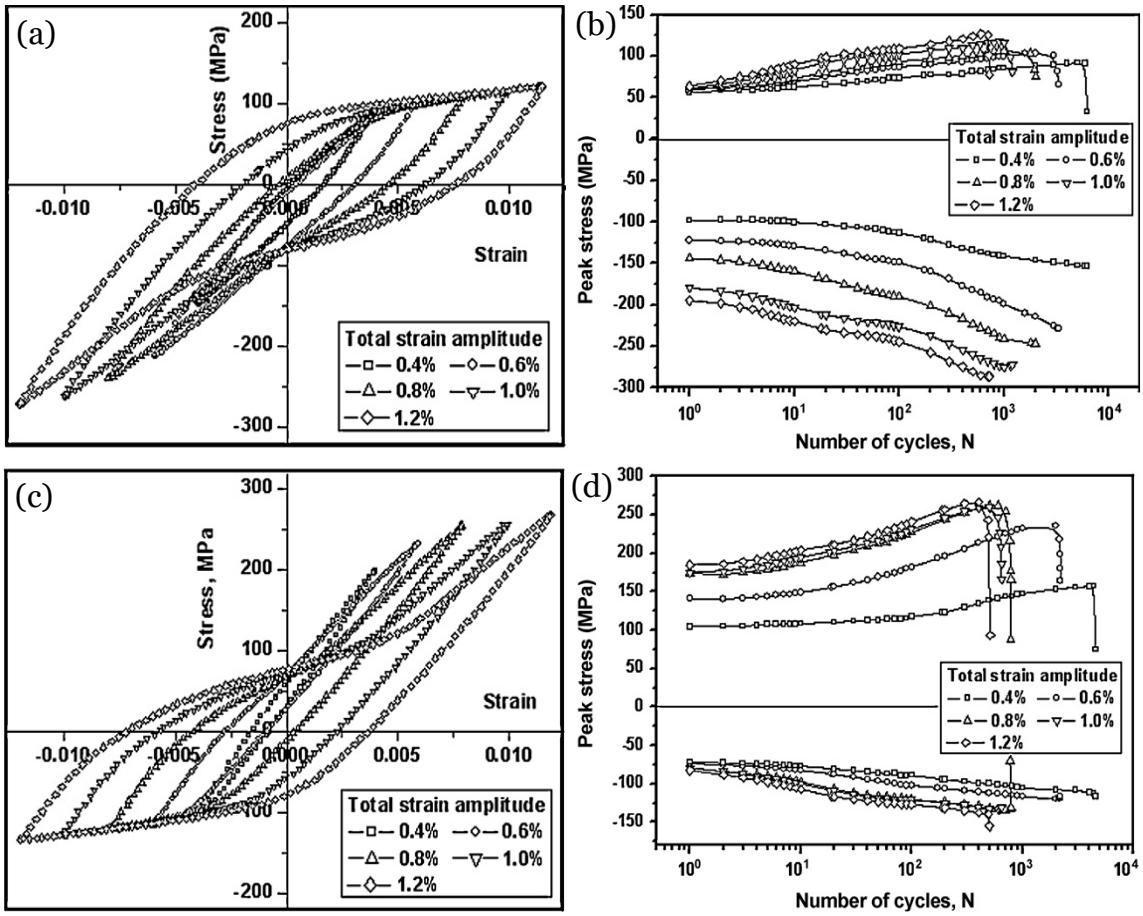

Figure 1.4 – (a) and (c) Stress-Strain hysteresis loops at half-life for rolled AZ31 Mg alloy for different cyclic strain amplitudes in specimens deformed along ND and RD. (b) and (c) Evolution of tensile and compressive peak stresses with the number of cycles for rolled AZ31 Mg alloy deformed along ND and RD at different cyclic strain amplitudes [80].

Obviously, the activation of different dominant deformation mechanisms as a function of texture, orientation, and strain amplitude has an important effect on the fatigue crack initiation mechanisms [89,90,92,94–98] and the fatigue life of wrought Mg alloys [65,68]. The experimental analyses indicate that fatigue cracks are nucleated at basal slip bands at low cyclic strain semi-amplitudes ($\Delta\varepsilon/2 \leq 0.5\%$) in textured Mg alloys deformed along the extrusion direction [89,90,94]. On the contrary, fatigue crack initiation is reported to switch to grain boundaries [90,92,94,98] and twins in these circumstances when the cyclic strain semi-amplitude increases. Other investigations have reported that fatigue cracks are nucleated around intermetallic particles [97]. Deng et al. [98] analyzed over 200 fatigue cracks nucleated in a weakly textured Mg – 3 wt. % Y alloy deformed at a cyclic strain semi-amplitude of 1% and found that 80% were nucleated at

grain boundaries while 20% were parallel to slip bands. More recently, Shi et al. [92] studied a limited number of fatigue cracks in specimens deformed along the RD, ND, and 45° RD-ND (29 cracks in RD, 27 cracks in ND, and 43 cracks in 45° RD-ND) in the RD-ND plane of a textured AZ31 Mg alloy deformed at a cyclic strain semi amplitude of 1%. They showed that intergranular cracking is the primary crack initiation mechanism along ND and 45° RD-ND, while transgranular cracking is dominant in RD [92].

The relationship between the fatigue life and the cyclic strain amplitude Δε of metallic materials under fully reversed strain-controlled cyclic loading can be described by the following three parameter equation [65]

$$\left(\frac{\Delta\varepsilon}{2} - \varepsilon_0\right)^{\xi} N_f = C \tag{1.1}$$

where $\Delta\varepsilon/2$ is the strain semi-amplitude, N_f is the number of loading cycles to failure, and ε_0, ξ, and C are constants determined by fitting the experimental data. However, this is not true in the case of textured wrought Mg alloys [36,65,82,99], as shown in Fig. 1.5a. It has been shown that there are two kink points in each $\Delta\varepsilon/2$-N_f curve of rolled AZ31 magnesium alloy (Fig. 1.5a) [65].

The kink points reflect changes in the dominant plastic deformation mechanisms during cyclic deformation as well as in the crack nucleation mechanisms. When $\Delta\varepsilon/2 < 0.4\%$, plastic deformation is controlled by basal slip without involving twinning-detwinning, and the stress-strain hysteresis loops are symmetric [65]. In addition, the fatigue life in this regime is much longer than at higher strain amplitudes ($\Delta\varepsilon/2 > 0.4\%$) due to the lower strain energy dissipation (because of the smaller area of the hysteresis loops) and the lower magnitude of the maximum tensile stress in each fatigue cycle due to activation of basal slip [36,65–67,69,77,82,99]. In the regime $0.4\% < \Delta\varepsilon/2 < 2\%$, twinning-detwinning occurs during cyclic deformation, leading to tension-compression asymmetry in the cyclic stress-strain curves. If $\Delta\varepsilon/2 > 2\%$, pyramidal slip is also active during cyclic deformation, and the fatigue life is < 100 cycles because of the higher magnitude of the maximum tensile stress in each fatigue cycle due to the activation of pyramidal slip [65,67,82,99].

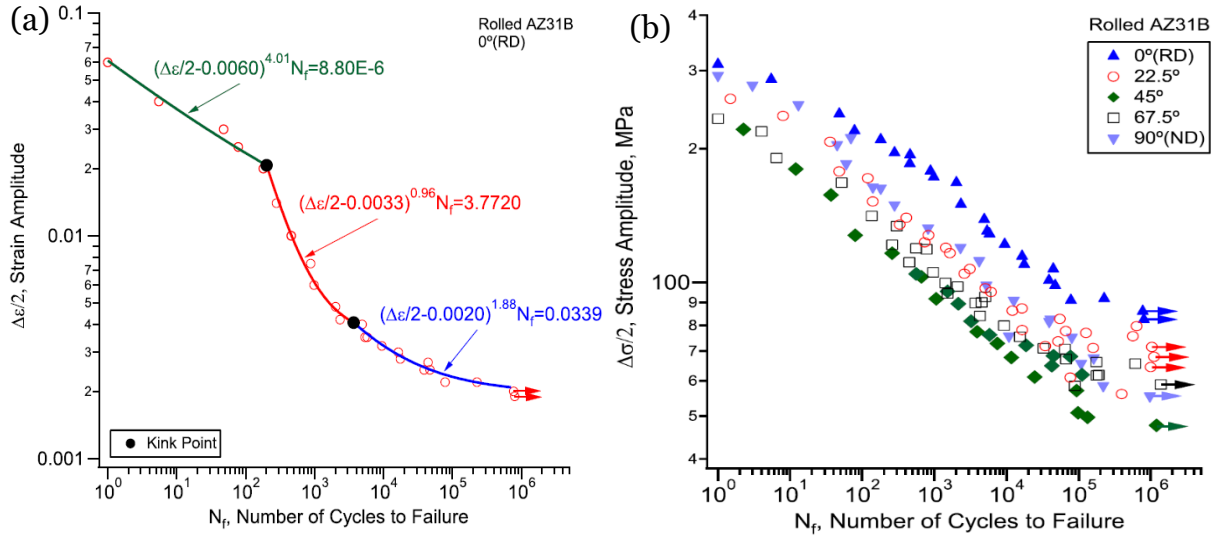

Figure 1.5 – (a) Fatigue life as a function of the cyclic strain amplitude for rolled AZ31B alloy deformed along the RD under fully reversed strain-controlled tension-compression, and (b) Fatigue life as a function of the stress semi-amplitude [65].

The effect of orientation on the fatigue life of rolled AZ31B Mg alloy under fully reversed strain-controlled condition is shown in Fig. 1.5b [65]. It is evident that the difference between fatigue life in RD and at 45° at $\Delta\sigma/2 = 100$ MPa is much higher (two orders of magnitude) compared to $\Delta\sigma/2 = 200$ MPa. The most likely explanation for this phenomenon is that $\Delta\sigma/2 = 100$ MPa is not enough to activate pyramidal slip, and in contrast, pyramidal slip will be active at $\Delta\sigma/2 = 200$ MPa, and as a result, the fatigue life will just reach hundreds of cycles.

In addition, it has been shown that the mean stress has a significant role in the fatigue life of extruded ZK60 Mg alloy under stress-controlled conditions [99]. For example, the fatigue life is > 10^5 cycles when the mean stress is compressive (σ_m= -200 MPa) and the stress semi-amplitude is almost 200 MPa, while the fatigue life is just hundreds of cycles (357 cycles) when the mean stress is tensile (σ_m = 90 MPa) due to activation of different fatigue deformation mechanisms [99]. Basal slip and twinning are the main deformation mechanisms in the fatigue of strongly textured as-extruded ZK60 Mg alloy when the mean stress is compressive, however, the pyramidal slip will be active when the mean stress is tensile.

In summary, changing the mean stress in stress-controlled fatigue or changing either orientation or strain amplitude in strain-controlled fatigue of textured wrought Mg alloys will result in considerable differences in the fatigue life due to the activation of different deformation mechanisms caused by their strong basal texture. Therefore, it is important to understand the link between the fatigue deformation mechanisms and the fatigue life in textured Mg alloys to design Mg alloys with optimum fatigue resistance.

1.4. Computational Homogenization

Physically based models of the mechanical behavior of materials are an essential tool for understanding the link between microstructure and mechanical properties. They allow a dramatic reduction in the time necessary to develop new materials with optimized properties for specific applications and a significant return of investment. Thus, there is a manifest interest in the scientific community and industry to improve and develop new multi-scale modeling strategies.

Homogenization theory is one of the most important tools to relate microstructure with effective properties in heterogeneous materials [100,101]. According to homogenization theory, the characteristic length scale of the microscopic domains—the average size of the heterogeneities—is much smaller than the characteristic length scale of the macroscopic sample and much larger than the molecular dimensions. As a result, continuum mechanics is applicable. The macroscopic or effective properties of the material under these circumstances can be determined by the geometrical features of the microstructure and the attributes of the various heterogeneities in the material. Following the pioneering work of Eshelby [102], different homogenization mean-field formulations were developed first for linear materials [103–106]. These techniques were further expanded through various linearization approximations to deal with nonlinear mechanical properties (nonlinear elasticity, plasticity, and viscoplasticity) [107–111].

However, there are two main limitations to the homogenization strategies based on mean-field approximations. First, these methods cannot account for local heterogeneities like clustering of grains with various sizes, shapes, and orientations, or accurately represent a specific misorientation distribution because these methods describe the

microstructure using average values for grain sizes, shapes, and orientations. While the impact of these local microstructural characteristics on properties that are dependent on the average values of the micromechanical fields, such as the elastic modulus, is frequently negligible, this is not the case for properties that are dependent on the extremal values (e.g., damage) [112–114]. Assuming that the micromechanical fields are constant throughout each phase results in the second limitation. It is hard to simulate processes in which these fields are confined in narrow bands in one or more phases/grains due to the plastic deformation, damage progression, low strain rate sensitivity (i.e., high nonlinearity), strong mechanical contrasts, etc. [115–117]. More advanced nonlinear homogenization techniques have been created to improve this second limitation in recent years, but at the expense of more complicated and costly numerical algorithms. These techniques use phase/grain level linearization schemes that also take into account information on the second moments of the field fluctuations in each phase and grain [118,119].

Full-field homogenization can be used to overcome the limitation of mean-field homogenization methods. This method solves a boundary value problem for a representative volume element (RVE) of the microstructure under homogeneous boundary conditions to find the effective properties of the polycrystal. It has been determined that three factors—the representation of the microstructure, the constitutive description of the single crystal behavior, and the numerical strategy to solve the boundary value problem—are necessary for the success and accuracy of computational homogenization approaches for polycrystals. The first criterion is that the size of the RVE must be large enough to lead to effective properties independent of the RVE dimensions and to offer an accurate statistical representation of the microstructure. The more complicated the single crystal constitutive behavior and the greater the RVE, the more expensive the calculation will be, necessitating quick and effective numerical methods to address the boundary value problem [91]. It should be noted that full-field homogenization has been traditionally carried out using the finite element method (FEM) to solve the governing partial differential equations (PDEs) of micromechanics in combination with the crystal plasticity (CP) formalism developed by Peirce et al. [120].

1.4.1. Representation of the Microstructure

Creating synthetic RVEs of the microstructure is the first step in the computational homogenization process. There are two approaches to define an RVE. It can be described as the smallest microstructure volume whose characteristics are identical to the effective properties of the heterogeneous solid (obtained using either homogeneous traction or displacement boundary conditions). Second, the RVE can be defined as the minimum volume of the microstructure whose statistical descriptors (which describe the characteristics of the heterogeneous microstructure) are equivalent to those found in the heterogeneous solid. The grain size and shape distribution, together with the orientation distribution function (ODF), which describes the crystallographic texture of the polycrystal, are the key characteristics that determine an RVE of a polycrystalline microstructure [88,91].

The RVE must be built as a digital model to carry out computational homogenization once all the data regarding the microstructure has been acquired. The RVEs can be created either by creating synthetic microstructures from the statistical descriptors defining the microstructure or by creating a one-to-one representation of an actual microstructure obtained via X-ray computed tomography or serial-sectioning data. The geometry of the RVE is usually defined using two distinct discretization types. The first one has the RVE divided into voxels, and the grains are made up of clusters of adjacent voxels with the same crystallographic orientation (Fig. 1.6.a). Voxel-based discretizations are the ideal choice for directly representing microstructures obtained by three-dimensional methods because they can be directly derived from the measured data. Additionally, voxel-based discretizations may be instantly exported into FEM as conventional hexahedral elements or as grid points for FFT-based algorithms.

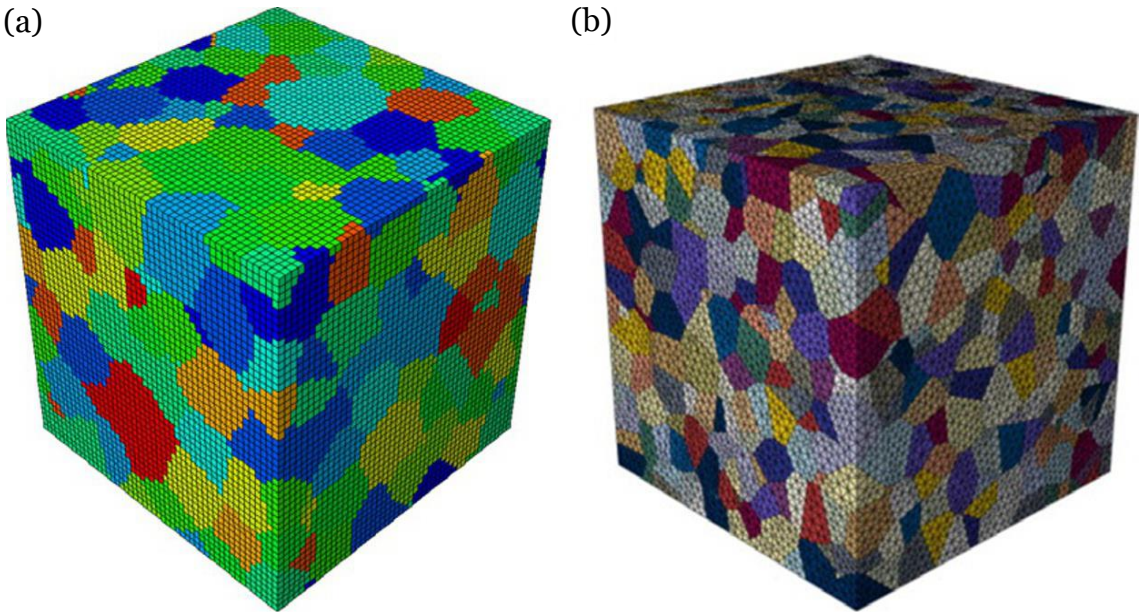

Figure 1.6 – Digital representation of an RVE of a polycrystal. (a) Voxel-based representation and (b) Voronoi-based representation [91]. Different colors stand for different grains.

However, there are two significant disadvantages for these voxel-based discretizations. First, because the grain boundaries are stepped surfaces, this representation cannot simulate phenomena localized at grain boundaries, such as grain boundary sliding. Second, because the voxel size is controlled by the dimensions of the smallest features that must be resolved within the RVE, the voxel-based FEM discretization frequently results in a very large number of elements. Representations of the grain structure based on Voronoi tessellation can be used to overcome these limitations (Fig. 1.6.b). In addition, weighted generalizations of the Voronoi model are often used due to the limitation of normal Voronoi tesselation to reproduce the actual grain size distribution. Therefore, the experimental grain size distribution (which can often be approximated by a log-normal function) is the starting point for the technique of constructing grain structures [88,91]. After implementing the grain size distribution in the RVE, the crystallographic texture can be introduced by assigning different orientations to the grains to reproduce the statistical distribution given by the ODF. The digital representation of the microstructure is an important and time-consuming task, and microstructure builders have been developed, such as Neper [121–123] and Dream3D [124]. They also provide tools to clean up the voxelized microstructures obtained from

tomography, serial-sectioning, or tessellation and to discretize the microstructure for full-field simulations [91].

1.4.2. Crystal Plasticity Model

Taylor and Elam [125,126] presented the first model that explained how crystallographic slip causes metallic single crystals to deform plastically. They studied the deformation of Al single crystals, which is described as the result of shear deformation along 12 slip systems, with the resolved shear stress on each slip system acting as the driving force for the shear deformation. A few years later, this model was used to study the deformation of a polycrystal as an aggregate of grains [127]. Hill [128] fitted Taylor's theories for the deformation of single crystals into the continuum mechanics framework for infinitesimal strains. In the early 1970s, Rice and Hill [129,130] expanded the theory based on the generic internal variable thermodynamic formalism to account for finite deformations. They used the advantage of Lee and Liu's [131] concept of the multiplicative decomposition of the deformation gradient into elastic and plastic parts. In the 1980s, many constitutive models for single crystals based on this framework were created employing viscoplasticity [132] or rate-independent formulations [120,133]. In parallel, the rigorous numerical implementations of the models were developed, including efficient and well-posed integration techniques for the highly nonlinear viscoplastic laws [134] and rigorous integration for the finite deformation framework [135].

In addition, another goal was to find an accurate description of the single crystal hardening evolution. The initial models were phenomenological [132,136], detailing how the cumulative shear strain changes the CRSS of various slip systems. More recently, using physically-based approaches, hardening was modeled from the material state variables, such as dislocation densities [136–138]. The choice between a hardening model that is phenomenological or microstructurally based is of minor importance because the main challenge in both scenarios is finding the quantitative values of the parameters experimentally to reproduce the plastic behavior of a specific single crystal.

The strain hardening model by Peirce et al. [139] only took into account isotropic hardening because it was designed for monotonic loading. The CRSS on each system included the explicit contributions of the slip in the same system (self-hardening) and the

slip on all the other slip systems (latent hardening). By including the effect of a backstress in the constitutive model to formulate kinematic hardening laws at the crystal level, this phenomenological framework is extended to account for cyclic deformation [140–142]. In the case of Mg alloys, plastic deformation will be accommodated by twinning when there are not enough slip systems for an arbitrary shape change of the crystal [143]. Hence, twinning was included in CP models to capture the monotonic mechanical behavior of Mg alloys [144,145]. In addition, the CP models were also incorporated with detwinning to accurately simulate cyclic loading in Mg alloys [146–149].

The standard multiplicative decomposition of the deformation gradient $\mathbf{F}$ into its elastic ($\mathbf{F}_e$) and plastic ($\mathbf{F}_p$) parts is generally the starting point of the crystal plasticity (CP) models [150].

$$\mathbf{F} = \mathbf{F}_e\mathbf{F}_p \tag{1.2}$$

where the initial configuration, the intermediate configuration as well as the current configuration are distinguished explicitly. The mapping from initial configuration to intermediate configuration by $\mathbf{F}_p$ dose not change the orientation of slip systems, while the mapping from the intermediate configuration to the current configuration through $\mathbf{F}_e$ contains the crystal rotation and the elastic deformation at the same time [129,130].

The plastic velocity gradient $\mathbf{L}_p$ in the intermediate configuration is the sum of $\mathbf{L}_p^{sl}$ and $\mathbf{L}_p^{tw}$ which are the contributions due to slip and twinning, respectively.

$$\mathbf{L}_p = \mathbf{L}_p^{sl} + \mathbf{L}_p^{tw}. \tag{1.3}$$

It should be noted that the plastic slip in the twinned regions of the crystal is unlikely to occur due to the continuous twinning-detwinning during cyclic deformation, therefore, it was not included in the model [47].

There are three (0001) <11$\bar{2}$0> basal, three {1$\bar{1}$00} <11$\bar{2}$0> prismatic and twelve {10$\bar{1}$1} <11$\bar{2}$3> pyramidal slip systems in Mg alloys which can accommodate the plastic deformation. Moreover, tensile twinning can occur along six {01$\bar{1}$2} <0$\bar{1}$11> twins

variants. The plastic velocity gradient can be contributed to the plastic slip with the following equation

$$\mathbf{L}_{\mathrm{p}}^{\mathrm{sl}} = (1 - \sum_{\beta=1}^{N_{tw}} f_{\beta}) \sum_{\alpha=1}^{N_{sl}} \dot{\gamma}_{\alpha}\, \hat{\boldsymbol{s}}_{\alpha}^{sl} \otimes \hat{\boldsymbol{m}}_{\alpha}^{sl} \tag{1.4}$$

where the unit vectors parallel to the slip direction and slip plane normal of slip system α in the reference configuration are $\hat{\boldsymbol{s}}_{\alpha}^{sl}$ and $\hat{\boldsymbol{m}}_{\alpha}^{sl}$, respectively. The volume fraction of twins corresponding to the twin system β is f_{β} and N_{sl} and N_{tw} stand for the number of slip and twin systems, respectively.

The plastic velocity gradient due to twining is given by

$$\mathbf{L}_{\mathrm{p}}^{\mathrm{tw}} = \sum_{\beta=1}^{N_{tw}} \dot{f}_{\beta}\, \gamma_{tw} \hat{\boldsymbol{s}}_{\beta}^{tw} \otimes \hat{\boldsymbol{m}}_{\beta}^{tw} \tag{1.5}$$

where the unit vectors parallel to the slip direction and slip plane normal of twin system β in the reference configuration are $\hat{\boldsymbol{s}}_{\beta}^{tw}$ and $\hat{\boldsymbol{m}}_{\beta}^{tw}$, respectively. The eigenstrain related to extension twinning in Mg alloys is 0.129 [27] and is given by γ_{tw}.

The slip rate in a slip system α can be defined by a power-law dependency expressed as

$$\dot{\gamma}_{\alpha} = \dot{\gamma}_{0} \left[\frac{\| \tau_{\alpha} - \tau_{\alpha}^{\mathrm{b}} \|}{g_{\alpha}} \right]^{\frac{1}{\mathrm{m}}} \mathrm{sign}(\tau_{\alpha} - \tau_{\alpha}^{\mathrm{b}}) \tag{1.6}$$

where $\tau_{\alpha}^{\mathrm{b}}$ and g_{α} are the kinematic and isotropic hardening contributions, respectively. The strain rate sensitivity exponent and the reference shear parameter are m and $\dot{\gamma}_{0}$, respectively.

The resolved shear stress τ_{α} of slip system α can be defined by the projection of the second Piola-Kirchhoff stress $\hat{\mathbf{S}}$ defined in the intermediate configuration, on the slip system or twin system α as

$$\tau_{\alpha} = \mathbf{S} : (\hat{\boldsymbol{s}}_{\alpha}^{sl} \otimes \hat{\boldsymbol{m}}_{\alpha}^{sl}). \tag{1.7}$$

The evolution law of isotropic hardening can be given by [144]

$$\dot{g}_\alpha = \sum_{\gamma=1}^{N_{sl}} h'_{\alpha\gamma} H_\gamma \left(1 - \frac{g_\gamma}{g_\gamma^{sat}}\right)^{a_{ss}} |\dot{\gamma}_\gamma| + \sum_{\beta=1}^{N_{tw}} h''_{\alpha\beta} H_\beta \left(1 - \frac{g_\beta}{g_\beta^{sat}}\right)^{a_{st}} |\dot{\gamma}_\beta| \quad (1.8)$$

where H_γ and g_γ^{sat} stand for the hardening modulus and the saturation critical resolved shear stress of the slip system γ, respectively, while g_β^{sat} and H_β are the corresponding values for the twin system β. $h'_{\alpha\gamma}$ stands for the latent hardening parameter between slip system α and slip system γ, while $h''_{\alpha\beta}$ is the latent hardening parameter between slip system α and twin system β. a_{ss} is the slip-slip hardening exponent, while a_{st} is the twin-slip hardening exponent.

The kinematic hardening contribution can be determined by the evolution of the backstress τ_α^b during the cyclic deformation, which is a simplification of the Ohno-Wang macroscopic model [151]. Moreover, it can reproduce the complex cyclic behavior of a polycrystal. Mathematically,

$$\dot{\tau}_\alpha^b = c_\alpha \dot{\gamma}_\alpha - d_\alpha \tau_\alpha^b \left(\frac{|\tau_\alpha^b|}{c_\alpha / d_\alpha}\right)^{k_\alpha} |\dot{\gamma}_\alpha| \quad (1.9)$$

where the parameter $1/d_\alpha$ indicates the absolute value of the shear caused by slip system α ($|\gamma_\alpha|$) when the back stress stabilizes, and k_α stands for the nonlinearity of the back stress evolution (kinematic hardening power), and the stabilized scalar back-stress for slip system α is c_α / d_α.

The evolution of the twin volume fraction in each twin variant, $\dot{f}_\beta$, follows a power law because twinning systems were treated as pseudo-slip systems. Tension twinning can only be activated when the resolved shear stress on the twin plane leads to an extension of the *c*-axis, and the twin volume fraction cannot increase if the whole volume linked with the Gauss point is completely twinned (i.e. $\sum f_\beta = 1$). Furthermore, if the resolved shear stress is the opposite of the one needed for twinning and reaches a critical value, the twinned region can detwin [47,88,152,153]. This means that $\dot{f}_\beta$ can be negative or positive, and the CRSS to activate twin boundary motion in both scenarios can be different. These criteria can be implemented mathematically as

$$\begin{cases} \dot{f}_\beta = \dot{f}_0 \left(\frac{|\tau_\beta|}{g_\beta}\right)^{\frac{1}{m}} sign(\tau_\beta) & if \;\; \dot{f}_\beta > 0 \quad and \quad \sum f_\beta < 1 \\ \dot{f}_\beta = 0 & if \;\; \tau_\beta \geq 0 \quad and \quad \sum f_\beta \approx 1 \\ \dot{f}_\beta = 0 & if \;\; \tau_\beta < 0 \quad and \quad f_\beta \approx 0 \end{cases} \tag{1.10}$$

where $\dot{f}_0$ is the references twin volume fraction rate, τ_β stands for the resolved shear stress on the twin system β (which can be calculated from equation (1.7) for the corresponding twin system), and g_β is the CRSS necessary to activate twining or detwinning. Although recent experimental observations showed that the CRSS of twinning and detwinning do not have to be equal [47,88], the same values of the CRSS for twinning and detwinning have been used in this investigation.

The hardening law for twin boundary motion is given by

$$\dot{g}_\alpha = \sum_{\beta=1}^{N_{tw}} h'''_{\alpha\beta} H_\beta \gamma_{tw} \left(1 - \frac{g_\beta}{g_\beta^{sat}}\right)^{a_{tt}} |\dot{f}_\beta| \tag{1.11}$$

where $h'''_{\alpha\beta}$ stands for the twin/twin latent hardening parameter, H_β the corresponding hardening modulus, g_β^{sat} the saturated CRSS for twinning or detwinning, and a_{tt} the twin-to-twin hardening exponent. It is assumed that plastic slip does not influence the hardening of twinning.

1.4.3. Numerical Simulation of Fatigue Behavior in Magnesium Alloys

Numerical simulations are a key tool to understand the mechanisms of fatigue behavior and provide quantitative predictions of the cyclic stress-strain curves and the fatigue life [154]. In the literature, crystal plasticity models based on finite element, fast Fourier transformation, and self-consistent techniques were often used to simulate the cyclic stress-strain curves and twin volume fraction evolutions of Mg alloys [91,146–149,155–158]. It should be highlighted that self-consistent models can accurately simulate the macroscopic behavior but cannot account for general boundary conditions, grain distributions, the addition of defects like voids, or the prediction of local fields [159].

The cyclic behavior and the activity of twinning during fatigue of Mg and its alloys were predicted successfully using the self-consistent models at low strain amplitudes

($\Delta\varepsilon/2$ ≈0.4%). However, there were still some deviations in cyclic curves and twin volume fractions at higher strain amplitudes [148,160,161]. In addition, the uniaxial ratcheting behavior of single crystal and polycrystal Mg alloy and the multiaxial ratcheting of extruded AZ31 Mg alloy under deformations dominated only by slip or twinning were simulated using a constitutive crystal plasticity model by Yu et al. [162] and Li et al. [163], respectively. They emphasized that the model was built using a small deformation plasticity framework because the final plastic strain was relatively small (not larger than 10%), thus, their model could not consider the evolution of texture and its influence on plastic deformation. More recently, the low-cycle fatigue behavior of a rolled AZ31 Mg alloy along the rolling direction was simulated successfully by Guo et al. [164] using a modified crystal-plasticity based on the finite strain elastic-viscoplastic self-consistent model containing a large deformation framework, slip, twinning, and detwinning. The numerical results showed that the evolution of lattice strain during the whole fatigue life (80 cycles) was in good agreement with the results of neutron diffraction. In addition, they demonstrated that the maximum twin volume fraction increased from the 1st to 2nd cycle, followed by a decrease until the 20th cycle and a secondary increase after the 20th cycle due to the activity of basal slip and twinning and the contribution of the residual twins [164].

Yaghoobi et al. [153] successfully modeled the fatigue behavior of the ZK60A Mg alloy along the extrusion direction by including a Taylor-type model in the PRISMS-Plasticity (an open-source crystal plasticity software) [165]. However, such crystal plasticity models do not account for the effect of stress within the twin on the slip, twinning, and detwinning. More recently, Yaghoobi et al. [159] used in-situ SEM-DIC (scanning electron microscope – digital image correlation) results to calibrate their advanced twinning/detwinning model for capturing the statistics of twin variants activation and twin area fraction in the fatigue of extruded Mg-4Al Mg alloy. In addition, they also predicted the first dominant twin variant for 47.5% of the grains and at least one of the two dominant twin variants for 80% of the grains at maximum compressive strain.

The CP model explained in section 1.4.2 was successfully applied to simulate the cyclic stress-strain curves of an Mg-RE alloy during computational homogenization at

different strain amplitudes (Fig. 1.7) [154]. According to Zhang et al. [154], basal and prismatic slip and continuous twinning-detwinning were the key mechanisms activated to accommodate cyclic deformation. Their material had an unusual texture which they approximated using a composite material made of Mg inclusions with the basal plane almost parallel to the extrusion axis (<5◦) embedded in a matrix of Mg crystals with random texture. In the matrix portions of the microstructure, basal slip always contributed more than prismatic slip, whereas prismatic slip was more significant in the inclusions when the material was deformed at high cyclic strain amplitudes. Full detwinning was placed in the inclusion areas of the fatigue cycle but not in the matrix sections, demonstrating the effect of texture on cyclic deformation processes.

1.4.4. Prediction of Fatigue Life in Polycrystals

The localization of damage is the main mechanism responsible of fatigue crack nucleation in polycrystals and it is associated with the extreme values of the statistical distribution of the microstructural features rather than on the average values. As a result, there is a significant experimental scatter among “nominally” similar polycrystals, which makes it challenging to draw a firm connection between microstructure and properties [91]. It is evident that only simulation approaches that consider the microstructural features (microstructure-sensitive computational modeling of fatigue) may establish a relationship between microstructure and fatigue properties [91,166,167].

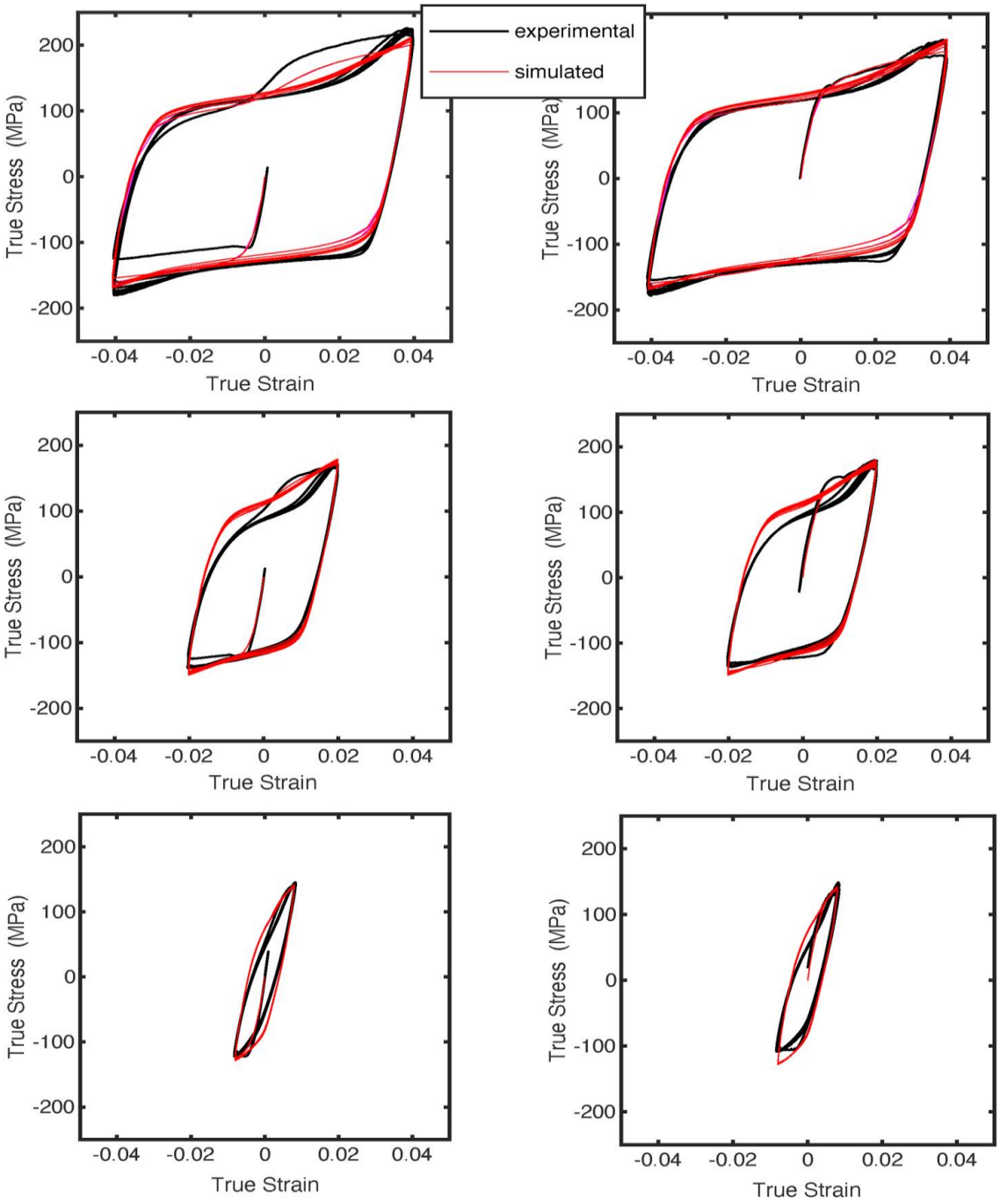

Figure 1.7 – Experimental (black) and simulated (red) cyclic stress-strain curves of the Mg-1Mn-0.5Nd (wt.%) alloy deformed along the extrusion direction. Different plots correspond to specimens deformed initially in either tension or compression at different cyclic strain semi-amplitudes ($\Delta\varepsilon/2$ = 0.8%, 2%, and 4%).

Fig. 1.8 shows the modeling framework for the fatigue behavior of polycrystalline metallic alloys based on the computational homogenization of polycrystals (CHP). The numerical simulation of the mechanical behavior of an RVE is the first step to acquire the

micromechanical fields in the whole RVE during cyclic deformation. The primary characteristics observed during the cyclic deformation of metallic alloys, including the Bauschinger effect, mean stress relaxation, ratcheting, and cyclic softening/hardening, should be considered in the constitutive model of single crystals, so the deformation mechanisms are adequately represented. This is often achieved through phenomenological models whose parameters should be calibrated for each alloy by comparing them to experimental cyclic stress-strain curves. Trial and error methods or optimization algorithms built on creating an objective error function can be used to complete this task [168]. The mechanical response of the polycrystal changes with the number of cycles until a stable stress-strain hysteresis loop is achieved. Depending on the alloy and the loading conditions, stabilization of the mechanical behavior may require a few cycles up to a few hundreds or thousands of cycles [168].

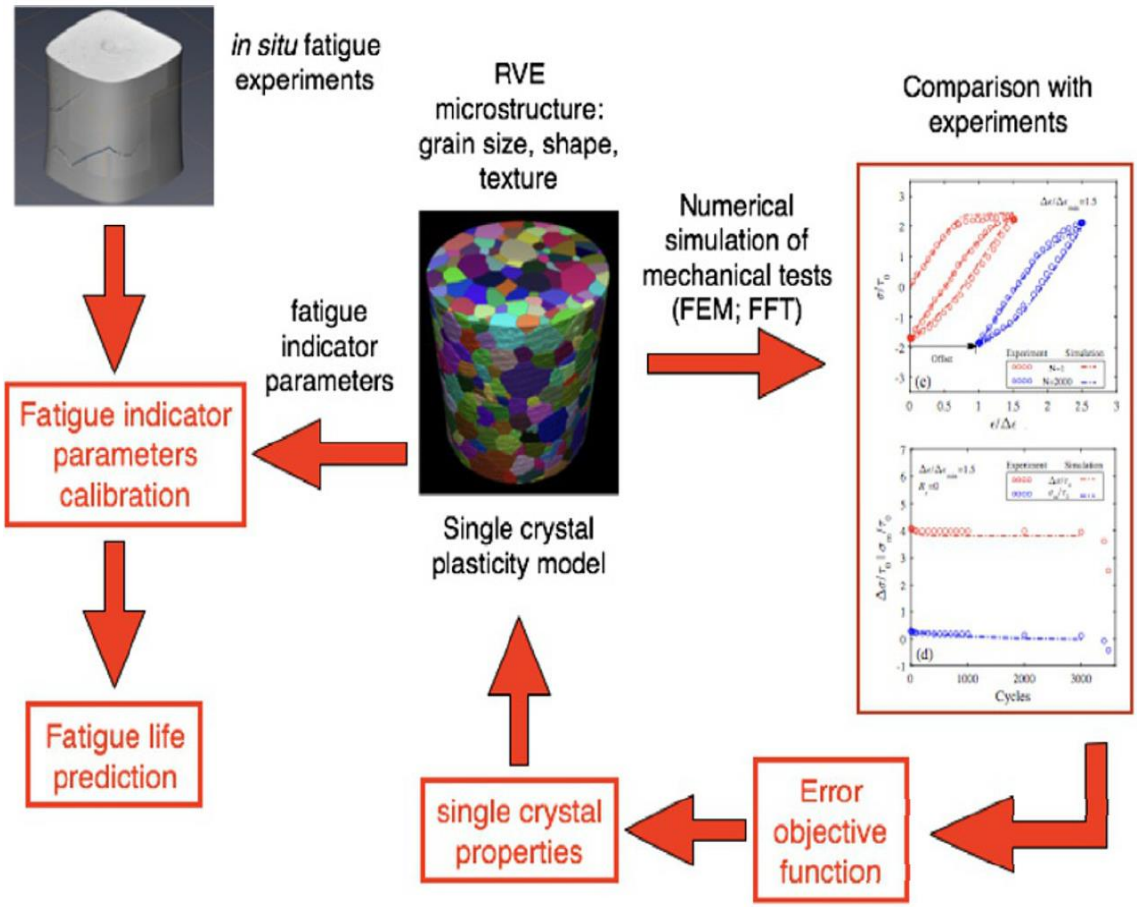

Figure 1.8 – Coupled experimental-simulation strategy to predict the fatigue life of polycrystalline metallic alloys using computational homogenization of polycrystals [91].

The prediction of the fatigue life is based on some fatigue indicator parameters (FIP), which are obtained from the evolution of mechanical fields and internal variables at the local level within the RVE when the stabilized cyclic stress-strain hysteresis loop has been determined through computational homogenization of the RVE. The main feature which controls crack nucleation can be described by the different FIPs according to the literature. Moreover, phenomenological relations can be used to link these FIPs to some stages of the fatigue life of the alloy under study (crack nucleation, minor crack propagation, or whole fatigue life) [91,169,178,170–177]. The most common FIPs reported in the literature are the accumulated plastic strain per cycle [169,170,173], the maximum shear strain [179–182], and the energy dissipated [174,183] or the energy density stored [173,175] in each cycle. It should be noted that the propagation of small micro-cracks dominates the majority of the fatigue life under low-cycle fatigue. However, most computational homogenization-based methods for predicting fatigue life assume that the fatigue life can be predicted using FIPs acquired from RVEs without cracks [91,184].

Zhang et al. [154] reported that the plastic shear strain accumulated in the slip system α of the voxel V during each fatigue cycle of an hcp Mg crystal can be calculated as follows [154]

$$\Delta\gamma^{\alpha}(V) = \int_{cyc} |\dot{\gamma}^{\alpha}(V)| dt \tag{1.12}$$

It should be noted that they did not include the contribution of twinning/detwinning to the plastic shear strain because it was assumed that this reversible process did not contribute to the accumulation of damage in Mg-RE alloys [94,154]. As an extension of Zhang's model, it was assumed that plastic strain associated with twinning/detwinning in each cycle can also lead to fatigue crack nucleation and their contribution to the FIP was also considered. The amount of $\Delta\gamma^{\alpha}(V)$ will be different throughout the RVE microstructure, and fatigue cracks will be initiated in the voxel with the highest cumulative plastic shear strain in stable fatigue cycles, which was considered as the FIP [154]. The fatigue life of an Mg-RE alloy has been predicted using the amount of cumulative plastic shear strain in different numbers of slip systems during one fatigue cycle according to equation (1.13) [154].

$$N = \Delta\gamma^{c} \,/\, \Delta\gamma_{s}^{\alpha} \tag{1.13}$$

where $\Delta\gamma^c$ is a material constant and N stands for the number of cycles to failure, which could be measured/compared with experimental data [154].

In addition, Briffod et al. [152] showed that the twin-induced FIPs had better trends in terms of mean behavior, relative dispersion, and stress amplitude sensitivity than the slip-induced (basal slip) FIPs to predict the high cycle fatigue life of AZ31 Mg alloy under load-controlled condition (Fig. 1.9) [152]. Therefore, it was claimed that twin initiation, despite the abundant basal slip even at low-stress amplitude, dominates the fatigue behavior under fully reversed load control. It should be noted that the use of FIPs to predict the fatigue life in Mg alloys is limited to the two studies mentioned above.

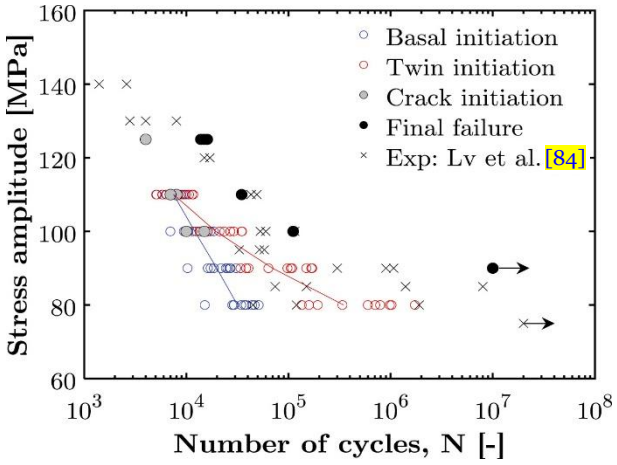

Figure 1.9 – Distribution of the extreme inverse FIP_{slip} and FIP_{twin} per aggregate fitted against experimentally observed crack initiation lives [152].

1.5. Motivations and Objectives

The fatigue behavior of Mg alloys has received much attention in recent years. However, conclusions could not be drawn on the effect of microstructural parameters (grain size, grain boundary orientation) on the fatigue behavior of Mg alloys. Furthermore, accurate analyses that provide reliable statistical information about the influence of different dominant deformation mechanisms (either basal slip, twinning/detwinning, or pyramidal slip) on fatigue crack nucleation mechanisms of Mg alloys are lacking. This information is essential to design Mg alloys with optimum fatigue resistance and also as input to predict the fatigue life of Mg alloys from fatigue indicator parameters [91,152,154].

In parallel, there are many investigations using crystal plasticity models to obtain the cyclic stress-strain curves in Mg alloys, as discussed in section 1.4.3. However, no study uses only one set of parameters to predict the cyclic stress-strain curves of Mg alloys at different strain amplitudes and orientations. In addition, the use of FIPs to predict the fatigue life in polycrystals was studied by different researchers, as was discussed in section 1.4.4. However, there are very few studies based on FIPs to predict the fatigue life of Mg alloys in the literature.

Therefore the objectives of this thesis are to study the link between deformation mechanisms and crack initiation under fully reversed strain-controlled fatigue of Mg alloys and to use this information to to predict the fatigue life of Mg alloys under fully reversed strain-controlled condition from computational homogenization simulations.

2. MATERIAL AND EXPERIMENTAL TECHNIQUES

2.1. Material

A rolled AZ31B-O magnesium alloy slab of dimensions 80×65×500 mm perpendicular to the rolling direction was purchased from Magnesium Elektron Company. The nominal chemical analysis provided by the supplier is shown in table 2.1.

Table 2.1 – Nominal Chemical Analysis of AZ31B-O

Chemical Analysis	
Alloying Element	Content (%)
Aluminum	2.89%
Zinc	1.05%
Manganese	0.42%
Magnesium	Balance

2.2. Sample preparation

2.2.1. Cutting

Three sheets with dimensions of 15×15×3 mm were cut with a handsaw to study the texture and microstructure of the as-received material. The samples were obtained from rolling-transverse, rolling-normal, and 45° between rolling and normal planes of the rolled material (one for each plane).

Flat dogbone samples for fatigue tests were obtained using Electrical Discharge Machining (EDM) in the rolling direction (RD), transverse direction (TD), normal direction (ND), and 45° between rolling and normal directions (45°) from the as-received materials. The dimensions of the specimens are shown in figure 2.1. EDM is a well-known method that offers remarkable advantages when machining magnesium alloys, such as the possibility of reproducing complex geometries, suppression of the heating in the samples, and excellent surface finish.

Specimens with rectangular cross-sections were selected in this investigation (instead of cylindrical ones that are standard to measure the fatigue life) to accurately assess the deformation and fracture mechanisms on the flat lateral surfaces during interrupted fatigue tests.

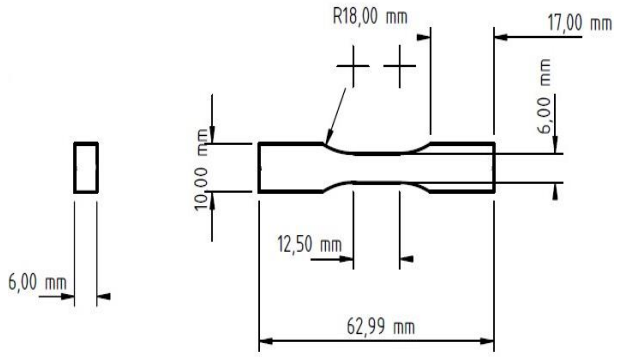

Figure 2.1 – Schematic of fatigue samples.

2.2.2. Surface Preparation

All the texture samples were prepared by mechanical grinding. Each surface was manually ground on consecutive abrasive SiC papers with a grit size of 1200, 2000, and 4000, followed by three polishing steps with 3 μm, 1 μm, and 0.25 μm diamond paste. Afterwards, they were etched using Nital 5% (5% nitric acid and 95% ethanol) solution at room temperature to eliminate the residual stresses after grinding.

Three specimens per condition were prepared for fatigue life tests. The surfaces and edges were manually ground on consecutive abrasive SiC papers with grit sizes of up to 4000, leading to mirror-like surfaces. The main concern of the process was ensuring an identical surface quality in all the materials to eliminate the influence of surface roughness on the fatigue response.

Interrupted fatigue test samples were etched with the specific solution (chemical composition shown in table 2.2) for 10 seconds to reveal the grain boundaries. They were again etched with Nital 15% (15% nitric acid and 85% ethanol) for 2 seconds to get a mirror-like surface. After etching, they were cleaned by immersion in an ultrasounds bath of pure ethanol for 3 minutes. Thus, the microstructural details, as well as the interaction

between deformation mechanisms (slip bands, twins) with the microstructural features, could be accurately ascertained by scanning electron microscopy (SEM), and simultaneously grain orientation and twins could be revealed by electron back-scattered diffraction (EBSD). The surface of the specimens was etched because thousands of grain boundaries should be analyzed in the SEM to determine the exact crack initiation sites. It should be noted that the depth of the grain boundaries after etching was measured by atomic force microscope, and the average grain boundary depth was very small (< 250 nm). This etching step can significantly affect the stress concentration at grain boundaries in the high-cycle fatigue test. However, it can not cause the stress concentration at grain boundaries in low cycle fatigue (LCF) of Mg alloys [89,90,94], and the fatigue crack initiation sites depend on the deformation mechanisms.

Table 2.2 – Chemical composition of the etchant solution

Picric Acid	Acetic Acid	Distilled Water	Ethanol
0.4 g	2.5 ml	2 ml	4 ml

2.3. Microstructural Characterization

2.3.1. Texture Analysis by X-Ray Diffraction (XRD)

The macro texture evolution of the as-received samples was analyzed by X-ray diffraction to get more precise grain orientations. The measurements were performed using Cu Kα radiation at 50 kV with the sample tilt angle ranging from 0° to 90° for {0002} basal slip, $\{10\bar{1}0\}$ prismatic slip, and $\{10\bar{1}1\}$ first-order pyramidal slip systems. All these measurements are carried out for RD-TD, RD-ND, and 45° between RD and ND (45° RD-ND) planes.

2.3.2. Electron Backscatter Diffraction (EBSD)

Electron backscatter diffraction (EBSD) is a scanning electron microscope (SEM) based diffraction technique widely employed in material characterization due to its exceptional spatial resolution, high speed, and ability to recreate three-dimensional microstructures [185,186]. EBSD enables to obtain quantitative information about the

grain size, grain boundary character, crystallographic orientation, and phase identification from the surface of bulk polycrystals.

The microstructural features were acquired from the area at the center of the samples with a FEI Helios Nanolab 600i dual-beam microscope equipped with a Nordlys EBSD detector from Oxford Instruments. Statistically representative maps containing at least 1500 grains were collected for each condition with an acceleration voltage of 20 kV and acceleration current of 2.7 nA. The step size was one-twelfth of the average grain size to guarantee an acceptable mapping resolution.

Average grain size, grain size distribution, grain boundary misorientation angle, and crystal orientation were extracted from the raw data using the Matlab toolbox MTEX [187]. Following the common practice, the minimum misorientation angle to define a high-angle grain boundary was set to 10° for grain detection. MTEX allows reconstructing the grains in the EBSD map through a Voronoi decomposition of the domain [187]. The grains were reconstructed from the crystallographic orientation recorded for the indexed pixels with a grain boundary threshold angle of 2°. Then, the grains whose grain size was smaller than 25 pixels were removed, and the grain computation was repeated. Afterwards, the EBSD dataset was restricted to the indexed phase (Mg), and the inaccurate measurements were removed using a spline filter. Then, the orientation of missing data was interpolated using the nearest neighbor method, and grain boundaries were smoothed.

2.4. Mechanical Characterization

2.4.1. Fatigue Life Tests

The fatigue life tests are intended to obtain the fatigue life curves and assess the evolution of the stress-strain curves. The deformation in the central section of the cylindrical specimens was measured and controlled with an extensometer. Fully reversed ($R = -1$), constant strain amplitude low cycle fatigue tests ($N < 10^5$ cycles) were performed using the servo-hydraulic Instron 8802 testing machine. Fatigue life tests were carried out at three different cyclic strain semi-amplitudes of $\Delta\varepsilon/2 = 0.4\%$, 0.8 %, and 2.0% at a constant frequency of 0.5 Hz in RD, ND, TD, and 45° between RD and ND. The specimens

were initially deformed in compression in all cases. The load and the deformation were recorded during the tests, which finished when the sample failed.

2.4.2. Interrupted Fatigue Tests

Two different cyclic strain semi-amplitudes of $\Delta\varepsilon/2$ = 2.0% and 0.4% in RD and 45° RD-ND were selected for interrupted tests to have all the dominant deformation mechanisms (basal slip, twinning/detwinning, pyramidal slip) in fatigue of magnesium alloys. These tests were stopped before failure at the number of cycles indicated in Table 2.3. They correspond to approximately 1/5 of the fatigue life in the specimens oriented at 45° RD-ND and 1/3 of the fatigue life in those deformed along the RD. The fatigue tests were always stopped after the maximum compressive strain was attained.

Table 2.3 – Number of Fatigue Cycles in the Interrupted Tests.

Orientation	$\Delta\varepsilon/_2 = 0.4\%$	$\Delta\varepsilon/_2 = 2.0\%$
45° RD-ND	1200 cycles	50 cycles
RD	500 cycles	50 cycles

2.5. Analysis of Deformation and Crack Initiation Mechanisms

Three circular marks were milled on the center of the samples subjected to interrupted fatigue tests using a focus ion beam in a dual-beam microscope (Helios Nanolab 600i) to track the identical area before and after deformation. The circle diameter and depth were 30 μm and 1 μm, respectively. An area far from circles (but still in the center of the sample) was chosen to avoid the possible stress concentrations at circles to investigate the fatigue deformation and crack initiation mechanisms. Then, the surface of the interrupted fatigue samples was observed with an Apreo 2S LoVac field emission scanning electron microscope (FE-SEM) (ThermoScientific, Netherlands) equipped with an Oxford-HKL EBSD detector at 20 kV and 2.7 nA before and after deformation to identify slip traces and fatigue crack nucleation sites at sub-micron scales.

Slip Trace Analysis

The use of EBSD in trace analysis has provided substantial and reliable evidence of the active deformation mechanisms. This approach has emerged as a crucial tool in resolving several outstanding controversies regarding the plasticity of Mg alloys [188]. The methodology used in this study to determine the active slip system or twin is explained in [188–190] and it has been summarized below.

The experimental approach utilized by Cepeda et al. [188] is illustrated in Fig. 2.2. To avoid the impact of surface oxidation, which could hinder the observation of trace appearance during straining, mechanical tests are performed using a microtensile testing machine (Fig. 2.2a) within an SEM.

The determination of slip activity is determined as follows. A slip trace is defined as a straight line that emerges from the intersection of an active slip plane with the sample surface, as highlighted in red in Fig. 2.2b. These traces become visible due to the formation of a surface step parallel to the specific plane after a specific strain. A twin trace is the long axis of a twin lamella that is visible on the surface. Firstly, EBSD is used to map large areas of the microstructure at the center of the gage section of the tensile/compression specimens before each test, as illustrated in the pre-test EBSD map in Fig. 2.2c. Secondly, the microstructure's evolution within these regions is monitored after deformation using Secondary Electron (SE) imaging with the SEM. The aim is to detect and track the development of as many slip traces as possible in a large number of grains. Post-process of the EBSD maps of the same areas is performed after tensile/compression testing up to a specific strain, to measure the orientations of the grains that exhibited slip traces. Then, a specific trace (such as the one shown in Fig. 2.2b) is selected, and its orientation is compared with the 12 potential traces given by a dedicated MATLAB code [191] from the orientation (three Euler angles) of the corresponding grain obtained from EBSD map (each trace corresponding to a different slip plane, as shown in Fig. 2.2e). In this code, the cross product between the slip plane normal and the Z axis of the specimen (perpendicular to the surface) in the sample reference frame was used to determine the theoretical orientation of the slip traces for each potential slip plane in Mg (basal, prismatic, or pyramidal). Finally, the selected trace

is assigned to the slip plane that provides the best match, with the MATLAB code also providing information about the Schmid Factor of the corresponding system (Fig. 2.2f). A similar methodology is employed to estimate twin activity. Twin lamellae are readily identifiable in EBSD maps after deformation because of the associated lattice rotations (with rotation angles dependent on the particular twin system).

The process of trace/twin identification is repeated for as many traces/twins as possible to obtain data that are statistically significant to estimate the activity of different deformation mechanisms. The frequency of observed traces is then linked to the activity of different slip and twin systems.

According to Schmid's law, a slip system can become active only if the resolved shear stress applied to the material exceeds the critical resolved shear stress of that particular slip system [192]. The slip or twinning system with the highest Schmid factor (SF) is the most likely to be activated [193–195]. Therefore, SF is commonly utilized to assess the activation of deformation modes, particularly for Mg alloys subjected to a uniaxial stress state.

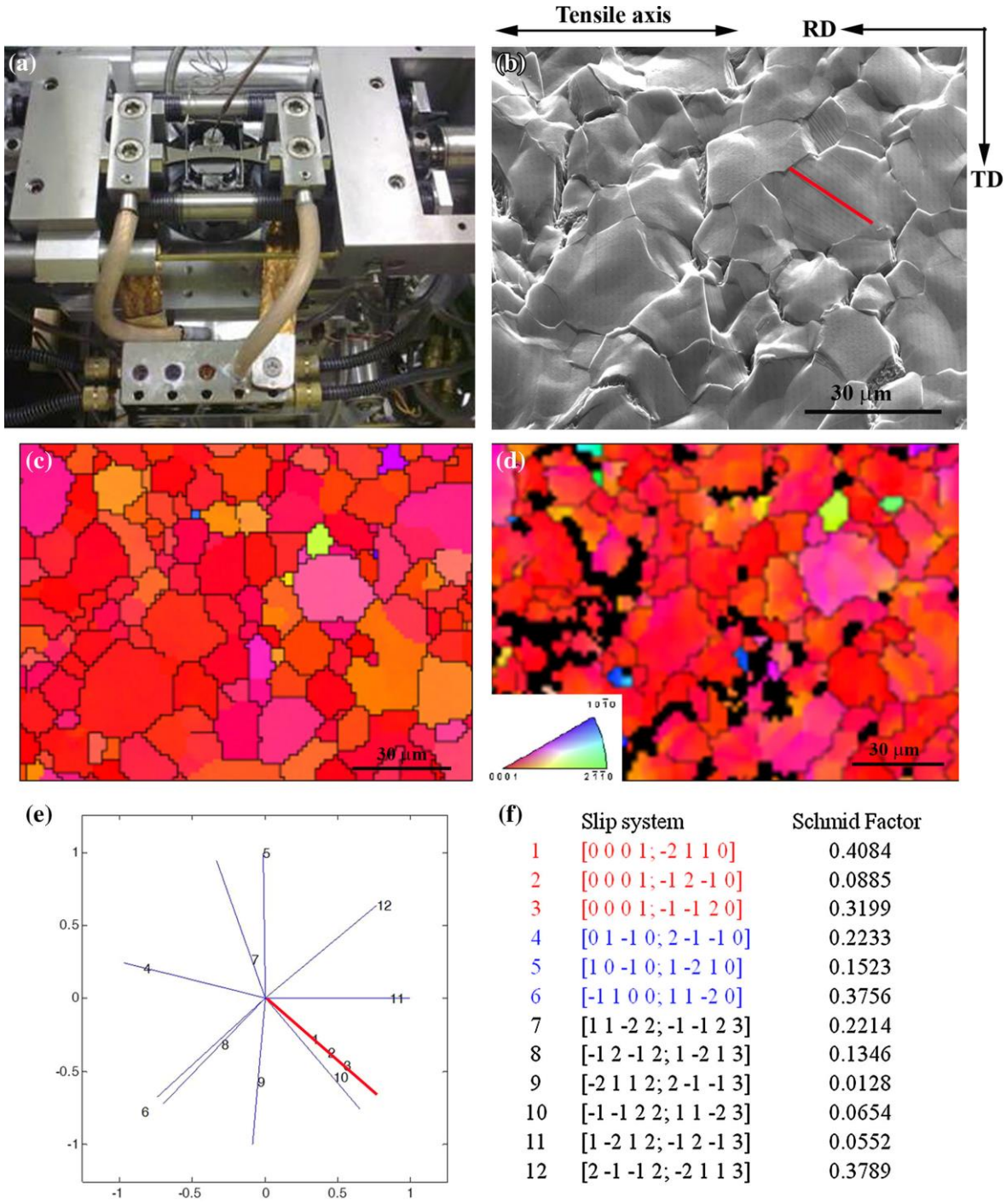

Figure 2.2 – Methodology used for slip trace analysis. a) Screw-driven tensile micromachine placed inside a scanning electron microscope (SEM). b) SEM micrograph showing the appearance of slip traces (red lines). c) and d) EBSD IPF maps in the ND corresponding to the SEM micrograph before and after straining, respectively. e) Calculation of the 12 possible traces and determination of the active slip system and f) Schmid factors for each grain in which a trace was detected [188].

3. FATIGUE DEFORMATION MECHANISMS

3.1. Initial Microstructure

The EBSD maps showing the grain orientations of the AZ31 Mg alloy in TD-45° RD-ND and RD-TD planes are shown in Figs. 3.1a and 3.1c, respectively. Moreover, the inverse pole figures of the (0002) orientations obtained by X-ray diffraction in the same planes are presented in Figs. 3.b and 3.1d, respectively. Most grains are suitable for accommodating plastic deformation via basal slip and twinning when the material deformed along the 45° RD-ND in TD-45° RD-ND plane because their c axis formed an angle of ≈45° with this plane (Fig. 3.1b). In contrast, the material has a strong basal texture in the RD-TD plane with the c axis of most grains perpendicular to the RD-TD plane (Fig. 3.1d). Hence, the basal slip will be hindered by the low Schmid factor of all basal slip systems due to the orientation of the basal planes, and tensile twinning can only take place in compression in most of the grains during deformation along the RD. The initial EBSD map for the specimen deformed along RD at $^{\Delta\varepsilon}/_{2} = 0.4\%$ is depicted in Fig. 3.1c. There is a region marked with a black rectangle in the RD-TD plane (Fig. 3.1c) where the grains are suitably oriented to accommodate plastic deformation by basal slip. This region was observed in the specimen deformed along RD at $^{\Delta\varepsilon}/_{2} = 0.4\%$. However, it was not seen in the studied area of the specimen deformed along RD at $^{\Delta\varepsilon}/_{2} = 2\%$ (Fig. 3.1e). In addition, some small grains (with a grain size below 20 μm) were fully twinned grains because of their orientation and grain boundary misorientation angle ≈ 86° (which corresponds to the twin boundary misorientation in Mg magnesium alloys), and 3 of them were marked with black arrows in (Fig. 3.1e). The grain boundaries and twin boundaries in Fig. 3.1e are shown with black and red lines, respectively, in Fig. 3.1f to demonstrate the grain boundary misorientation angle (≈ 86°) of the fully twinned grains.

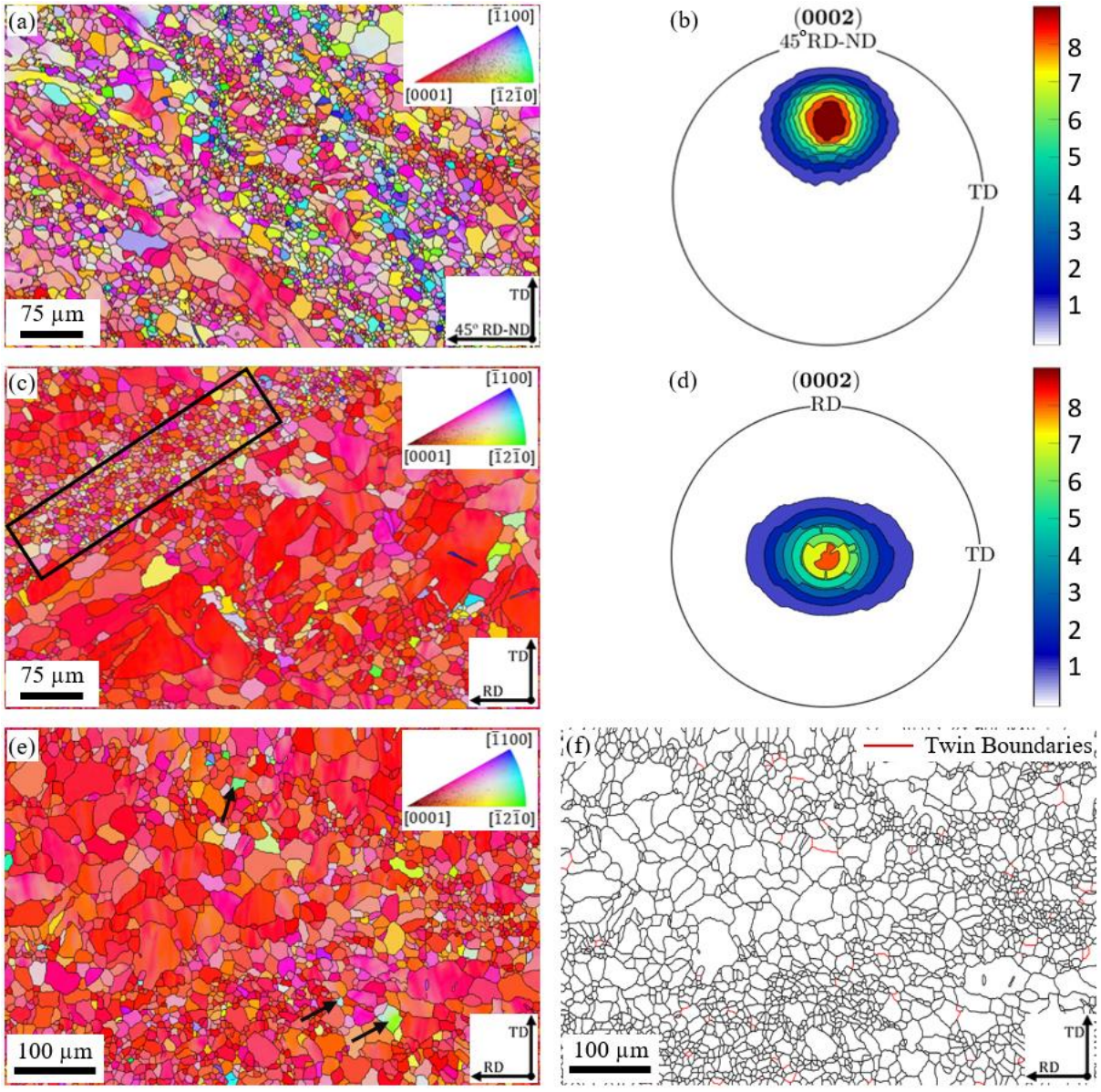

Figure 3.1 – EBSD map showing the grain orientation according to the inverse pole figures in (a) TD-45° RD-ND plane (c) RD-TD plane. XRD pole figures in (b) 45° RD-ND plane (d) RD-TD plane. (e) Initial EBSD image showing the orientation of the grains in the studied region in RD at $^{\Delta\varepsilon}/_{2}$ = 2%. Twinned grains (as indicated by the orientation and the grain boundary misorientation angle) are marked with arrows) (f) Grain boundaries and twin boundaries of the studied area in (e).

The cumulative grain size distributions (obtained from two EBSD maps for each plane) are plotted in Fig. 3.2a for both planes. The average grain sizes are 7.2 ± 4.4 µm (TD-45° RD-ND) and 9.1 ± 5.2 µm (RD-TD), and this difference can be attributed to the rolling process. More than 80% of the grains in both orientations were < 10 µm, although

large grains up to 50–60 μm were also present in both planes. The fraction of large grains was higher in the RD-TD plane. The grain boundary misorientation distributions obtained from the EBSD maps (two EBSD maps for each plane) in both planes are plotted in Fig. 3.2b, and they are practically superposed with a maximum of around 30°. There is a tiny peak in both cases at around 86°, which indicates that there were very few twins in the as-received alloy.

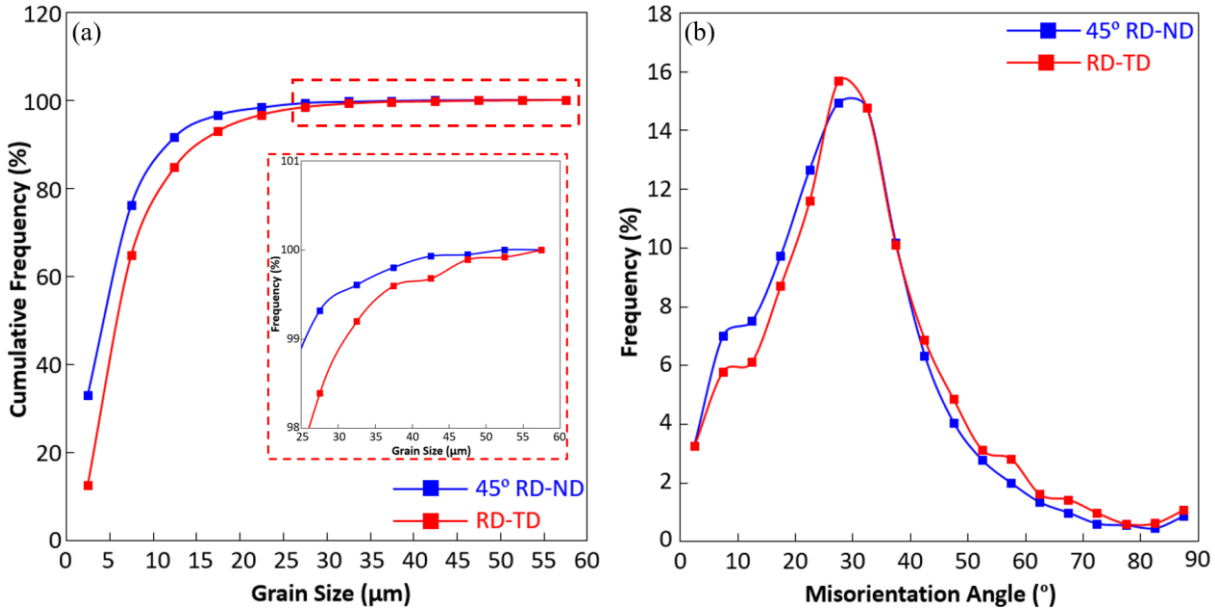

Figure 3.2 – (a) Cumulative grain size distributions in different planes. (b) Initial misorientation angle distributions in different planes.

3.2. Cyclic Stress-Strain Curves and Fatigue Life

The experiments to measure the fatigue life were carried out under strain control at cyclic strain semi-amplitudes ($\Delta\varepsilon/2$) of 0.4%, 0.8%, and 2% with a strain ratio of R=-1, as indicated in section 2.4.1. At least two tests per condition were performed to check the scatter. The cyclic stress-strain curves for different values of the applied cyclic strain semi-amplitude are plotted in Figs. 3.2-5 for the different orientations along RD, TD, ND, and 45° between RD and ND, respectively. In general, the cyclic stress-strain curves reached a steady-state condition after a few cycles and presented similar features to those reported by others [76,79,82,83] in Mg and Mg alloys.

The hysteresis loops of the specimen deformed along the RD are not symmetric (Fig. 3.3). Plastic deformation during the compression part of the first cycle occurs at constant stress (Fig. 3.3), and this behavior is in agreement with massive twining, which is supported by the strong basal texture (Fig. 3.1d). Detwinning is expected to be active during unloading, particularly when the far-field stresses become tensile until it is fully completed. Tensile twinning cannot accommodate further plastic deformation in tension, and most grains are not suitably oriented for basal slip. Thus, the pyramidal slip has to be activated, leading to a strong strain hardening (Fig. 3.3) [80,85,154,196,197]. The shape of the stress-strain curve in the second load cycle in tension was not the same as in the first cycle. The strain range of the twinning part at second cycle is much larger than the first cycle, therefore, there are many more twins. As a result, the detwinning part in second cycle accommodated larger strains. Afterwards, the shape of the cyclic stress-strain curves did not change significantly with the number of cycles until failure. The plastic deformation mechanisms were similar during the whole fatigue life and are reflected in the corresponding shapes of the hysteresis loops at the 100th cycle in the RD.

The shape of the stress-strain curves in the TD is similar to the ones in the RD (Fig. 3.4) due to the similar sequence of active deformation mechanisms. These stress-strain curves for RD and TD were also reported in other investigations [80,84].

The shapes of the stress-strain curves along the ND also show similar differences between the tension and compression regions (Fig. 3.5), although the sequence of events was different. The curves showed parabolic hardening during compression in the first cycle, followed by twinning when the load was reversed to tension. The shape of the stress-strain curve in the second load cycle in compression was not parabolic (presented an S-shape) due to the development of detwinning (like in the tensile region of the second cycle along RD and TD). This asymmetric behavior in cyclic stress-strain curves of the AZ31 magnesium alloy agrees well with the previous investigations in the hot-rolled condition [65,80].

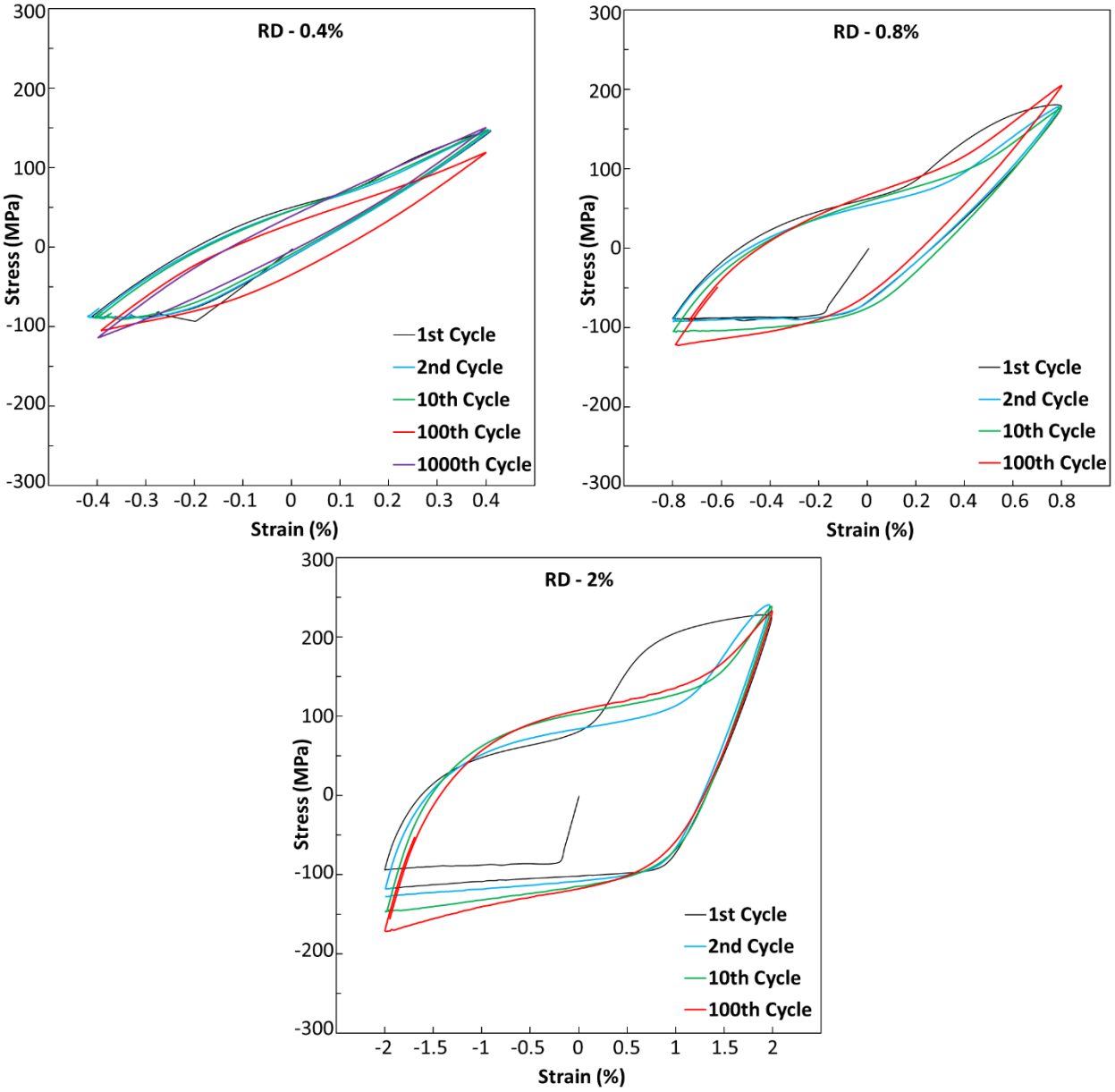

Figure 3.3 – Cyclic stress-strain curves of the RD specimens loaded in cyclic deformation at different strain amplitudes.

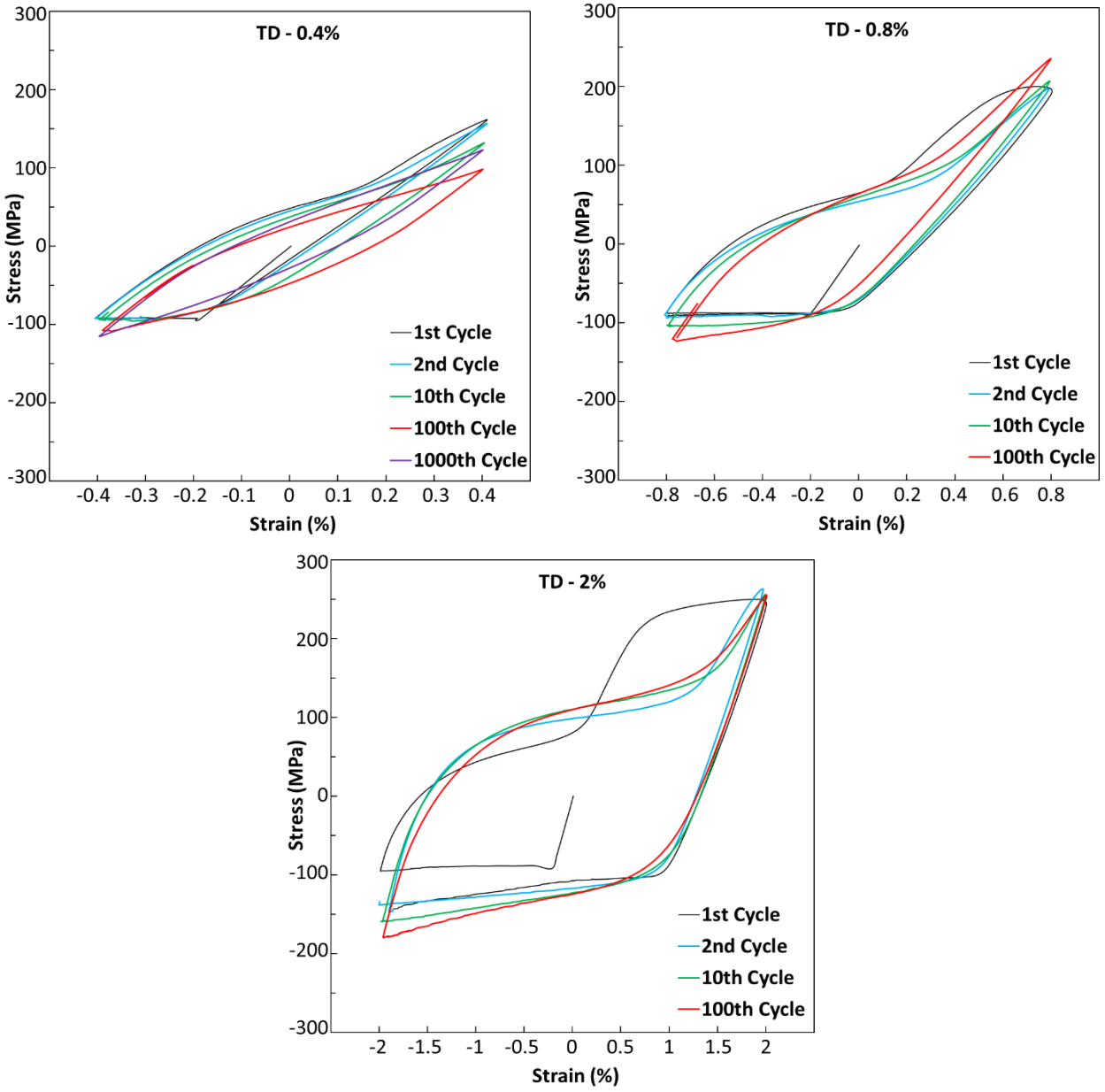

Figure 3.4 – Cyclic stress-strain curves of the TD specimens loaded in cyclic deformation at different strain amplitudes.

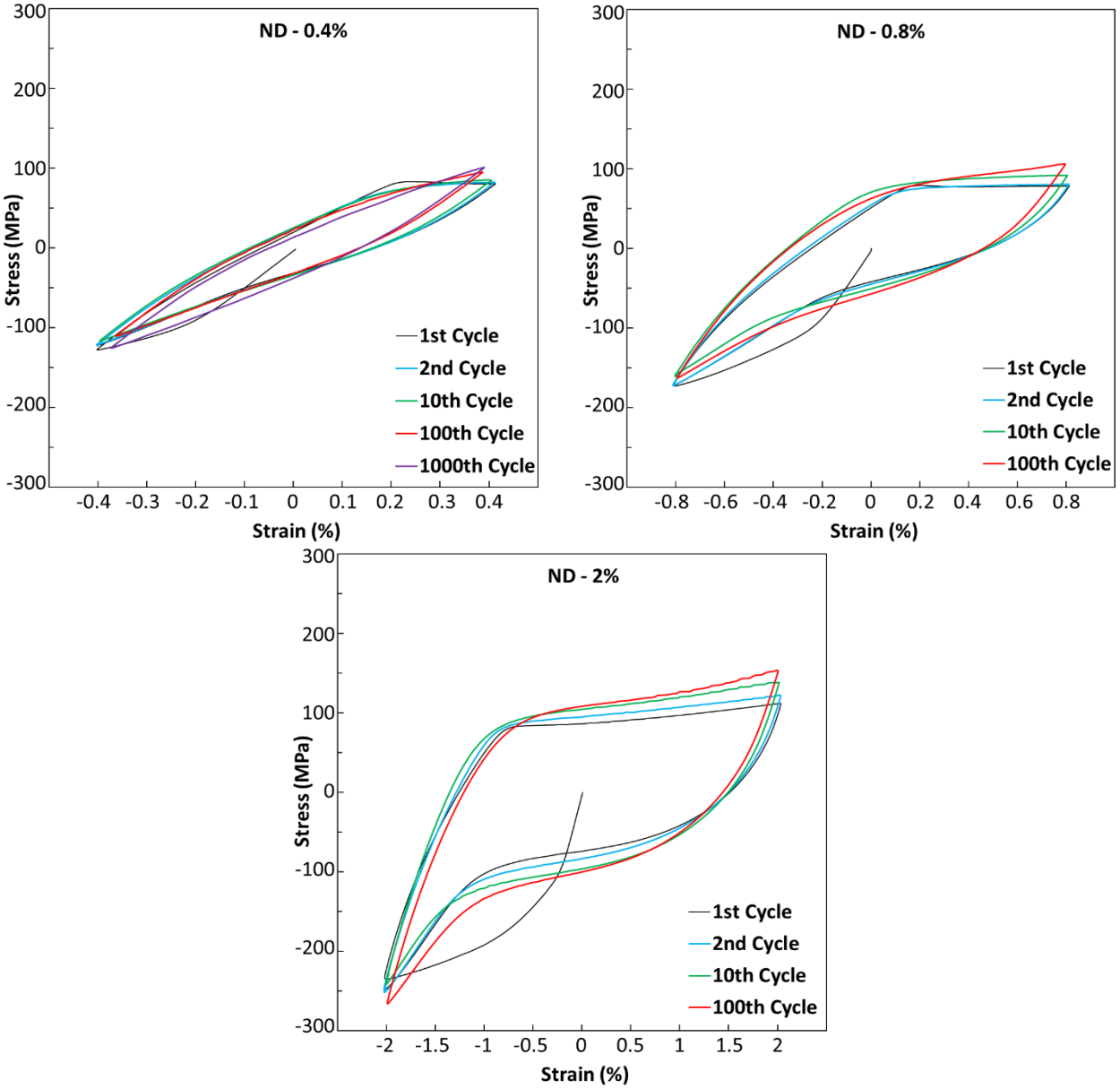

Figure 3.5 – Cyclic stress-strain curves of the ND specimens loaded in cyclic deformation at different strain amplitudes.

The cyclic stress-strain curves of the specimens deformed along 45° RD-ND at different number of cycles are plotted in Fig. 3.6. The hysteresis loops are symmetric from the first fatigue cycle in the specimens deformed along 45° RD-ND, and this behavior indicates that similar deformation mechanisms are active in the tensile and compressive parts of the fatigue cycle. Taking into account the orientation of most of the grains (Fig. 3.1b), basal slip is expected to be the dominant deformation mechanism together with

tensile twinning [65,92,93,198]. In addition, grains twinned during the compressive part of the cycle will detwin in the tensile part and viceversa.

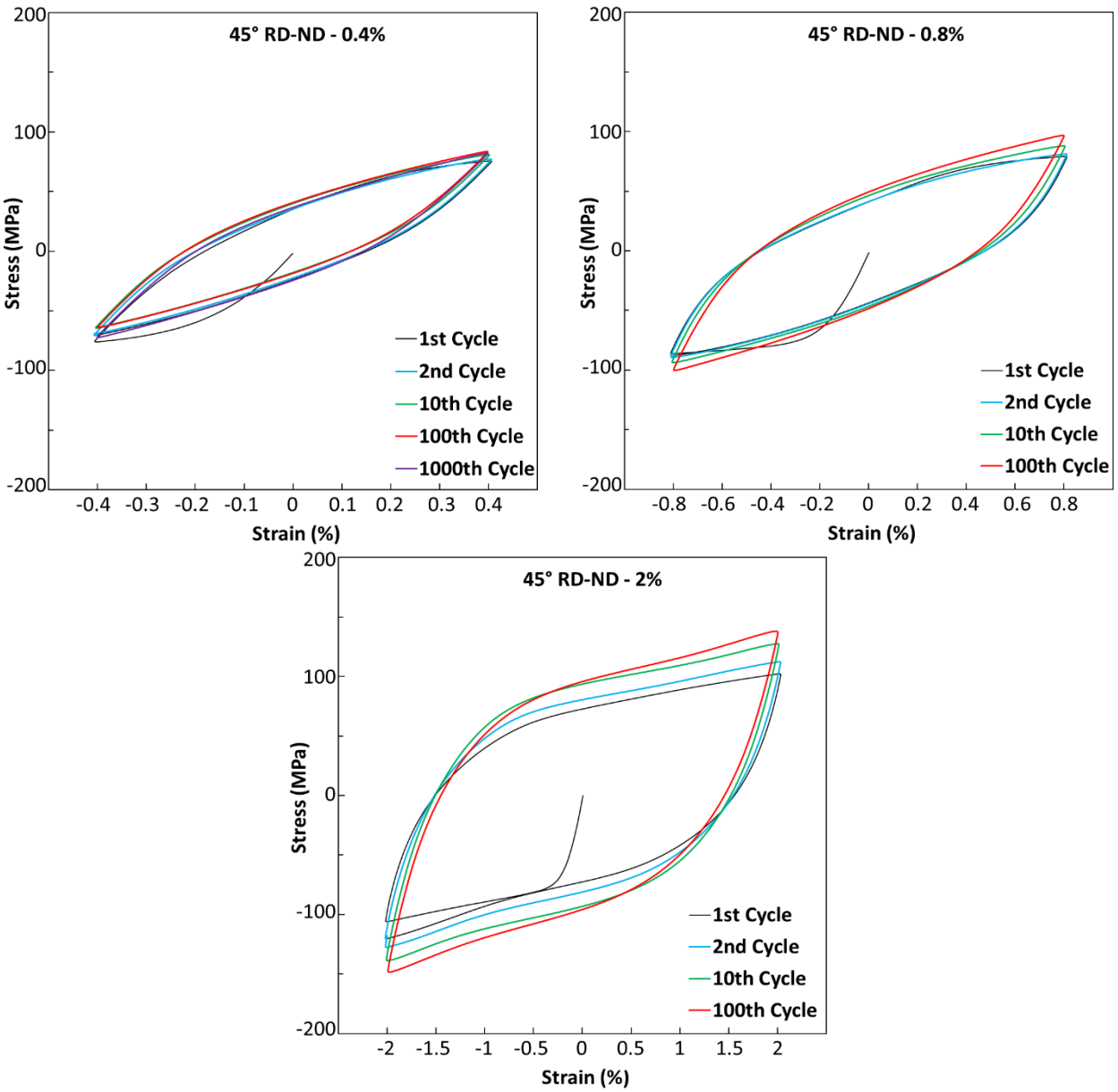

Figure 3.6 – Cyclic stress-strain curves of the 45° specimens loaded in cyclic deformation at different strain amplitudes.

The stress-strain curve of the first cycle in RD, TD, ND, and 45° RD-ND at $\Delta\varepsilon/2$ = 2% is shown in Fig. 3.7 to clarify the effect of the deformation mechanism on the cyclic stress-strain curves in the rolled AZ31 Mg alloy. It is evident that the yield stress during deformation along 45° RD-ND (compression part) is much lower (≈70 MPa) than in other orientations because deformation will mainly be accommodated by basal slip (which has

the minimum CRSS among different deformation mechanisms in Mg alloys) instead of either twinning or pyramidal slip. Deformation along the ND (compression) leads to the highest yield stress (≈140 MPa) due to the activation of pyramidal slip (which has the maximum CRSS among different deformation mechanisms in Mg alloys). Finally, the activation of twinning ($CRSS_{Ba}<CRSS_{Tw}<CRSS_{Py}$ in Mg alloys) in the compressive part of the cycles in RD and TD resulted in a yield stress of 100 MPa.

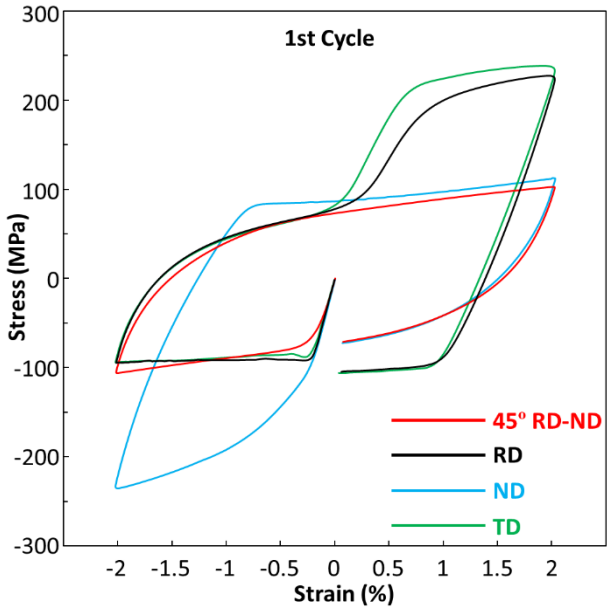

Figure 3.7 – Cyclic stress-strain curves of the first cycle for different orientations at $\Delta\varepsilon/2 = 2\%$.

The stress-strain curves of the first cycle at the $\Delta\varepsilon/2$ = 0.4%, 0.8%, and 2% in RD are plotted in Fig. 3.8 to illustrate the strain semi-amplitude dependency of the hysteresis loops. As shown in Fig. 3.8, the hysteresis loops are narrow and almost symmetric at a low strain amplitude of 0.4%. In addition, the maximum stress in tension in each fatigue cycle is higher than the maximum stress in compression, and the asymmetry increases with $\Delta\varepsilon/2$ because of the strain hardening associated with pyramidal slip [30,36,65,67,68,83,89,90].

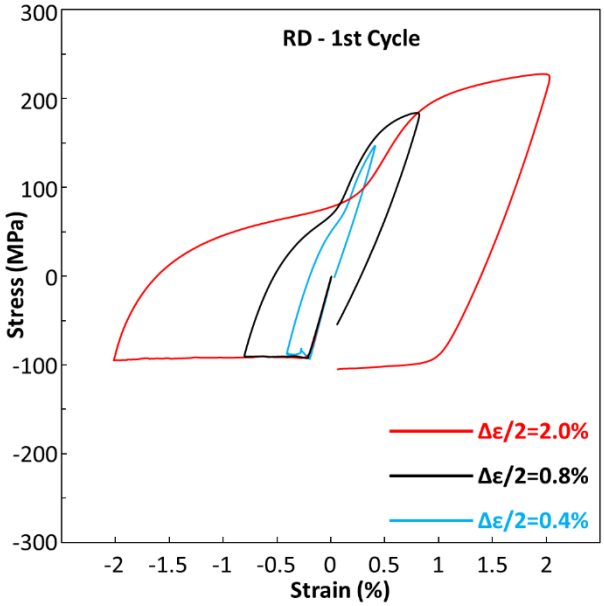

Figure 3.8 – Cyclic stress-strain curves of the first cycle for different strain semi-amplitudes in RD.

The evolution of the maximum (σ_{max}) and minimum (σ_{min}) stress in each cycle with the number of fatigue cycles N is plotted in Fig. 3.9 for the specimens deformed along RD, TD, ND, and 45° RD-ND. There are large differences between the absolute values of σ_{max} and σ_{min} in the RD, TD, and ND for any given cyclic strain semi-amplitude due to the activation of different deformation mechanisms in the tension and in compression, and the differences increase with $\Delta\varepsilon/2$. In contrast, the magnitude of the maximum and minimum stress is the same when the samples are loaded along 45° RD-ND ($\sigma_{max} \approx |\sigma_{min}|$).

A glance at the results for σ_{max} and σ_{min} suggests that both σ_{max} and σ_{min} remained almost constant throughout the test at $^{\Delta\varepsilon}/_{2} = 0.4\%$, while a slight cyclic hardening occurs in both tension and compression with the number of cycles at $^{\Delta\varepsilon}/_{2} = 0.8\%$ and $^{\Delta\varepsilon}/_{2} = 2\%$ for any material orientation. Thus, higher strain amplitudes result in larger cyclic hardening. The maximum cyclic hardening was observed in the compressive stress of the specimens deformed along the RD and TD (Fig. 3.9a and 3.9b). It could be attributed to the latent hardening associated with the interaction of the twin boundaries with the pyramidal dislocations accumulated during the tensile part of the cycle because

the twins act as obstacles to dislocation motion. Moreover, the hardening ratio increased with $^{\Delta\varepsilon}/_{2}$ because the contribution of twinning also increased. These results are in good agreement with the previous studies on te evolution of the maximum (σ_{max}) and minimum (σ_{min}) stress as a function of the number of fatigue cycles [65,80].

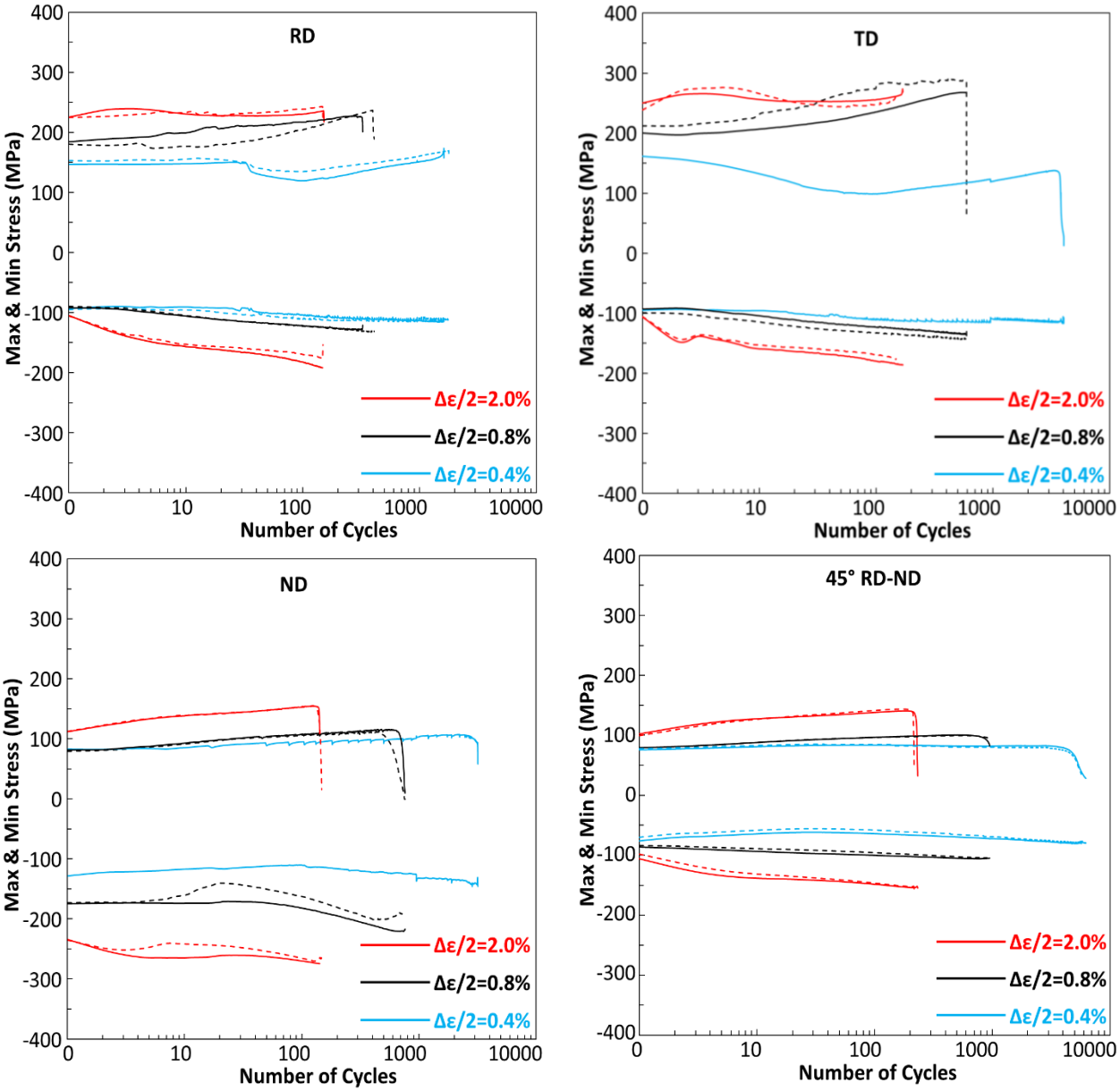

Figure 3.9 – Evolution of the maximum (σ_{max}) and minimum (σ_{min}) stress as a function of the number of cycles N in different orientations.

The fatigue life is plotted in Fig. 3.10 as a function of applied cyclic strain semi-amplitude ($\Delta\varepsilon/_2$) for the rolled AZ31 Mg alloy deformed along RD, TD, ND, and 45° RD-ND. The fatigue life at 45° RD-ND is much longer than that along other orientations. The origin of the differences between fatigue lives at different orientations can be traced to the activation of the different deformation mechanisms at different orientations. It should be noted that the lines in Fig. 3.10 are drawn by connecting the average fatigue lives at different strain amplitudes in each orientation.

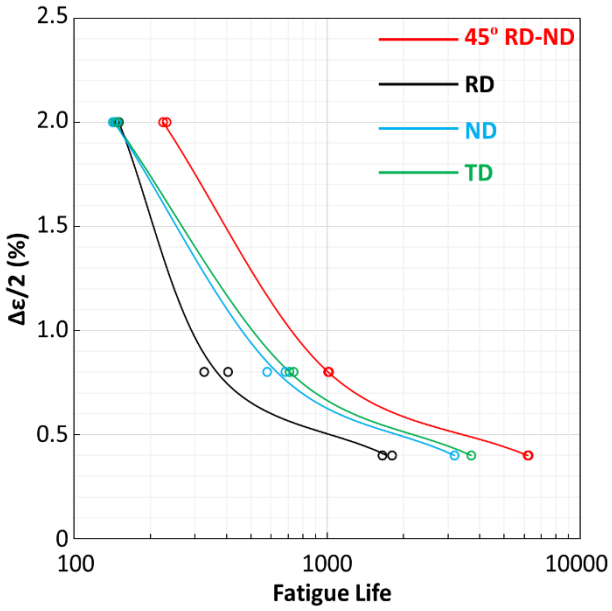

Figure 3.10 – Fatigue life as a function of the cyclic strain semi-amplitude, $\Delta\varepsilon/_2$ of the all specimens. RD, ND, TD, and 45° RD-ND stand for the samples deformed along rolling, normal, transverse, and 45° between rolling and normal directions, respectively.

3.3. Cyclic Deformation Mechanisms in RD

The surface of the specimens after 1/3 of the fatigue life was analyzed using SEM to discover the dominant deformation mechanisms as a function of the strain amplitude in the RD (Table 3.1). The theoretical orientation of the slip systems (basal and pyramidal slip) and of six different tensile twin variants were determined grain by grain in all samples using slip trace analysis methodology by grain orientation (which was extracted from EBSD maps) presented in [188–190]. These theoretical traces were compared with the orientation of the slip bands and of the elongated twins observed in the deformed

specimens in the SEM using secondary electrons. Most active slip systems had a distinct slip plane trace and appropriate deviation angles for other slip planes. Although, the slip trace analysis cannot discriminate between slip systems if they share the same slip plane. In these cases, the slip system showing the largest Schmid factor was considered the active slip system [192,199].

The EBSD map of the sample deformed during 50 fatigue cycles along the RD at $\Delta\varepsilon/2 = 2.0\%$ is plotted in Fig. 3.11a. The test was stopped at zero load after reaching the maximum compressive strain, and the inverse pole figure map shows that the *c* axis of several grains was reoriented nearly 90° from ND towards RD and the $<11\bar{2}0>$ or $<10\bar{1}0>$ axes became parallel to the ND. This texture change is consistent with the activation of tension twins. In addition, although partial de-twinning took place during unloading [47], many elongated twin bands are visible in the microstructure (Fig. 3.11c). They were also identified as tension twins because of the orientation with respect to the parent grain and the grain boundary misorientation angle of around 86° (Fig. 3.11b). The twin area fraction was 28%, indicating the importance of the twinning/de-twinning during cyclic deformation.

The SEM images of the specimens deformed along RD at $\Delta\varepsilon/2 = 2.0\%$ and $\Delta\varepsilon/2 = 0.4\%$ are shown in Figs. 3.11c and 3.11e, respectively. It is important to mention that only a few slip/twin traces are marked in the SEM image in Fig. 3.11. Deformation bands were not evident in every grain either because the twin boundaries did not extend to the grain surface or because the orientation of the basal slip system was parallel to the grain surface and did not lead to any traces. However, they do indicate the dominant deformation mechanisms in this orientation. Pyramidal slip bands and elongated tensile twins were the main deformation mechanisms identified in the samples deformed along RD at $\Delta\varepsilon/2 = 2\%$ (Fig. 3.11c). There was only one basal slip trace in the sample deformed along RD at $\Delta\varepsilon/2 = 2\%$ and it is presented in Fig. 3.11d, even though basal slip should likewise be active at this cyclic strain semi-amplitude in this orientation because of the reduced CRSS to activate this mechanism. However, the region in Fig. 3.1e had a very strong basal texture (stronger than the average one), and the majority of the basal planes were (nearly) parallel to the RD-TD plane. As a result, the Burgers vectors of the basal dislocations were (nearly) parallel to the surface and did not lead to slip traces on the surface. In contrast, many

basal slip traces were found on the surface of the specimen deformed along RD at $\Delta\varepsilon/2$ = 0.4% (Fig. 3.11e) in the region in which the grains were suitably oriented for basal slip (Fig. 3.1c).

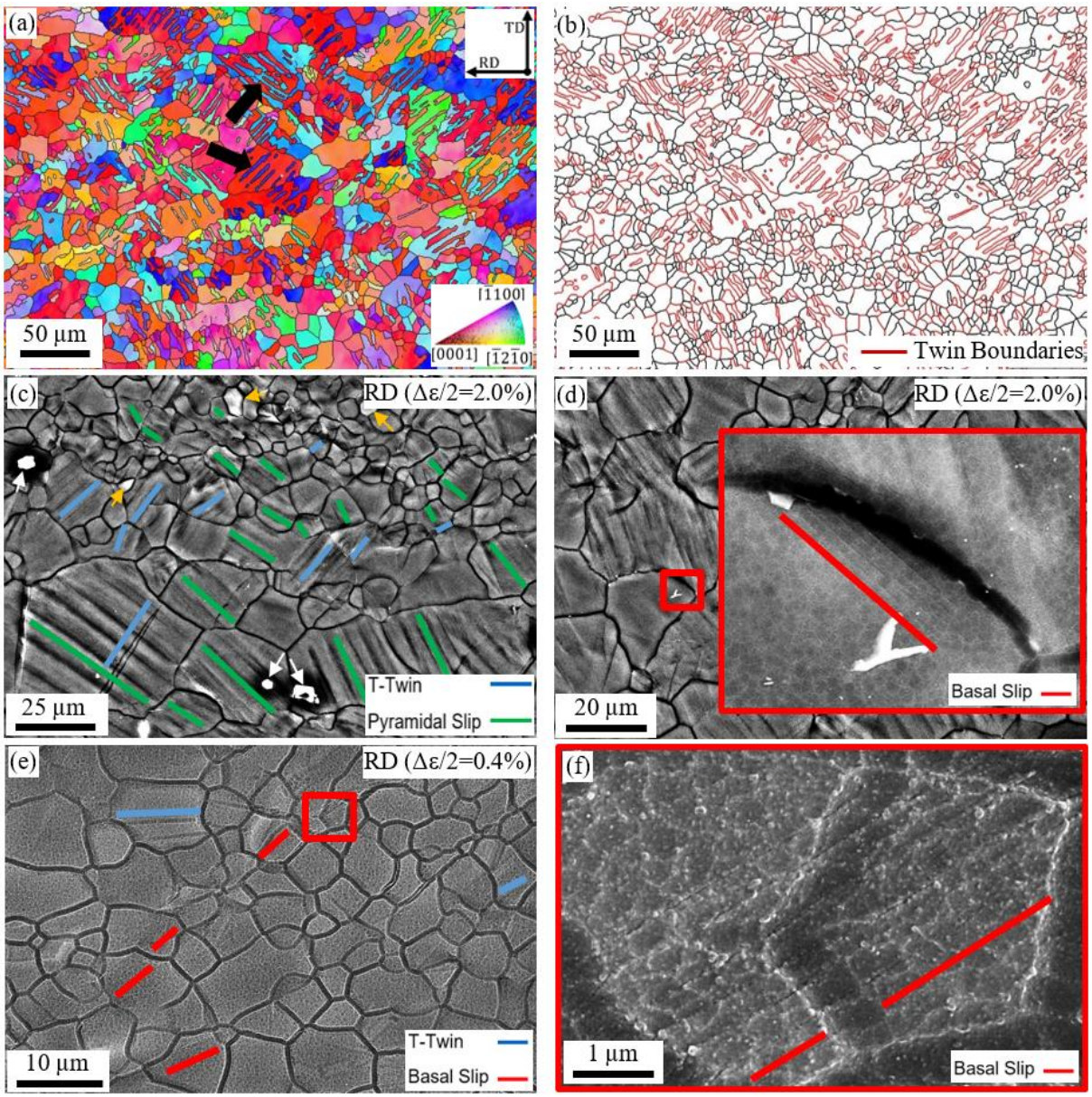

Figure 3.11 – (a) EBSD map and (b) grain boundaries and twin boundaries of the specimen deformed along RD at $\Delta\varepsilon/2$ = 2.0% after 50 cycles. Tension twins are marked with black arrows in (a). Secondary electron image showing slip bands and elongated twins within the grains after (c) 50 cycles at $\Delta\varepsilon/2$ = 2.0% along RD, and (e) 500 cycles at $\Delta\varepsilon/2$ = 0.4% along RD. (d) The only one basal slip trace found in the sample deformed along RD at $\Delta\varepsilon/2$ = 2.0% after 50 cycles. (f) Higher magnification of the region within the red rectangle in (e). Following slip/twin trace analysis, those parallel to red lines were

identified as basal slip bands, those parallel to the blue lines were tensile twins, and those parallel to the green lines stand for pyramidal slip bands.

The basal slip traces are always very fine and can be seen more clearly in Fig. 3.11f, which shows the area marked with a red rectangle in Fig. 3.11e at higher magnification. It should be noted that the absence of pyramidal slip traces in this specimen indicates that the stresses during the tensile part of the fatigue cycle were insufficient to produce pyramidal slip bands due to the low strain semi-amplitude of 0.4%. However, pyramidal slip should be present in these samples to explain the asymmetry between the maximum and minimum stress in each fatigue cycle (Fig. 3.3). In addition, Shi et al. [92] analyzed the strain-controlled fatigue deformation mechanism in a hot-rolled AZ31B Mg alloy and have also shown that the basal slip and twinning were activated along RD and ND at the strain semi-amplitude of $\Delta\varepsilon/2 = 1\%$.

A large effort was carried out to look for slip traces and twins in more than two thousand grains at different cyclic strain semi-amplitudes in RD to get quantitative data regarding the predominant deformation mechanisms. The results of this analysis are depicted in Table 3.1. The fraction of the grains with slip traces ot twin bands in the specimens deformed along RD was reduced from 25.6% ($\Delta\varepsilon/2 = 2\%$) to 7.2% ($\Delta\varepsilon/2 = 0.4\%$) when the cyclic strain semi-amplitude decreased. Pyramidal slip bands have the highest fraction (72.3%) in the sample deformed along RD at $\Delta\varepsilon/2 = 2\%$ (Table 3.1). In addition, both pyramidal slip bands and elongated twins appeared in the same grain in 9.1% of the grains, showing that both mechanisms can be active simultaneously due to the grain orientation. The large tension-compression anisotropy in the cyclic stress-strain curves, which was caused by the activation of pyramidal slip during the tensile part of the cycle, is consistent with these observations.

According to slip trace analysis along RD at $\Delta\varepsilon/2 = 0.4\%$ (Table 3.1), the primary deformation mechanisms were elongated twins and basal slip bands, which were found in 170 grains of the studied area in the deformed specimen (Table 3.1). Very few grains are well oriented for the basal slip because of the strong basal texture, which means that the deformation must be accommodated in fewer grains, which take up more plastic deformation. As a result, the presence of basal slip bands is limited. In fact, it was common to find basal slip traces in elongated clusters of tiny grains that were suitably oriented for

basal slip. These clusters of grains in which deformation was localized were oriented parallel to the basal slip traces (Fig. 3.1c), and (as it will be demonstrated in the next chapter), they were important from the viewpoint of crack nucleation. Although it seems that pyramidal slip was also active in this specimen based on the asymmetry in the maximum stresses in tension and compression, the cyclic strain semi-amplitude was probably too low to promote the development of pyramidal slip bands on the surface. It should be noted that the pyramidal slip traces were not found in the fatigue of AZ31 Mg alloy at $\Delta\varepsilon/2 = 1\%$ along RD and ND by Shi et al. [92].

Table 3.1 – Deformation mechanisms from slip/twin trace analysis in RD.

Orientation	RD	
$\Delta\varepsilon/2$ (%)	0.4	2.0
Number of grains analyzed	2348	2100
Number of grains with traces	170	538
Elongated tensile twins	61.2%	18.4%
Basal slip	38.8%	0.2%
Pyramidal slip	-	72.3%
Pyramidal slip & tensile twins	-	9.1%

3.4. Cyclic Deformation Mechanisms in 45° RD-ND

The surface of the specimens deformed along 45° RD-ND was examined in the SEM after 1/5 of the fatigue life to reveal the main deformation mechanisms as a function of the cyclic strain semi-amplitude. The EBSD maps showing the grain orientation in one region of the specimen deformed along 45° RD-ND before deformation and after 1200 fatigue cycles are depicted in Figs. 3.12a and 3.12b, respectively. The test was stopped at zero load after the maximum compressive strain was reached. This region has random grain orientation, and the deformed specimen shows elongated twins (shown by arrows) (Fig. 3.12b). The analysis of the grain boundary misorientation angle in this region (Fig. 3.12c) showed that these twin boundaries corresponded to tension twins (grain boundary misorientation $\approx 86^{\circ}$). They were nucleated during the compressive part of the fatigue cycle and did not disappear by detwinning during unloading [65,197].

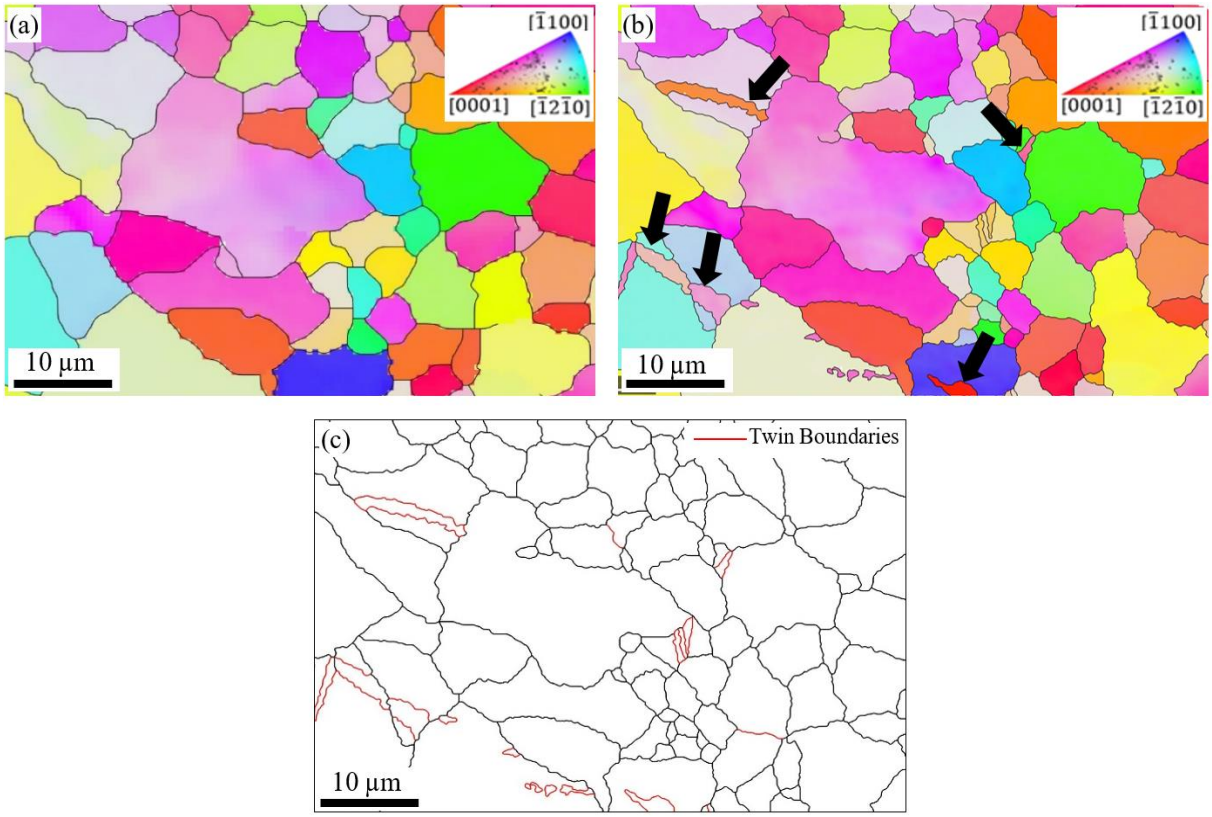

Figure 3.12 – EBSD maps of one region of the specimen deformed along 45° RD-ND. (a) Before deformation. (b) After 1200 fatigue cycles. (c) Grain boundaries and twin boundaries after deformation, the latter marked with red lines. The test was stopped at the maximum compressive strain. Tensile twins in (b) are marked with arrows.

Figs. 3.13a and 3.13b display examples of slip trace analysis for the specimens deformed along 45° RD-ND at $\Delta\varepsilon/2$ = 2% and 0.4%, respectively. The specimen deformed along 45° RD-ND at $\Delta\varepsilon/2$ = 2% had basal slip bands and elongated bands parallel to the twins (depicted with red and blue lines, respectively). However, the specimen deformed along 45° RD-ND at $\Delta\varepsilon/2$ = 0.4% only had elongated bands parallel to tensile twins (Fig. 3.13b). One explanation for the lack of basal slip traces in the grains of the specimen deformed along 45° RD-ND and $\Delta\varepsilon/2$ = 0.4% is that the deformation was consistently distributed over different basal slip planes in all grains, and most of the grains were suitably oriented for basal slip. Hence, the secondary electron images obtained from the SEM did not show deformation localization in slip bands in a few grains in the area that has been studied. However, basal slip bands appeared in many grains when the cyclic strain semi-amplitude was 2% because the basal slip was localized (Fig. 3.13a). It has been shown that the basal slip traces are visible in the fatigue of AZ31 Mg alloy along 45° RD-

ND at $\Delta\varepsilon/2$ = 1% [92]. These deformation mechanisms (basal slip and twinning) in the samples deformed along 45° RD-ND (representative of Mg alloys with weak basal texture) are in good agreement with the results of the deformation mechanism in the fatigue of AZ31 Mg alloy along 45° RD-ND and weakly textured Mg–3wt.% Y alloy deformed at $\Delta\varepsilon/2$ = 1% [92,93,98,198].

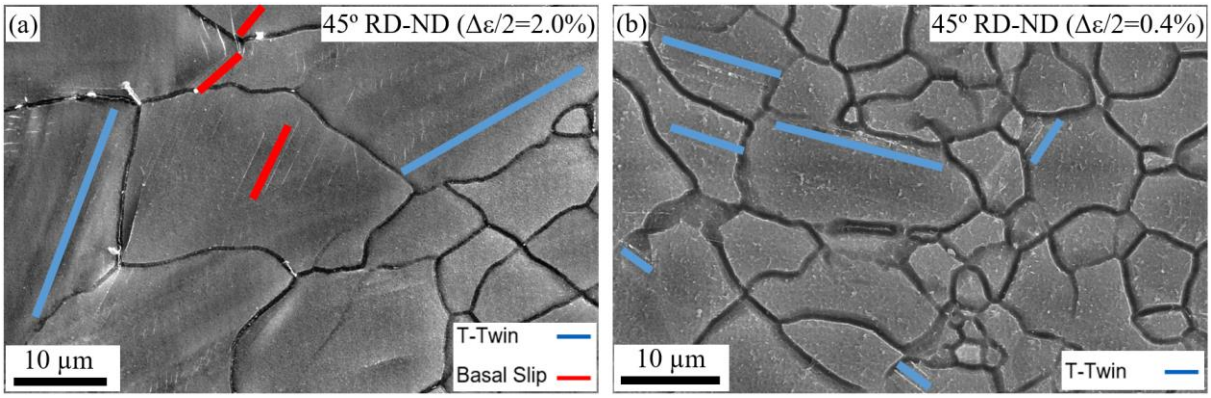

Figure 3.13 – Secondary electron image showing slip bands and elongated twins within the grains along 45° RD-ND after (a) 1200 cycles at $\Delta\varepsilon/2$ = 0.4% and (b) 50 cycles at $\Delta\varepsilon/2$ = 2.0%. Following slip/twin trace analysis, those parallel to the red lines were identified as basal slip bands, and those parallel to the blue lines were tensile twins.

A massive effort was put into looking for slip traces and twins in the specimens deformed along 45° RD-ND at $\Delta\varepsilon/2$ = 2% and 0.4% in 4515 and 1544 grains, respectively, to get quantitative information regarding the main deformation mechanisms in these specimens (Table 3.2). According to the slip trace analysis, 16% of the grains (248 out of 1544) showed traces (either basal slip or twin band) in the specimen deformed along 45° RD-ND at $\Delta\varepsilon/2$ = 2%, and approximately one-half of them were elongated twin bands. The other half were basal slip traces, which appeared due to the slip localization being triggered at higher cyclic strain semi-amplitude. The fraction of the grains with traces decreased to 3.8% by reducing the strain semi-amplitude to 0.4% in the specimens deformed along 45° RD-ND, all of which were tension twin bands (Table 3.2). However, it is essential to mention that basal slip should also be a dominant deformation mechanism because most grains were suitably oriented for basal slip [65,68,92,198] but slip traces did not appear because the deformation was not localized in a few slip planes.

Table 3.2 – Deformation mechanisms from slip/twin trace analysis in 45º RD-ND.

Orientation	45º RD-ND	
$\Delta\varepsilon/2$ (%)	0.4	2.0
Number of grains analyzed	4515	1544
Number of grains with traces	171	248
Elongated tensile twins	100%	52.4%
Basal slip	-	47.6%

4. FATIGUE CRACK INITIATION MECHANISMS

4.1. Fatigue Crack Initiation Mechanisms in RD

Fatigue crack initiation sites in the specimens deformed along RD at $\Delta\varepsilon/2$ = 2% and 0.4% were analyzed at higher magnification with secondary electrons in the same region where the deformation mechanisms were studied (Figs. 4.1 and 4.2). The detection of 496 cracks in the specimen deformed along RD at $\Delta\varepsilon/2$ = 2% shows that microcracking was widespread after 33% of fatigue life (Table 4.1). However, the number of observed cracks was reduced to 152 cracks by decreasing the cyclic strain semi-amplitude to 0.4% in RD (Table 4.1). This large number of cracks at each cyclic strain semi-amplitude led to statistically relevant results. Intergranular (crack at grain boundaries) and transgranular (cracks parallel to pyramidal slip or twin bands) cracks were discovered in the specimens deformed along RD at different cyclic strain semi-amplitudes (Fig. 4.1 and 4.2), in agreement with previous studies [89,94–96,200]. Notably, the dominant fatigue crack initiation sites were intergranular cracks at both strain semi-amplitudes in RD (57.2% at $\Delta\varepsilon/2$ = 2% and 62.5% at $\Delta\varepsilon/2$ = 0.4%, Table 4.1). Figs. 4.1 and 4.2 show the crack initiation sites in the specimens deformed along RD at $\Delta\varepsilon/2$ = 2% and 0.4%, respectively. A grain boundary crack has nucleated around a small grain which is totally twinned due to the eigenstrain associated with the twinning (Figs. 4.1a and 4.1b,). Examples of transgranular cracks parallel to pyramidal slip bands (33.9% of total cracks, Table 4.1) and tension twin bands (8.1% of total cracks, Table 4.1) in this specimen are displayed in Figs. 4.1c,d and 4.1e,f, respectively. The latter was linked to the large grains (Figs. 4.1e and 4.1f).

The grain boundary crack initiated at the triple point in the specimen deformed along RD at $\Delta\varepsilon/2$ = 0.4% is marked with a yellow rectangle in Figs. 4.2a and 4.2c. The cracks parallel to the basal slip bands (red rectangle in Fig. 4.2a and 4.2b) were the second fatigue crack initiation mechanism (32.9%, Table 4.1), and they nucleated in clusters of grains suitably oriented for basal slip. The secondary images obtained from the SEM after 500 and 800 cycles for the sample deformed along RD at $\Delta\varepsilon/2$ = 0.4% are shown in Figs. 4.3a and 4.3b, respectively. It is obvious from Fig. 4.3 that the cracks parallel to the basal slip band were initiated in a cluster of grains properly oriented for basal slip, and

propagated through the grain boundaries to link several grains after 300 more cycles. Moreover, a few cracks parallel to the elongated twin boundaries in large grains were also found (4.5%, Table 4.1) (Fig. 4.2d and 4.2e).

The fatigue crack initiation sites along RD were studied in more than 2000 grains in each strain semi-amplitude ($\Delta\varepsilon/2$ = 2% and 0.4%) (Table 4.1). The results indicated two different mechanisms: Transgranular cracks parallel to the slip bands (either pyramidal or basal slip) or tension twin bands and intergranular cracks at triple junctions or grain boundaries. The transgranular cracks parallel to the pyramidal slip bands were not found in the specimen deformed along RD at $\Delta\varepsilon/2$ = 0.4% due to the limited number of pyramidal slip bands. However, this mechanism was the main transgranular crack initiation mechanism in the specimen deformed along RD at $\Delta\varepsilon/2$ = 2%. Furthermore, a few transgranular cracks parallel to the twin boundaries were found at both cyclic strain semi-amplitudes.

Table 4.1 – Fatigue crack initiation locations as a function of cyclic strain semi-amplitude in RD. IC stands for intergranular cracking, and TC for transgranular cracking.

Orientation	RD	
$\Delta\varepsilon/2$ (%)	2.0	0.4
Number of Cracks	496	152
Grain Boundary Crack (IC)	57.2%	62.5%
Basal Slip Band Crack (TC)	-	32.9%
Pyramidal Slip Band Crack (TC)	33.9%	-
Tensile Twin Boundary Crack (TC)	8.1%	4.6%

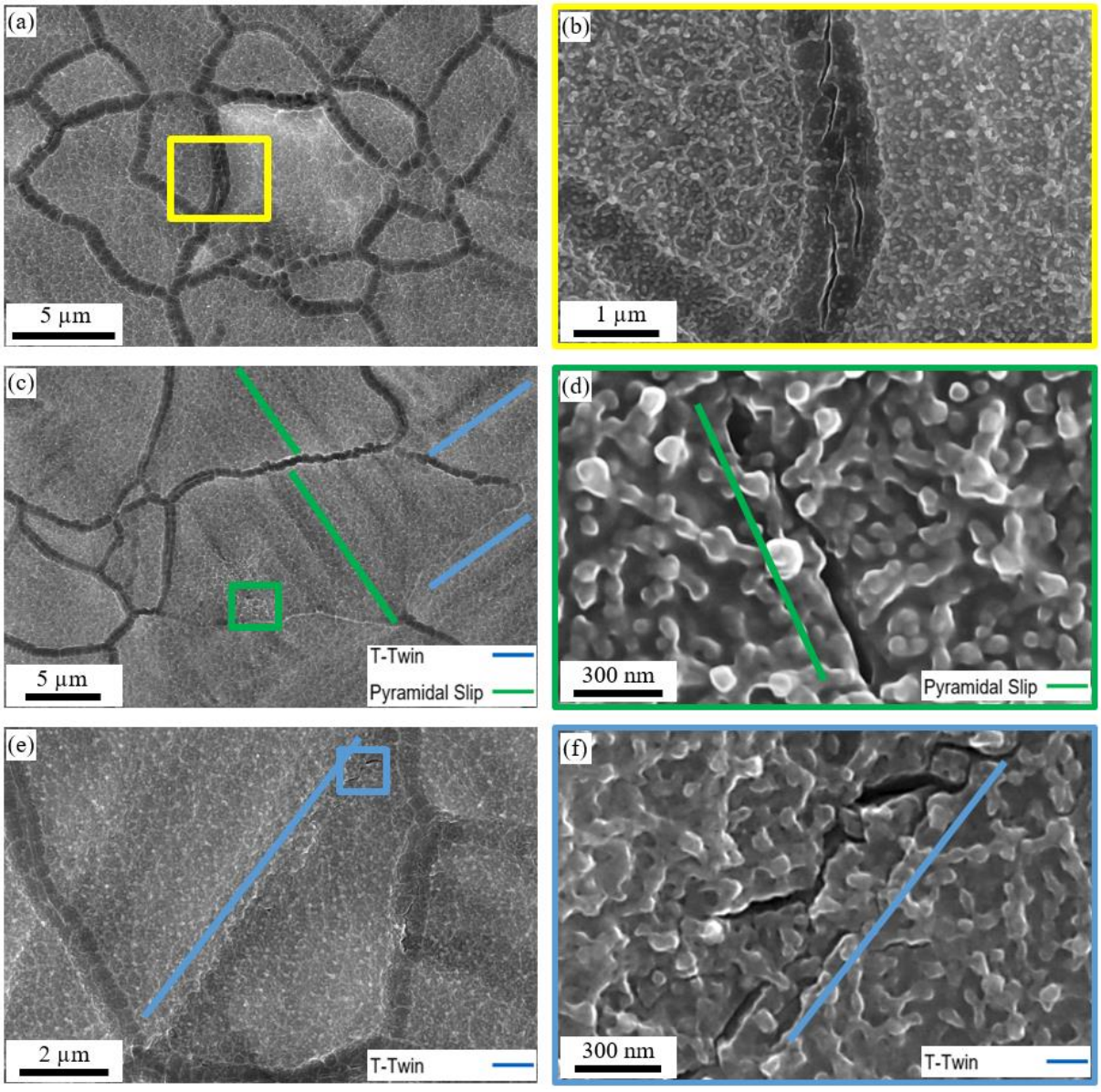

Figure 4.1 – Fatigue crack initiation sites in the rolled AZ31B-O sample after 50 fatigue cycles at $\Delta\varepsilon/2$ = 2.0% along RD. (a) Intergranular crack at a grain boundary around a fully-twinned small grain. (b) Higher magnification of the region within the yellow rectangle in (a). (c) Crack parallel to pyramidal slip band. (d) Higher magnification of the region within the green rectangle in (c). (e) Transgranular crack parallel to tensile twin. (f) Higher magnification of the region within the blue rectangle in (e).

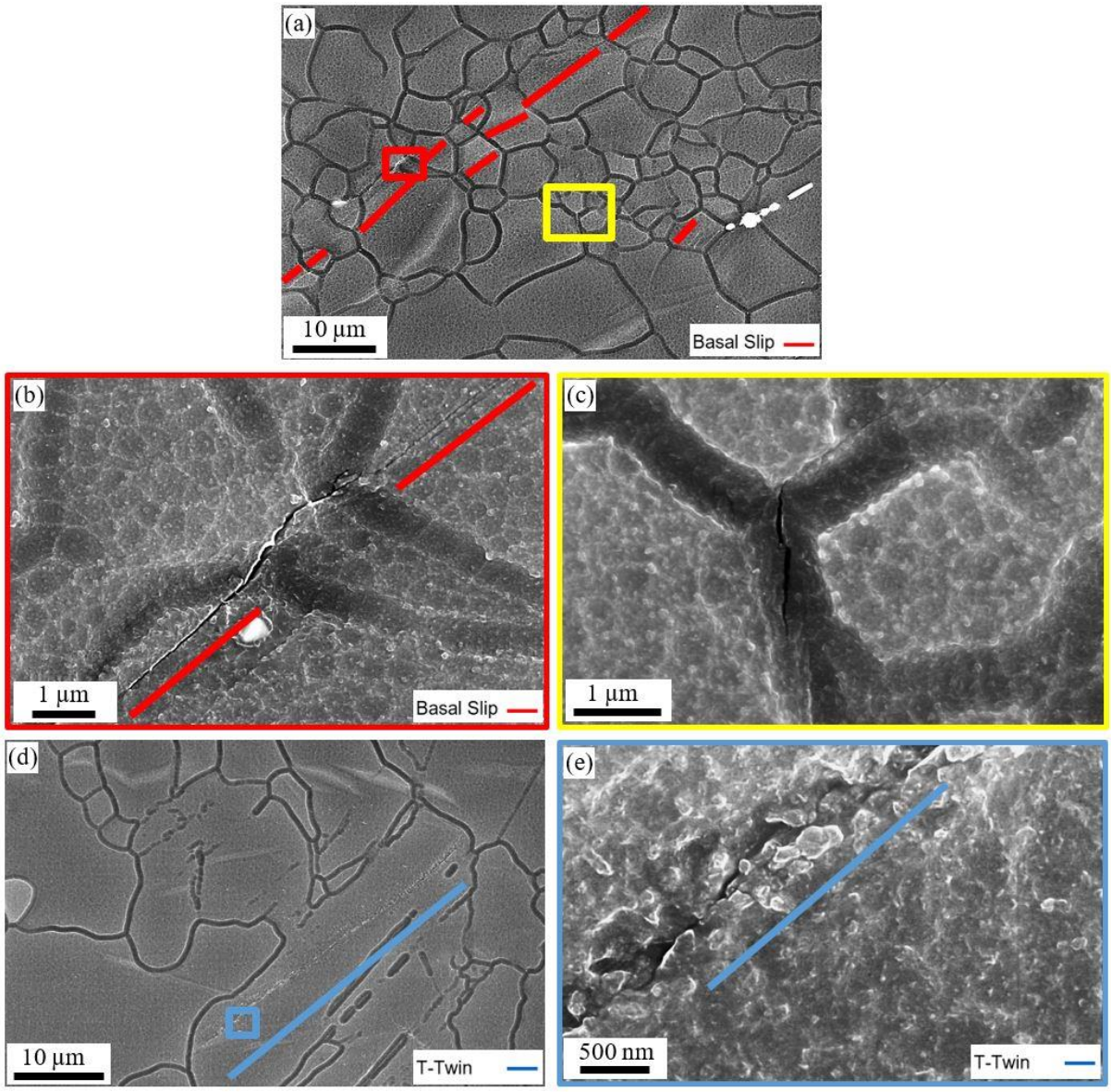

Figure 4.2 – Fatigue crack initiation sites in the rolled AZ31B-O sample after 500 fatigue cycles at $\Delta\varepsilon/2 = 0.4\%$ along RD. (a) Intergranular cracks near a cluster of grains with almost parallel basal slip traces (yellow rectangle) and at a triple point (red rectangle). (b) Higher magnification of the yellow rectangle in (a). (c) Higher magnification of the red rectangle in (a). (d) Crack parallel to a twin. (e) Higher magnification of the region within the blue rectangle in (d).

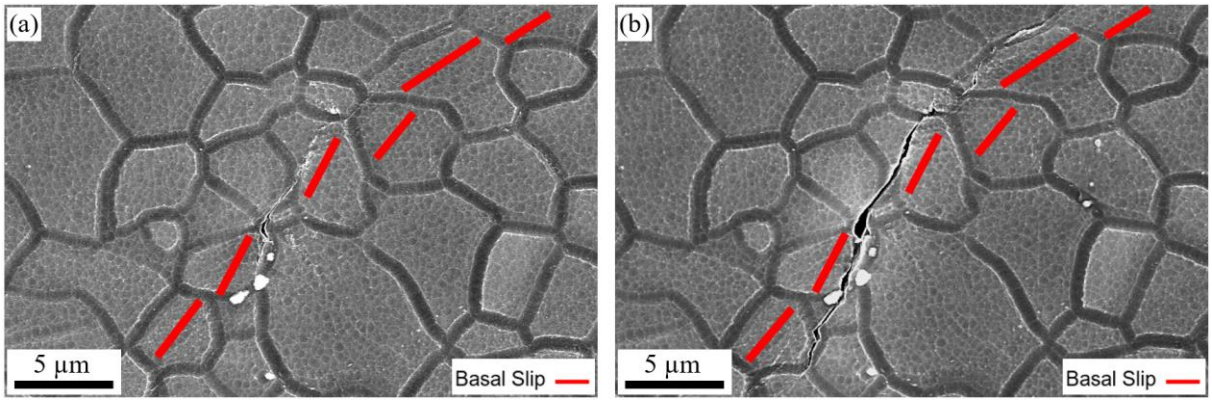

Figure 4.3 – Fatigue crack parallel to the basal slip bands in the rolled AZ31B-O sample at $\Delta\varepsilon/2$ = 0.4% along RD after (a) 500 fatigue cycles and (b) 800 fatigue cycles.

The probability of cracking as a function of the grain size for the different types of crack initiation sites in the specimens deformed along RD is plotted in Figs. 4.4a and 4.4b for $\Delta\varepsilon/2$ = 2% and 0.4%, respectively. Less than 20% of grains smaller than 20 μm presented intergranular or transgranular cracks (associated with twin boundaries or basal/pyramidal slip bands), while grain boundary cracking was dominant in these smaller grains (Fig. 4.4a and 4.4b). These transgranular or intergranular cracks around or through small grains were often short and less important from the propagation perspective until failure. Transgranular cracks in clusters of grains that were appropriately aligned for basal slip were the only exception (Figs. 4.2a and 4.3a). They expanded quickly by connecting cracks that ran parallel to the basal slip bands in various grains, and they had the potential to reduce the fatigue strength. In contrast, more than 60% of the grains > 30 μm were cracked after 33% of the fatigue life. The transgranular cracks in large grains (> 30 μm) were parallel to the pyramidal slip bands or along the tension twin bands at $\Delta\varepsilon/2$ = 2% and 0.4%, respectively. They covered the whole grain width (for example, look at Figs. 4.2d and 4.2a) and were most likely to propagate until failure.

In addition, Fig. 4.4c displays the influence of grain boundary misorientation angle on the probability of fatigue crack nucleation at grain boundaries in the specimens deformed along RD. Some grain boundary cracks were related to the small fully twinned grains in the specimen deformed along RD at $\Delta\varepsilon/2$ = 2% (Fig. 4.1a and 4.1b), and the grain boundary cracks appeared due to the stress concentration induced by the twinning

eigenstrain. However, only 11 grains had this mechanism visible in the specimen deformed along RD at $\Delta\varepsilon/2 = 2\%$. As demonstrated in Fig. 4.4c, most grain boundary cracks were linked with the high values of the grain boundary misorientation angle rather than twinning or the interaction of slip bands or twins with the grain boundary when the material deformed along RD at $\Delta\varepsilon/2 = 2\%$. In fact, when the grain boundary misorientation is > 40°, the proportion of grain boundaries that initiate fatigue cracks grows dramatically, and 70% of grain boundaries with a misorientation angle between 65° and 90° were cracked. On the other hand, just 3% of the grain boundaries with a misorientation angle of < 40° were broken. A clear explanation for this phenomenon is not available, although it may be probably created due to the incompatibility of deformation between adjacent grains, which is more likely to occur in small grains because the critical stress to nucleate twins or promote slip increases as the grain size decreases. Higher tensions are thus achieved at the grain boundaries, which encourages grain boundary cracking. In contrast, there is no relation between grain boundary cracking and grain boundary misorientation angle at low cyclic strain semi-amplitude of 0.4% (Fig. 4.4c).

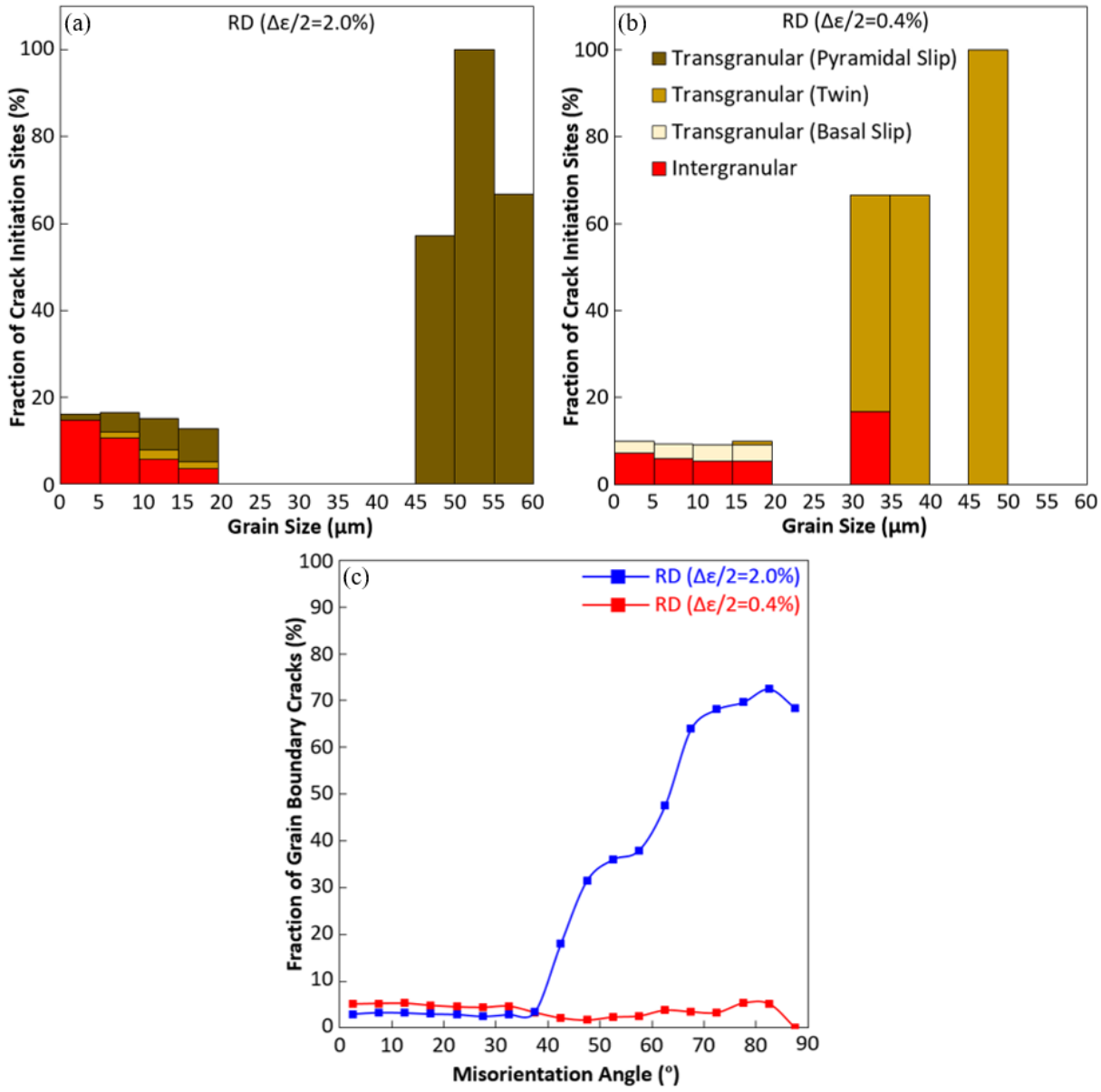

Figure 4.4 – (a) Fraction of crack initiation sites as a function of grain size for each crack initiation mechanism in the specimen deformed along RD at $\Delta\varepsilon/2 = 2\%$. (b) Idem at $\Delta\varepsilon/2 = 0.4\%$. (c) Fraction of intergranular cracks as a function of the grain boundary misorientation angle in the specimens deformed along RD.

4.2. Fatigue Crack Initiation Mechanisms in 45° RD-ND

Higher magnification secondary images, in the same area where the deformation mechanisms were investigated, were used to find the fatigue crack nucleation sites in the specimens deformed along 45° RD-ND at $\Delta\varepsilon/2$ = 2% and 0.4%. Because of the large size of the studied region, 200 to 300 cracks were found for each cyclic strain semi-amplitude (Table 4.2), resulting in statistically significant results. The different crack initiation sites for the samples deformed along 45° RD-ND at $\Delta\varepsilon/2$ = 2% and 0.4% are depicted in Figs. 4.5 and 4.6, respectively. The dominant crack nucleation sites in the specimen deformed along 45° RD-ND at $\Delta\varepsilon/2$ = 2% were intergranular cracks (mainly occurred in triple points) (67%, Table 4.2), and one example is shown in Fig. 4.5a. It has been shown by Shi et al. [92] that the grain boundary cracks are dominant in the fatigue of AZ31 Mg alloy along 45° RD-ND at $\Delta\varepsilon/2$ = 1%, and they were 60.5% of the total number of cracks. The number of transgranular crack parallel to the basal slip bands is shown in Figs. 4.5b (the fraction was 4.5%, Table 4.2). Furthermore, Figs. 4.5c and 4.5d show cracks parallel to the tension twin bands, which were observed in 14.5% of the studied grains (Table 4.2). Finally, Figs. 4.5d and 4.5e present clusters of short cracks parallel to the basal slip plane orientation. This type of cracks was also observed by other researchers during fully reversed strain-controlled fatigue of extruded AZ31 Mg alloy at $\Delta\varepsilon/2$ = 1% [89] and it is most likely related to the basal slip activation inside the tension twin bands during the tension or compressive part of the fatigue cycle (twinned regions are properly oriented for basal slip). Nonetheless, the fraction of these clusters is limited (13.9%, Table 4.2), and they never propagated. As a result, they do not appear to be important in terms of fatigue failure. However, the dominant fatigue crack initiation mechanism in the specimen deformed along 45° RD-ND at $\Delta\varepsilon/2$ = 0.4% was the cracks which were initiated at the tension twin/matrix boundary (73.1%, Table 4.2). Figs. 4.6a and 4.6b indicate one example of this type of crack. Intergranular crack, found in 27% (Table 4.2) of the grains in the studied area (including triple points), is depicted in Fig. 4.6c. Transgranular cracks initiated at the tension twin/matrix boundary propagated along the grain boundaries, as shown in Fig. 4.6d. No other fatigue crack nucleation sites were observed in this specimen.

Table 4.2 – Fatigue crack initiation locations as a function of cyclic strain semi-amplitude in RD. IC stands for intergranular cracking, and TC for transgranular cracking.

Orientation	45° RD-ND	
$\Delta\varepsilon/2$ (%)	2.0	0.4
Number of Cracks	289	212
Grain Boundary Crack (IC)	67.1%	26.9%
Basal Slip Band Crack (TC)	4.5%	-
Tensile Twin Boundary Crack (TC)	14.5%	73.1%
Basal Slip Band Crack within Tension Twin (TC)	13.9%	-

The statistical analysis of fatigue crack initiation sites along the 45° RD-ND in 1544 and 4515 grains at $\Delta\varepsilon/2$ = 2% and 0.4%, respectively, resulted in two different mechanisms: intergranular cracks nucleated at grain boundaries and triple points, and transgranular cracks appeared parallel to the twins or basal slip. The grain boundary cracks were the main mechanism at high cyclic strain semi-amplitudes ($\Delta\varepsilon/2$ = 2%), and the cracks at twin/matrix boundary dominate at low cyclic strain semi-amplitudes ($\Delta\varepsilon/2$ = 0.4%). One possible reason for this large difference in the fraction of intergranular cracks in this sample at different strain semi-amplitudes is that the basal slip was much more active at $\Delta\varepsilon/2$ = 2% (Fig. 3.13a and Table 3.2) in comparison with $\Delta\varepsilon/2$ = 0.4%. As a result, the stress concentrations were facilitated at grain boundaries and triple junctions, and crack initiation followed. These types of cracks were consistent with the previous studies on the fatigue crack initiation of weakly textured Mg alloys [92,94].

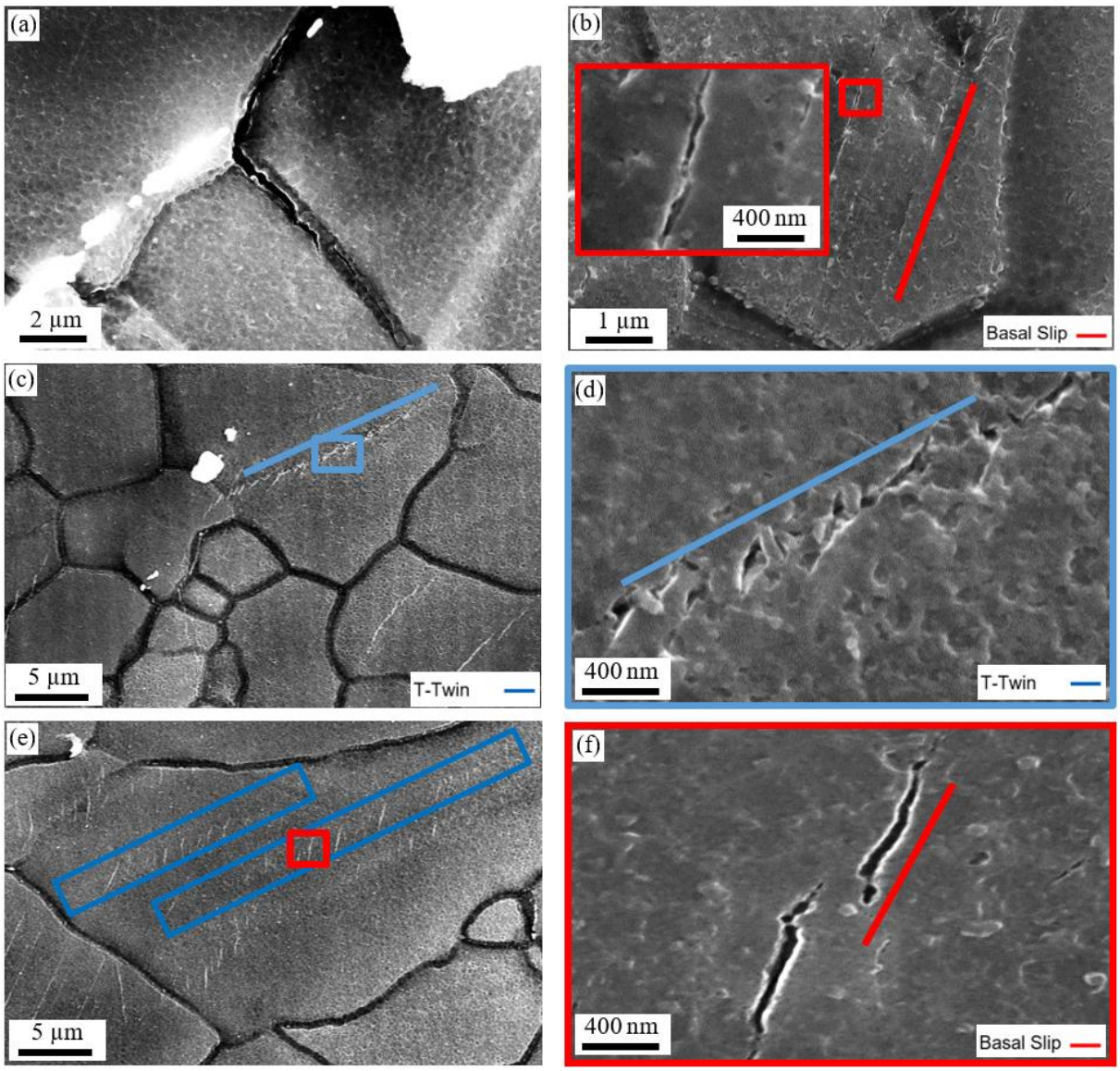

Figure 4.5 – Fatigue crack initiation sites in the rolled AZ31B-O sample after 50 fatigue cycles at $\Delta\varepsilon/2$ = 2.0% along 45° RD-ND. (a) Intergranular crack at a grain boundary triple junction. (b) Transgranular crack parallel to the basal slip plane orientation (c) Crack parallel to a twin. (d) Higher magnification of the region within the blue rectangle in (c). (e) Short cracks parallel to the traces of basal planes within the twins. (f) Higher magnification of the region within the red rectangle in (e) shows the short cracks parallel to the traces of basal planes within the twins.

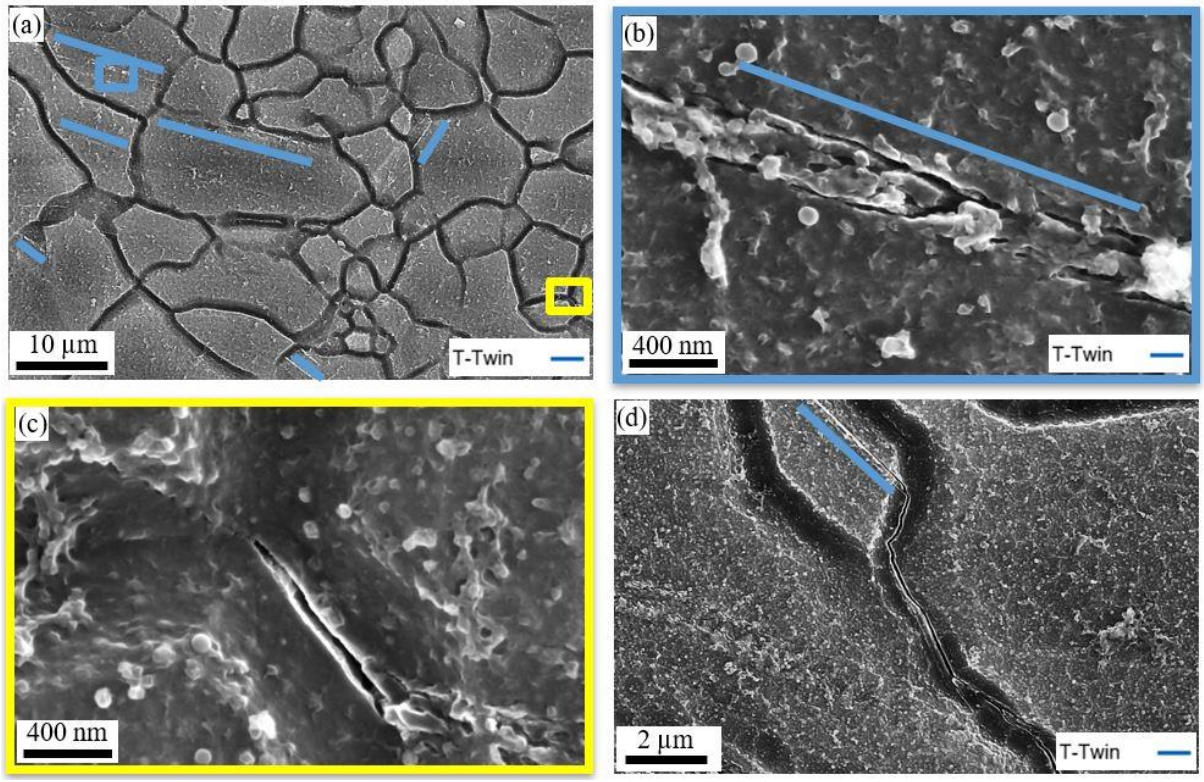

Figure 4.6 – (a) Fatigue crack initiation sites in the rolled AZ31B-O sample after 1200 fatigue cycles at $\Delta\varepsilon/2$ = 0.4% along 45° RD-ND. (a) Crack parallel to twin. (b) Higher magnification of the region within the blue rectangle in (a). (c) Higher magnification of a grain boundary crack at a triple point within the yellow rectangle in (a). (d) Propagation along the grain boundary of a crack nucleated parallel to a twin.

Figs. 4.7a and 4.7b show the probability of the cracking as a function of grain size for intergranular and transgranular cracks in the specimen deformed along 45° RD-ND at $\Delta\varepsilon/2$ = 2.0%, 0.4%, respectively. These findings clearly illustrate that the grain boundaries are the preferential crack nucleation sites in the small grains of both strain semi-amplitudes. However, the cracks preferred to be nucleated at the tension twins/matrix boundary in large grains. Notably, the probability of initiating a fatigue crack is very high in large grains (above 40%), and these cracks are very long because they cover the entire width of the large grain. Consequently, large grains, which were well oriented for twinning, seem to be the preferential site for initiating fatigue cracks leading to failure in specimens in which basal slip and tensile twinning are the dominant deformation mechanisms. Finally, the effect of grain boundary misorientation angle on the probability of initiating a crack at the grain boundaries was studied. The results are depicted in Fig. 4.7c. This factor did not play any role in the fatigue crack initiation at

grain boundaries in the specimens deformed along 45° RD-ND at both $\Delta\varepsilon/2$ = 0.4% and 2%. However, the crack initiation probability increases with $\Delta\varepsilon/2$.

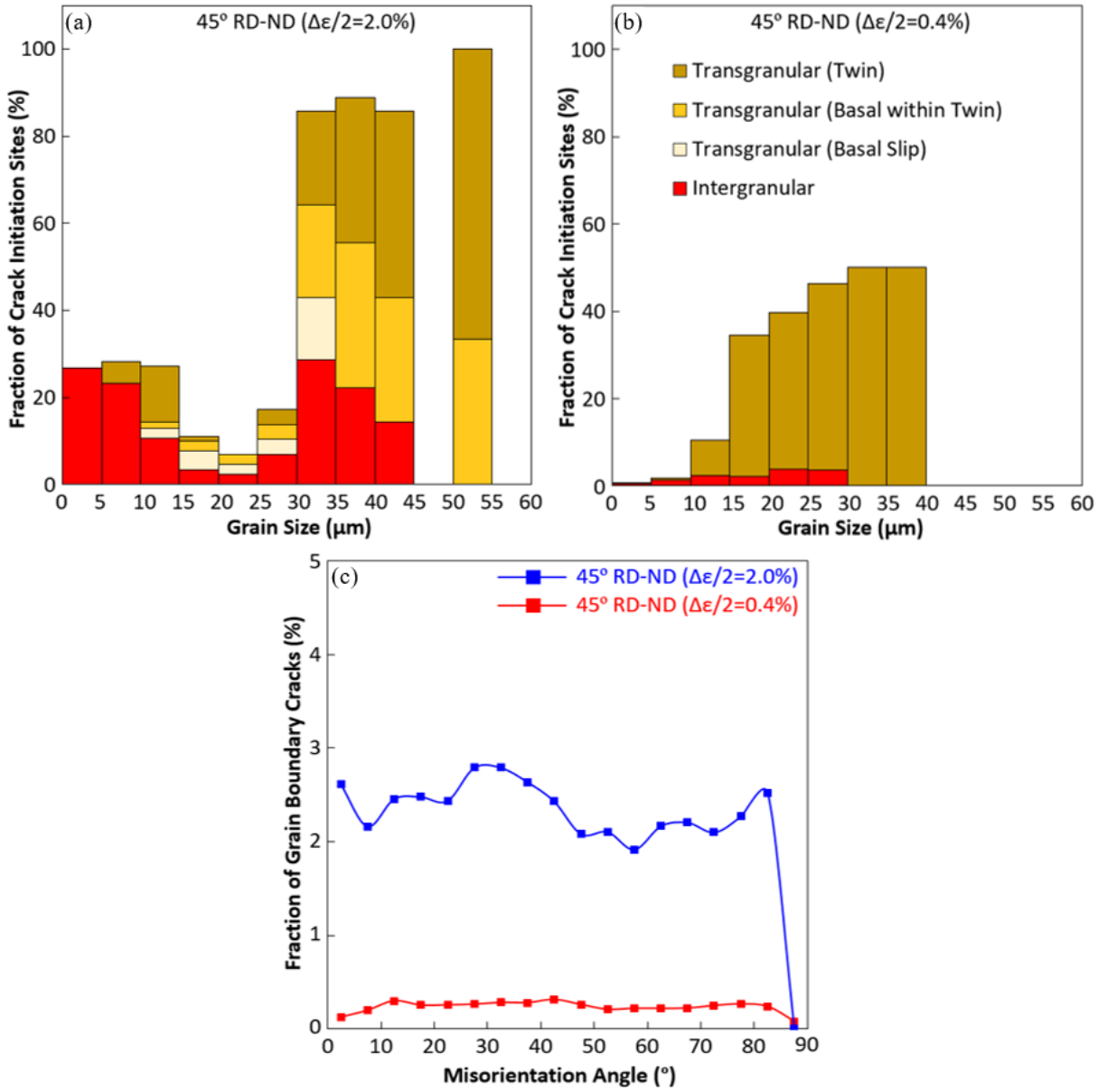

Figure 4.7 – (a) Fraction of crack initiation sites as a function of grain size for each crack initiation mechanism in the specimen deformed along 45° RD-ND at $\Delta\varepsilon/2$ = 2%. (b) *Idem* at $\Delta\varepsilon/2$ = 0.4%. (c) Fraction of intergranular cracks as a function of the grain boundary misorientation angle in the specimens deformed along 45° RD-ND.

5. COMPUTATIONAL HOMOGENIZATION

The cyclic deformation of the AZ31B Mg alloy along different orientations was simulated by means of the finite element simulation of a Representative Volume Element (RVE) of the material that takes into account the microstructural features of the material in different orientations. A hierarchical sequence of three distinct RVEs (one RVE with voxel tessellation and two RVEs with voronoi tessellation) was used to determine the optimum parameters of the crystal plasticity model that are able to reproduce the cyclic stress-strain curve of the rolled AZ31B Mg alloy in different orientations. Each RVE was created with NEPER [123], an open-source software, and included 200 grains whose the grain size distribution followed the experimental one in Fig. 3.2a. The RVE of the polycrystal was a cubic domain with a regular mesh of 27 × 27 × 27 cubic C3D8R elements of Abaqus in the voxel model (Fig. 5.1a). The Voronoi-type RVEs were meshed with second-order modified tetrahedral element (C3D10M elements with 10 nodes of Abaqus) using Gmsh [201], following the Voronoi tessellation algorithm (Figs. 5.1b and c). The coarser and finer Voronoi type RVEs have 27427 C3D10M elements and 83318 C3D10M elements in Figs. 5.1b and c, respectively.

Periodic boundary conditions were applied along the X, Y, and Z directions of RVEs to simulate the mechanical response. The connections between the displacements of each pair of nodes A and B (which located on opposite surfaces of the domain) were established based on

$$\mathbf{u}_B - \mathbf{u}_A = (\bar{\mathbf{F}} - \mathbf{I})\Delta_{BA} \tag{1}$$

where Δ_{BA} is the distance vector between node B and node A, $\mathbf{I}$ the second order identity tensor. The far-field deformation gradient $\bar{\mathbf{F}}$ applied to the RVE was calculated as following:

$$\mathbf{u}(M_i) = (\bar{\mathbf{F}} - \mathbf{I})\mathbf{e}_i \tag{2}$$

where the orthogonal basis vectors along X, Y, and Z are $\mathbf{e}_i$ with i = 1, 2, 3.

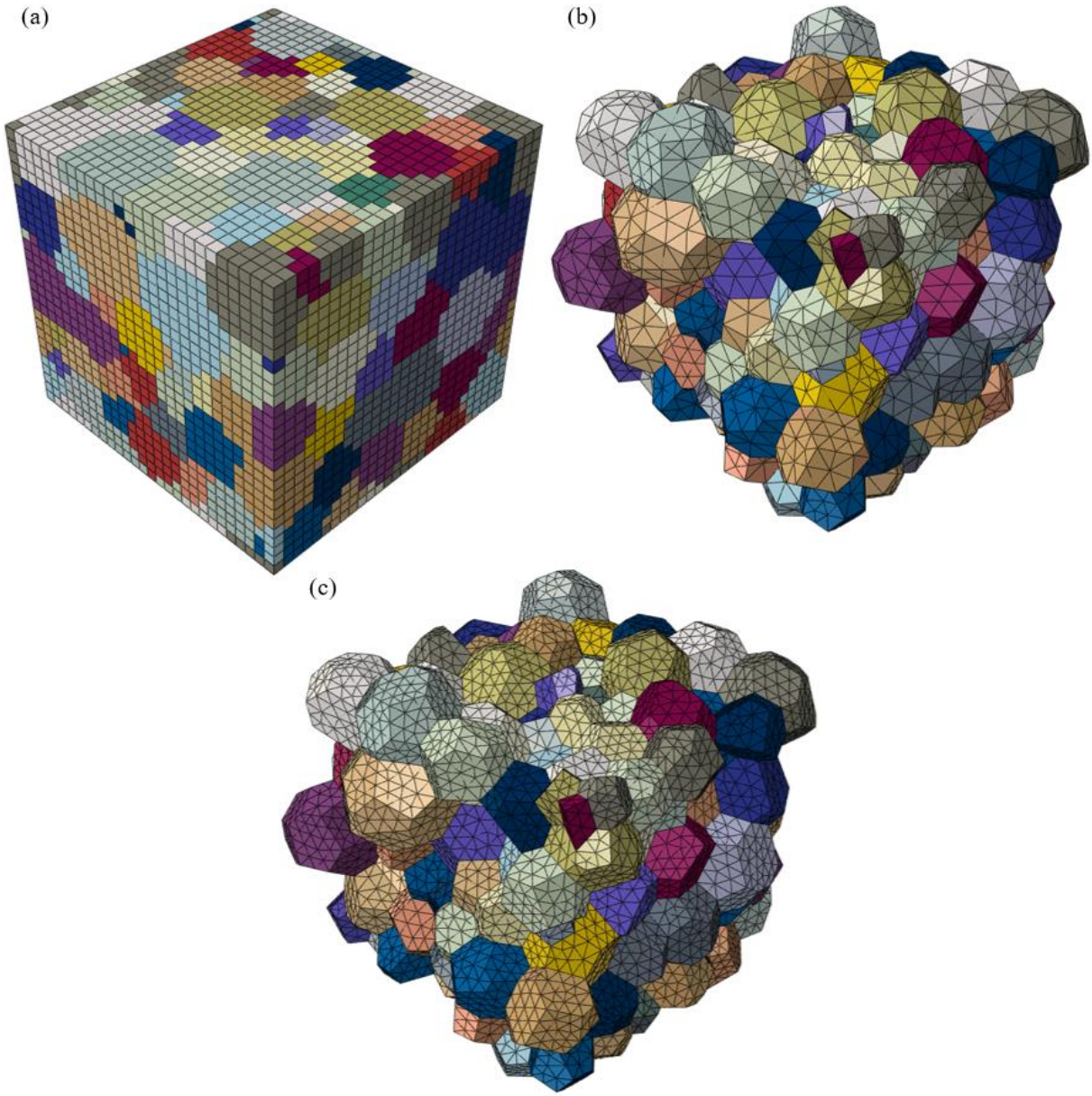

Figure 5.1 – RVEs of the microstructure including 200 grains with (a) voxel type RVE with 19683 C3D8R elements, (b) Voronoi type RVE with 27427 C3D10M elements, and (c) Voronoi type RVE with 83318 C3D10M elements.

The vector $\mathbf{u}(M_i)$ is the displacement of master node M_i normalized by RVE dimension along direction i. Three springs of negligible stiffness, connected to a fixed node inside the RVE, are used to link the master nodes with the microstructure. The displacement of the master nodes is determined by applying a nodal force $\mathbf{P}_j$ to the degree of freedom j of master node M_i according to

$$\mathbf{P}_j\,(M_i) = \left(\overline{\boldsymbol{\sigma}}_{ij}\mathbf{e}_i\right)A \tag{3}$$

where A is the projection of the current area to the of the face perpendicular to the $\mathbf{e}_i$ in this direction, and $\bar{\boldsymbol{\sigma}}$ is the far-field stress tensor.

The initial orientations of the grains in each RVE were obtained from the experimental orientation distribution function provided by X-ray diffraction. The RVE with voxel tessellation was used to identify the parameters of the crystal plasticity model in section 5.1 to save the simulation time and cost. Afterwards, these parameters were used to simulate the cyclic stress-strain curves and fatigue deformation mechanisms using the Voronoi-type RVE with coarser mesh in section 5.2. The cyclic stress-strain curves of the RVE under uniaxial cyclic loading were simulated by Abaqus/Standard and the crystal plasticity constitutive model was coded in an User Material subroutine UMAT. The uniaxial cyclic deformation was achieved by applying an alternating cyclic displacement in one direction of the master node while keeping the total stresses in both perpendicular directions at zero. The applied strain rate was 10^{-3} s^{-1}.

5.1. Parameter Identification and Discretization Effects

The elastic constants of Mg single crystals used in the simulations, obtained from Zhang and Joshi [145], can be found in Table 5.1. The main parameters of the crystal plasticity model were adjusted by comparing experimental and simulated cyclic stress-strain curves. These parameters include the initial and saturated critical resolved shear stress of each slip system, as well as twinning, the corresponding isotropic hardening components, and the parameters for kinematic hardening for each slip system and twinning. They are depicted in Table 5.2. Other parameters were adopted from the literature for Mg alloys [202,203] and are listed in Table 5.3.

Table 5.1 – Elastic constants in GPa [145].

C_{11}	C_{12}	C_{33}	C_{13}	C_{44}
59.4	25.6	61.6	21.4	16.4

Table 5.2 – Model parameters determined by comparison of the simulation results with the experimental cyclic stress-strain curves at different strain semi-amplitudes and orientations.

Slip/Twin Mode	Basal	Prismatic	Pyramidal	Twinning
g^{ini} (MPa)	15.2	67.3	51.3	35.4
g^{sat} (MPa)	25	120	100	100
H (MPa)	10	50	1000	200
c (MPa)	-	-	5000	1300
d	-	-	70	70
k	-	-	7.5	7.5

Table 5.3 – Model parameters of the flow and hardening laws for Mg alloys [202,203].

$\dot{f}_0$	0.01
$\dot{\gamma}_0$	0.1
m	0.1
$h'_{\alpha\beta}$ (coplanar slip systems)	1
$h'_{\alpha\beta}$ (non-coplanar slip systems)	1
$h''_{\alpha\beta}$	2
$h'''_{\alpha\beta}$	1
a_{ss}	0.6
a_{tt}	1

The cyclic stress-strain curves corresponding to the deformation along RD, ND, and 45° RD-ND obtained from the simulation of the different RVEs at $\Delta\varepsilon/2 = 2\%$ (the highest strain semi-amplitude in each direction) are plotted in Figs. 5.2-5.4. The simulations were carried until a saturated cyclic stress-strain curve was achieved. Saturation was attained

after approximately 6 cycles in all orientations. The simulations capture the anisotropic (along RD and ND) and isotropic (along 45° RD-ND) cyclic stress-strain curves of the textured AZ31B Mg alloy with one set of crystal plasticity parameters. The simulation results with the Voronoi-type RVE with coarse mesh were very close to those obtained with the fine mesh and the voxel-type RVE. The simulations with the fine Voronoi-type RVE were very time consuming. Therefore, the coarse Voronoi-type RVE was used to assess the fatigue behavior of AZ31B in sections 5.2 and 5.3.

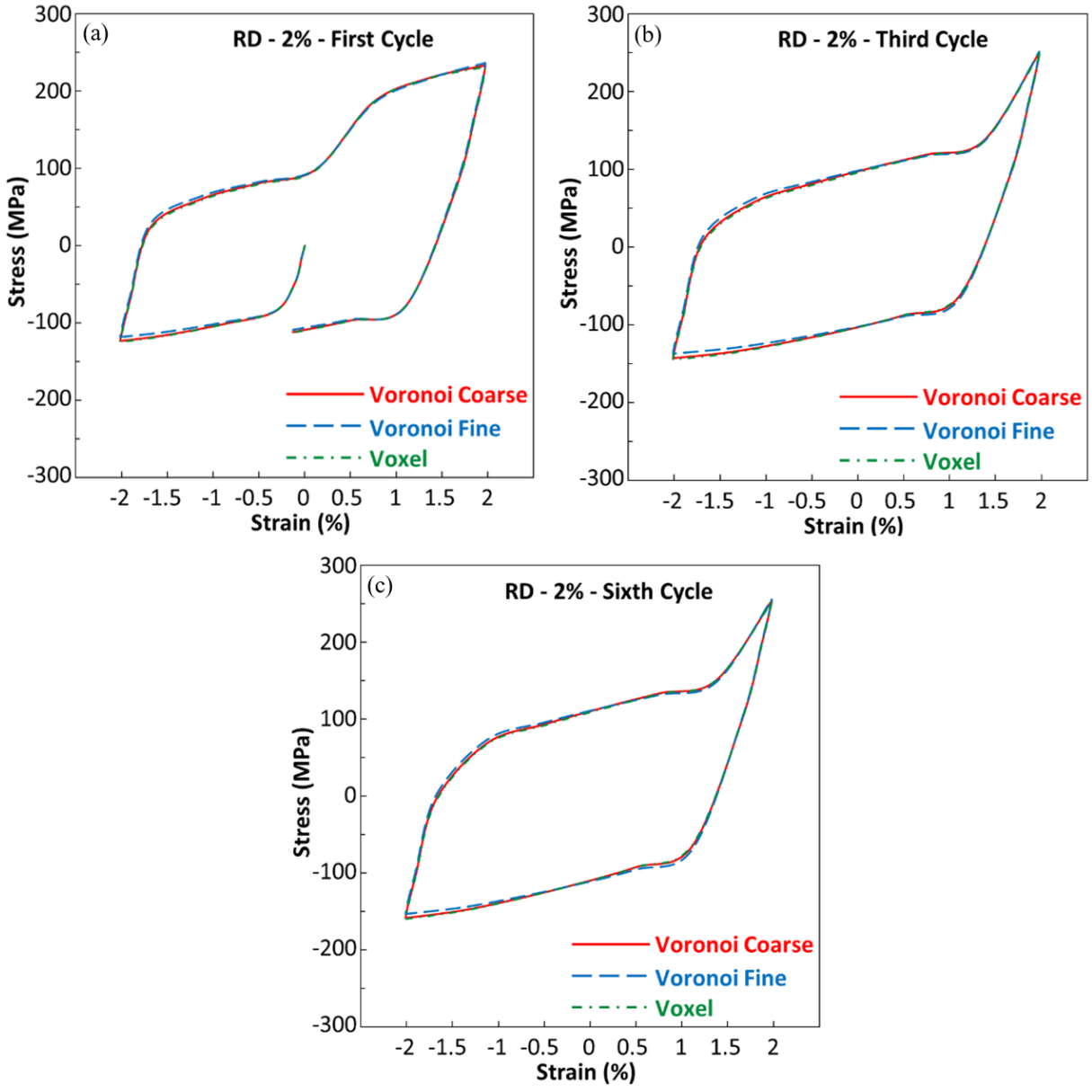

Figure 5.2 – Comparison of the simulated cyclic stress-strain curves of the AZ31 Mg alloy deformed along RD at $\Delta\varepsilon/2$ = 2% using different RVEs for the (a) First cycle (b)

Third cycle, and (c) Sixth cycle. The Voronoi tessellation with coarser mesh colored in red, the Voronoi tessellation with finer mesh colored in blue, and the Voxel tessellation colored in green in all figures. The simulated results overlap each other in all figures.

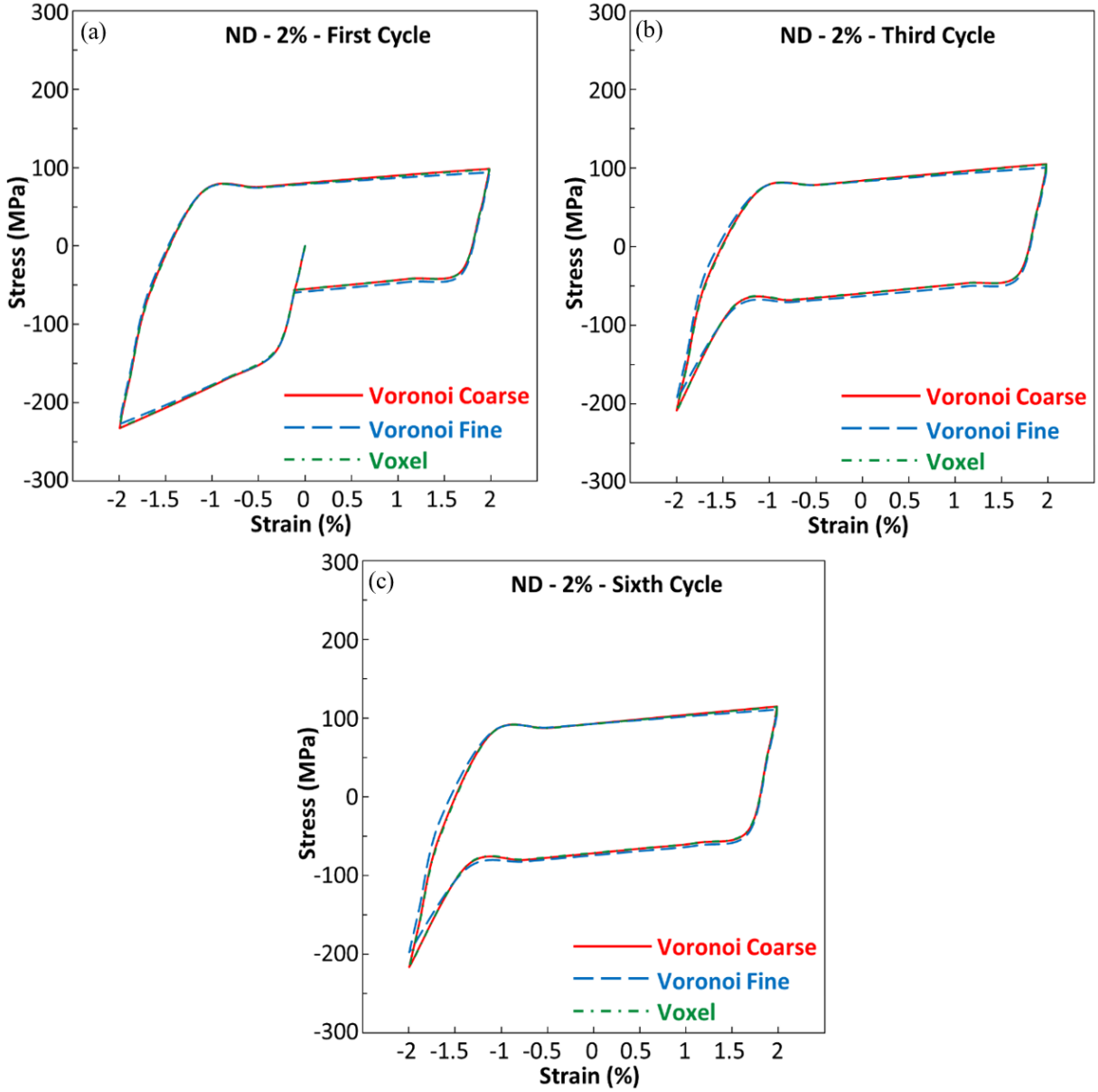

Figure 5.3 – Comparison of the simulated cyclic stress-strain curves of the AZ31 Mg alloy deformed along ND at $\Delta\varepsilon/2$ = 2% using different RVEs for the (a) First cycle (b) Third cycle, and (c) Sixth cycle. The Voronoi tessellation with coarser mesh colored in red, the Voronoi tessellation with finer mesh colored in blue, and the Voxel tessellation colored in green in all figures. The simulated results overlap each other in all figures.

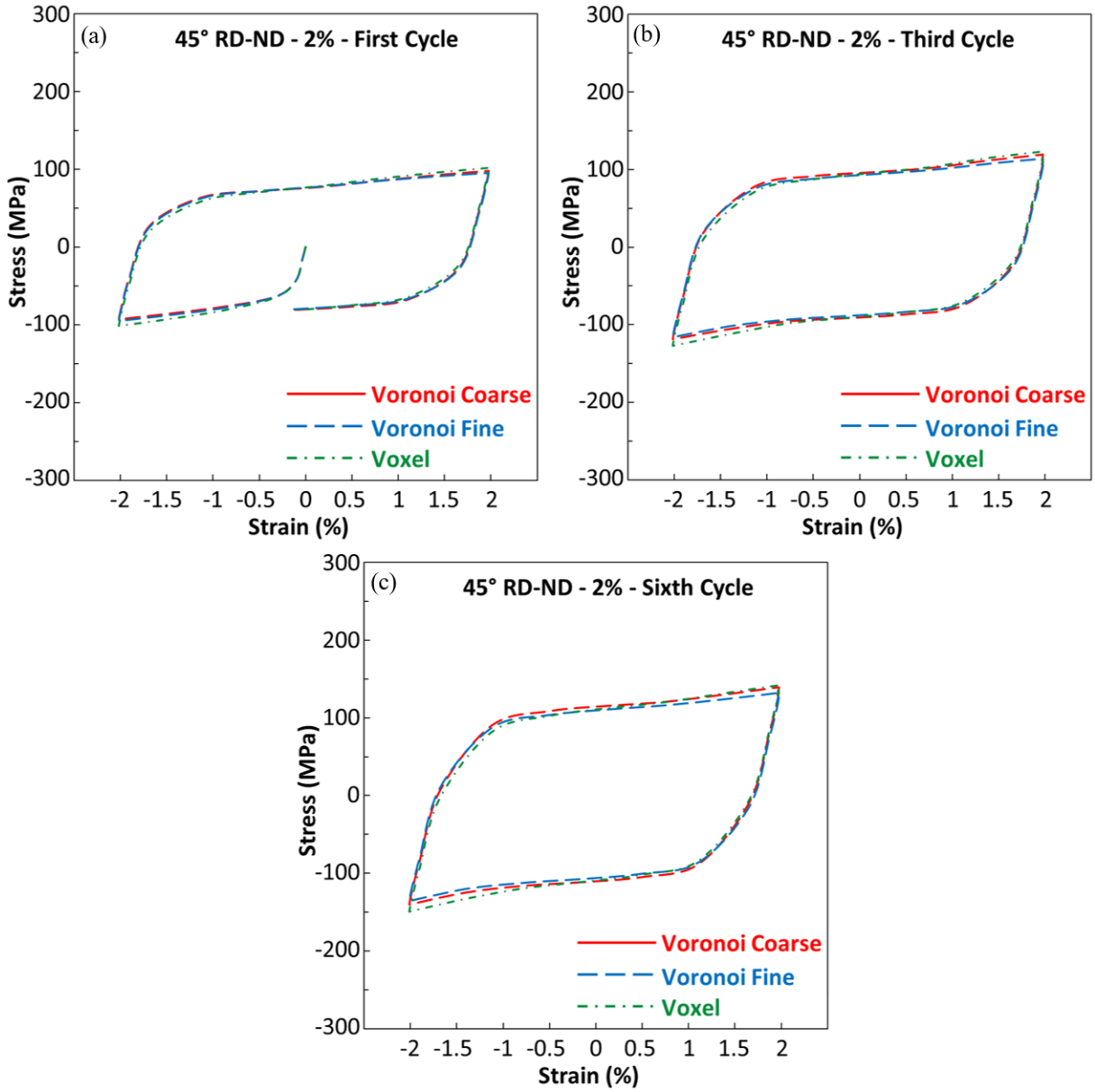

Figure 5.4 – Comparison of the simulated cyclic stress-strain curves of the AZ31 Mg alloy deformed along 45° RD-ND at $\Delta\varepsilon/2 = 2\%$ using different RVEs for the (a) First cycle (b) Third cycle, and (c) Sixth cycle. The Voronoi tessellation with coarser mesh colored in red, the Voronoi tessellation with finer mesh colored in blue, and the Voxel tessellation colored in green in all figures. The simulated results overlap each other in all figures.

5.2. Comparison of Experiments and Simulations

The rolled AZ31 Mg alloy presented a strong texture (Fig. 3.1b) in RD-TD plane. This texture was included in the orientation of the grains in the RVE and it is anticipated that the deformation mechanisms will be different in RD, ND, and 45° RD-ND. The cyclic stress-strain curves and the deformation mechanisms which attained from the simulation and experiments in the samples deformed along RD, ND, and 45° RD-ND at $\Delta\varepsilon/2$ = 0.4%, 0.8%, and 2% will be compared in sections 5.2.1-5.2.3. It should be noted that the simulation was carried out until a satrurated cyclic stress-strain curve was obtained, which occurred after about 6 cycles for all conditions.

5.2.1. Cyclic deformation mechanisms along the RD

The cyclic stress-strain curves for the samples deformed along RD obtained from simulations of a Voronoi-type RVE with a coarse mesh at $\Delta\varepsilon/2$ = 0.4%, 0.8%, and 2% are compared to experimental results in Fig. 5.5. The simulated curves agree well with the experimental results. The simulations reproduced the plastic anisotropy in the curves associated with the development of twinning/detwinning and pyramidal slip during cyclic loading along RD (Fig. 5.5). It should be noted that the experimental and simulated saturated maximum (tension) and minimum (compression) stresses were comparable for the samples deformed along RD with different cyclic strain amplitudes. In the RD samples, the simulated cyclic stress-strain curves stabilized rapidly (within a few cycles) in the tension part of the fatigue cycle, while the measured peak stress of hysteresis loop varied slightly during the fatigue deformation (as shown in Fig. 3.9). The compression part of the cyclic stress-strain curves did not saturate after a few cycles (particularly in the specimens deformed at $\Delta\varepsilon/2$ = 2% along RD) and this cyclic hardening in the compression part was also found in the experimental results (as shown in Fig. 3.9). As mentioned in section 3.2, cyclic hardening in compression is associated with the presence of twins that hinder the movement of pyramidal dislocations, that build up during the tensile part of the fatigue cycle.

Although the back stresses of different slip systems were considered in the current CPFEM model, the simulated stress-strain curves have different slopes from experimental ones during unloading. This reflects that the Bauschinger effect was not

properly captured by the simulations. The strong Bauschinger effect in Mg alloys [204–206] occurs due to the stress relaxation caused by detwinning. During this process, local stresses are redistributed among grains with different orientations, which retards the ongoing detwinning process. Furthermore, it has been reported that the accumulation of dislocations at higher strain amplitudes reduces the Bauschinger effect quickly [204]. However, these mechanisms are not considered in the constitutive model.

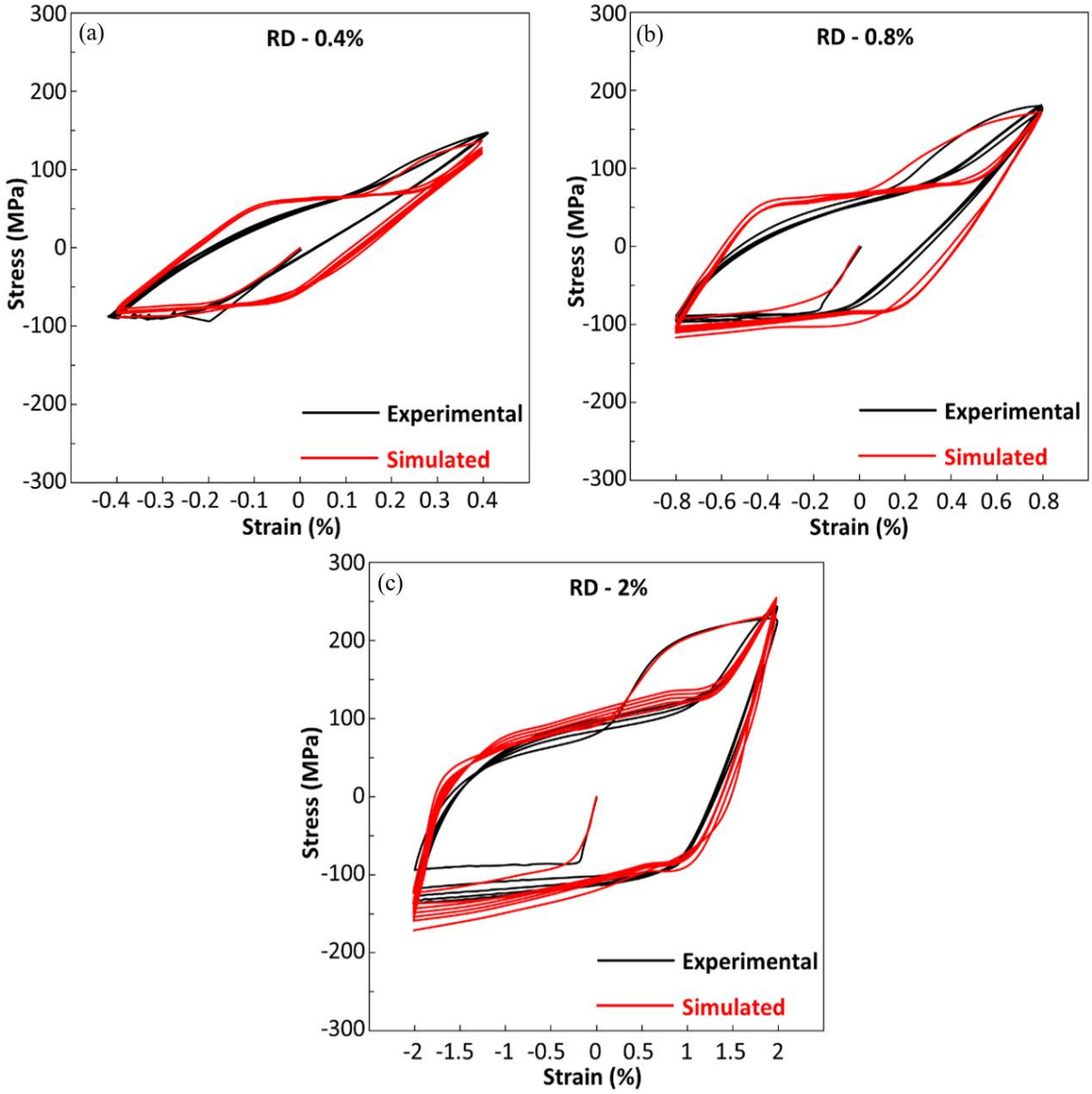

Figure 5.5 – Experimental (black) and simulated (red) cyclic stress-strain curves of the AZ31 Mg alloy deformed along RD at different strain semi-amplitudes ($\Delta\varepsilon/2$ = 0.4%,

0.8%, and 2%). The simulated curves are plotted using the RVE with Voronoi tessellation and a coarse mesh.

The average accumulated shear slip (average of all elements) for the different deformation mechanisms (basal slip, prismatic slip, pyramidal slip, and twinning) is plotted in Fig. 5.6 as a function of the number of cycles during the fatigue of AZ31 Mg alloy at different strain semi-amplitudes along RD. The average accumulated slip was calculated by averaging the results of all elements (27427 elements) in the RVE. According to Fig. 5.6, deformation was mainly accommodated by twinning/detwinning and pyramidal slip in the samples deformed along RD at $\Delta\varepsilon/2$ = 0.4%, 0.8%, and 2%. Some prismatic and basal slip was also observed, and their contribution to plastic deformation is reduced as strain semi-amplitude decreases (by comparing Figs. 5.6a-5.6c). These results are in a good agreement with experimental observations based on slip trace analysis, which are shown in Table 3.1.

5.2.2. Cyclic deformation mechanisms along the ND

The simulated cyclic stress-strain curves alongside with experimental ones for the samples deformed along ND at $\Delta\varepsilon/2$ = 0.4%, 0.8%, and 2% are plotted in Figure 5.7. The simulated stress-strain curves exhibit good agreement with the experimental ones, capturing the anisotropy of the curves resulting from twinning/detwinning and pyramidal slip during cyclic loading along ND (Fig. 5.7). Moreover, the saturated maximum (tension) and minimum (compression) stresses obtained from both experimental and simulated data were similar for samples deformed along ND at $\Delta\varepsilon/2$ = 0.8% and 2% (Fig. 5.7b and 5.7c). However, there is a gap of about 40 MPa between the simulated and measured saturated maximum stress (tension) for the sample deformed along ND at $\Delta\varepsilon/2$ = 0.4% although the saturated minimum stresses (compression) from simulations and experiments are comparable. It should be noted that the simulated stress-strain curves have different slopes from experimental ones during unloading due to the Bauschinger effect (which is explained in section 5.2.1).

The results of deformation mechanisms in the samples deformed along ND (Fig. 5.8) show similar trends to the RD samples. However, the contribution of prismatic slip in the fatigue of AZ31 Mg alloy along ND was almost zero due to the orientation of the grains (the prismatic planes are parallel to the loading direction in most grains).

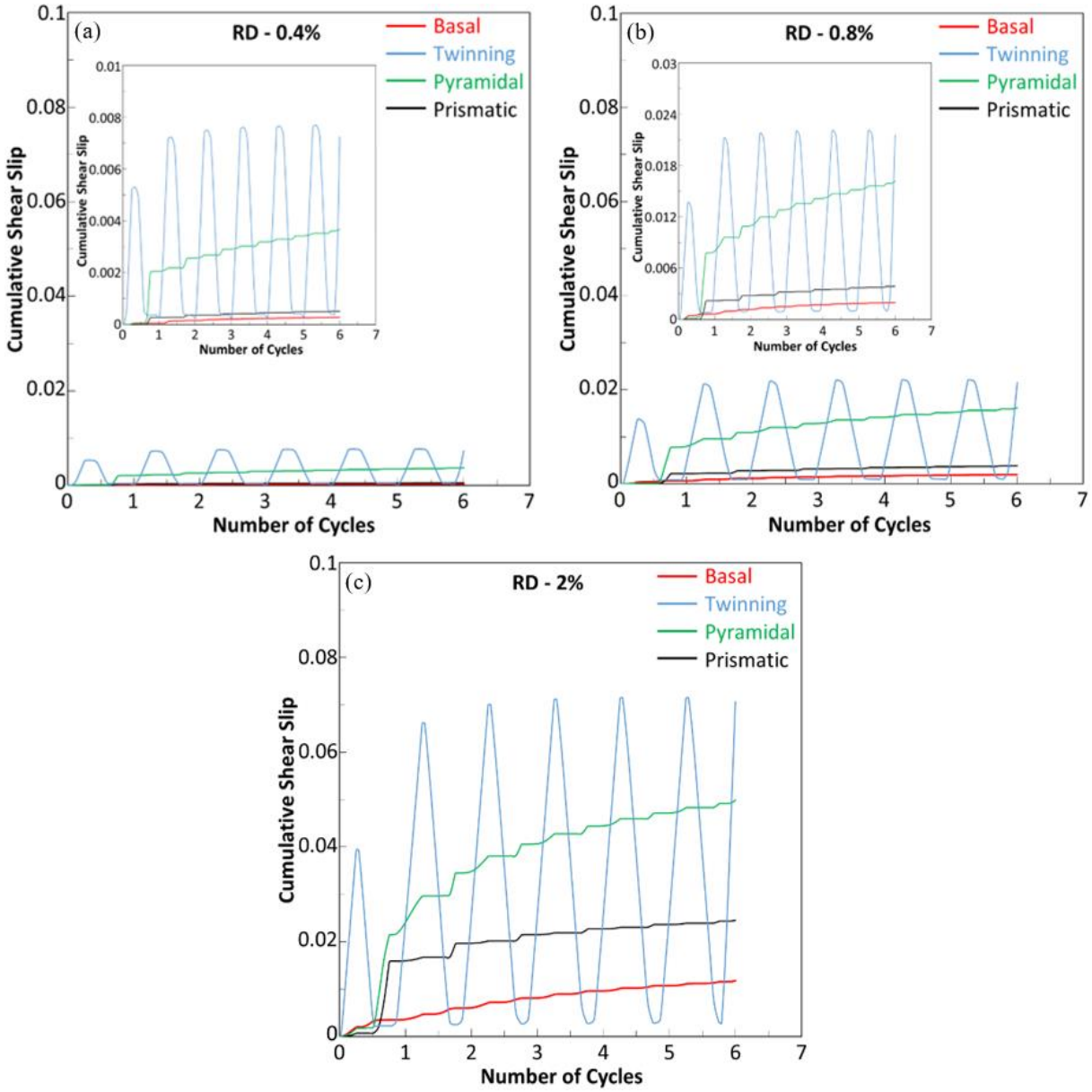

Figure 5.6 – Predictions of the accumulated plastic shear strains of different deformation mechanisms in the AZ31B Mg alloy subjected to the fatigue deformation along RD at (a) $\Delta\varepsilon/2$ = 0.4%, (b) $\Delta\varepsilon/2$ = 0.8%, and (c) $\Delta\varepsilon/2$ = 2%. The accumulated shear slip by basal slip, pyramidal slip, prismatic slip, and twinning are shown with red, green, black, and blue lines, respectively.

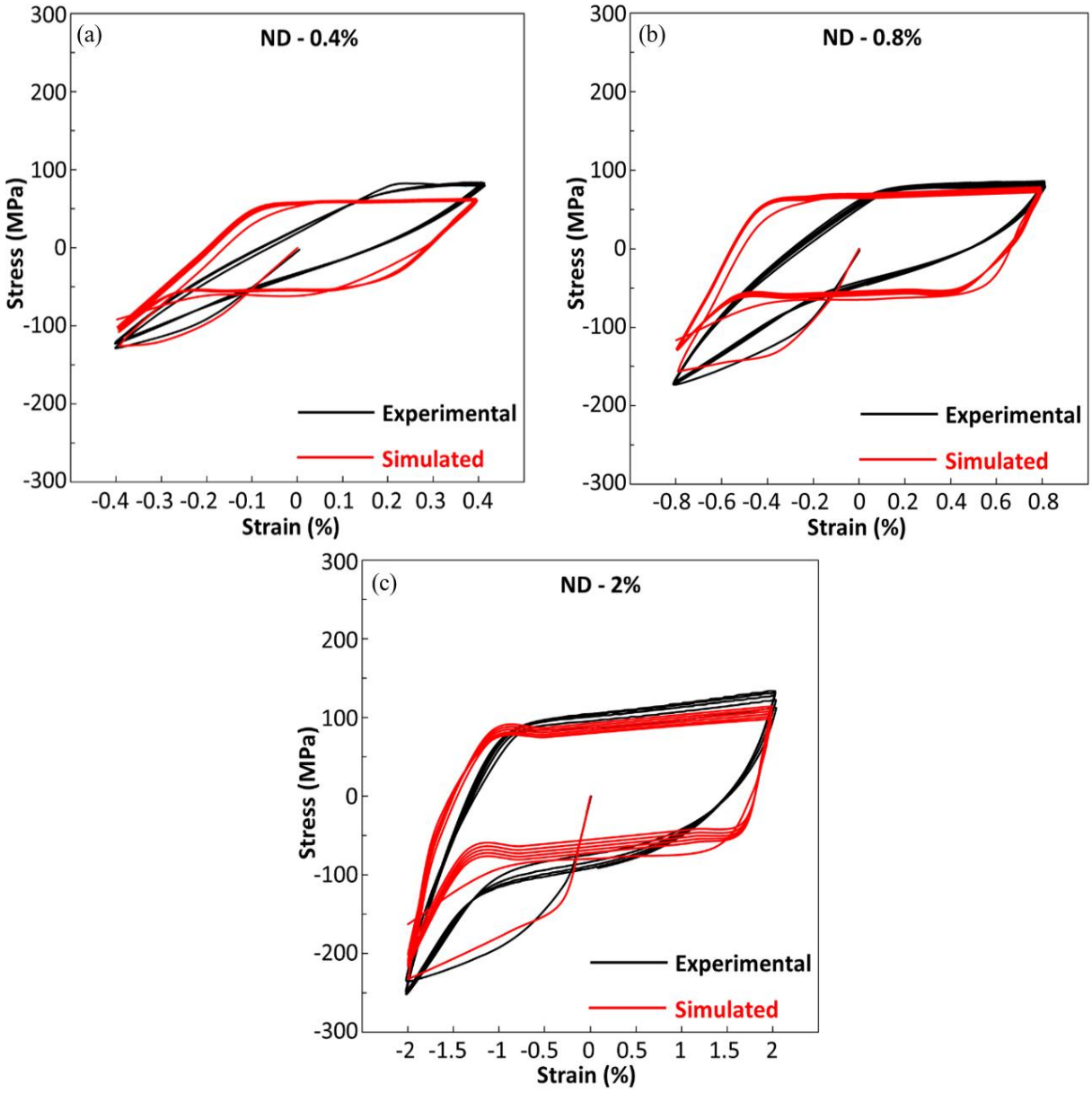

Figure 5.7 – Experimental (black) and simulated (red) cyclic stress-strain curves of the AZ31 Mg alloy deformed along ND at different strain semi-amplitudes ($\Delta\varepsilon/2$ = 0.4%, 0.8%, and 2%). The simulated curves are plotted using the RVE with Voronoi tessellation and a coarse mesh.

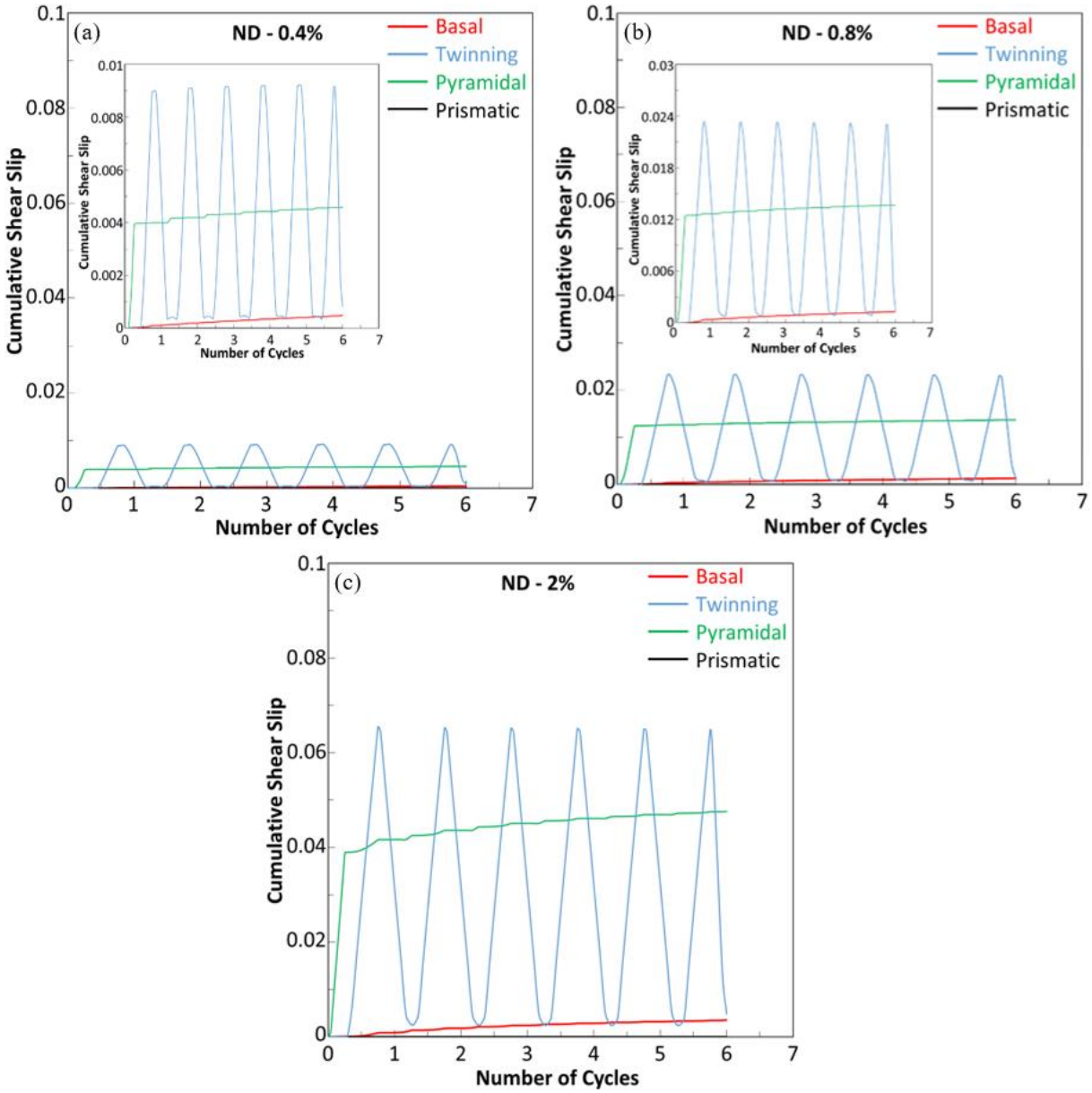

Figure 5.8 – Predictions of the accumulated plastic shear strains of different deformation mechanisms in the AZ31B Mg alloy subjected to the fatigue deformation along ND at (a) $\Delta\varepsilon/2 = 0.4\%$, (b) $\Delta\varepsilon/2 = 0.8\%$, and (c) $\Delta\varepsilon/2 = 2\%$. The accumulated shear slip by basal slip, pyramidal slip, prismatic slip, and twinning are shown with red, green, black, and blue lines, respectively, in all figures.

5.2.3. Cyclic deformation mechanisms along 45° RD-ND

The simulated cyclic stress-strain curves for the samples deformed along 45° RD-ND at $\Delta\varepsilon/2$ = 0.4%, 0.8%, and 2% are plotted together with experimental ones in Fig. 5.9. The simulated stress-strain curves that were in good agreement with the experimental data, effectively capturing the isotropic cyclic stress-strain curves caused by basal slip when the samples deformed along 45° RD-ND (as shown in Figure 5.9). Furthermore, the saturated maximum (tension) and minimum (compression) stresses from both simulations and experiments were comparable for samples that were deformed along 45° RD-ND at $\Delta\varepsilon/2$ = 0.8% and 2% (as depicted in Figs. 5.9b and 5.9c). Nevertheless, there is a difference of approximately 40 MPa between the simulated and measured maximum saturated stress (tension) for the sample deformed along 45° RD-ND at $\Delta\varepsilon/2$ = 0.4% although the saturated minimum stress (compression) obtained from both simulation and experiments are comparable.

It is worth mentioning that the simulated stress-strain curves exhibit different slopes from the experimental curves during unloading, which is attributable to the Bauschinger effect (as detailed in section 5.2.1). However, this difference in the samples deformed along 45° RD-ND is lower than the ones for the samples deformed along RD and ND because the contribution of twinning/detwinning is much lower in 45° RD-ND.

In contrast with RD and ND samples, most of the grains are suitably oriented for basal slip in 45° RD-ND due to the texture (Fig. 3.1a): Therefore, the deformation in 45° RD-ND was mainly accommodated by basal slip. Figure 5.10 illustrates the accumulation of slip with respect to the number of cycles for different deformation mechanisms (prismatic slip, basal slip, pyramidal slip, and twinning) during the fatigue of AZ31 Mg alloy at different strain semi-amplitudes along 45° RD-ND. As depicted in Figure 5.10, the main deformation mechanism in the samples that were deformed along 45° RD-ND at $\Delta\varepsilon/2$ = 0.4%, 0.8%, and 2% was basal slip, and the cumulative shear strain accumulated in other slip systems is negligible (Fig. 5.10). It should be noted that the twinning was also observed in our experimental results (which were shown in section 3.4), however, the amount of accumulated shear strain in twins were small at different strain semi-amplitudes (which were calculated from simulations). This can be traced to the activation

of basal slip in a large number of grains in this orientation due to the texture (the twinning was activated in a limited number of grains), which produce a large amount of accumulated shear strain in basal slip.

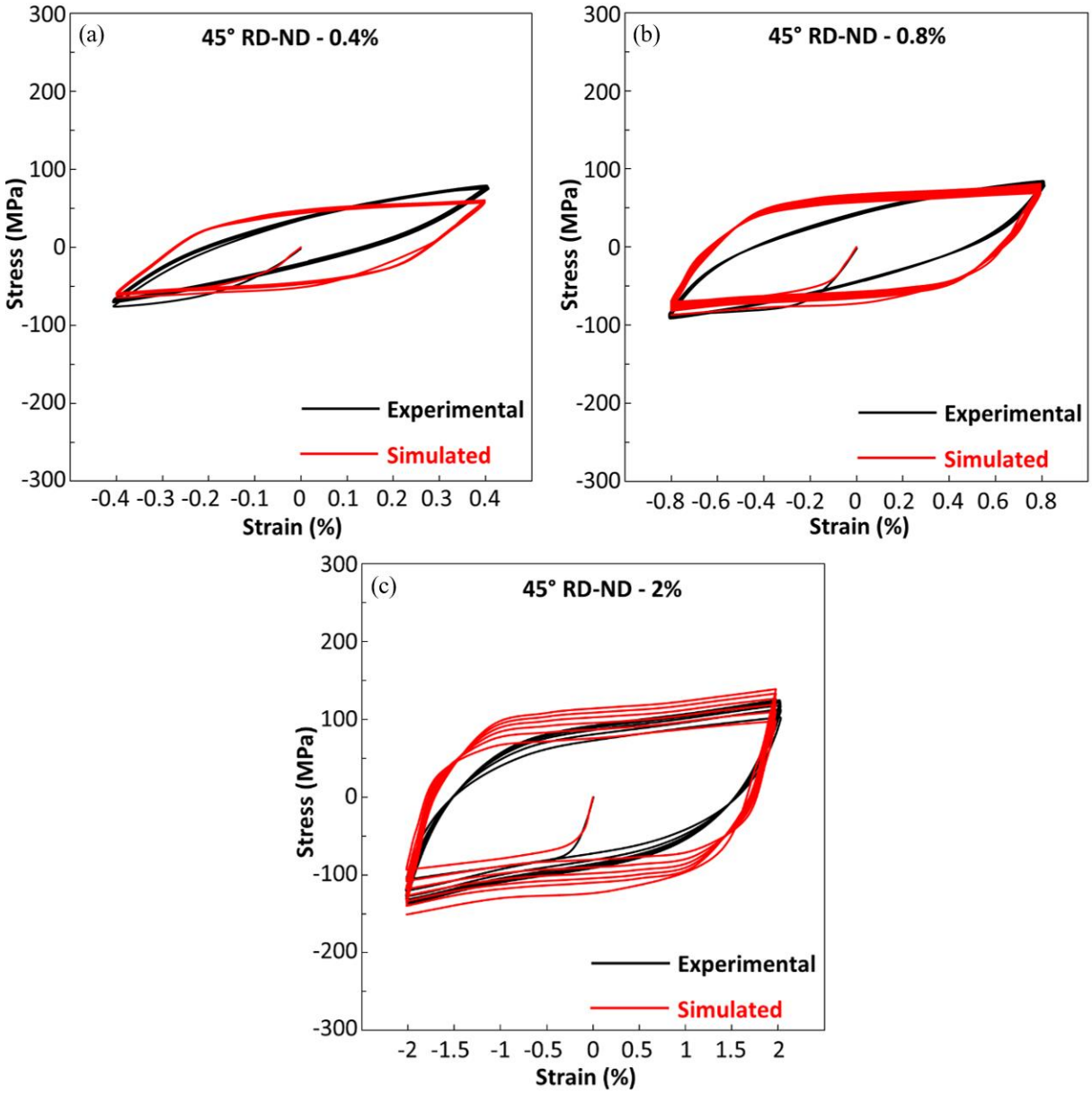

Figure 5.9 – Experimental (black) and simulated (red) cyclic stress-strain curves of the AZ31 Mg alloy deformed along 45° RD-ND at different strain semi-amplitudes ($\Delta\varepsilon/2$ = 0.4%, 0.8%, and 2%). The simulated curves are plotted using the RVE with Voronoi tessellation and a coarse mesh.

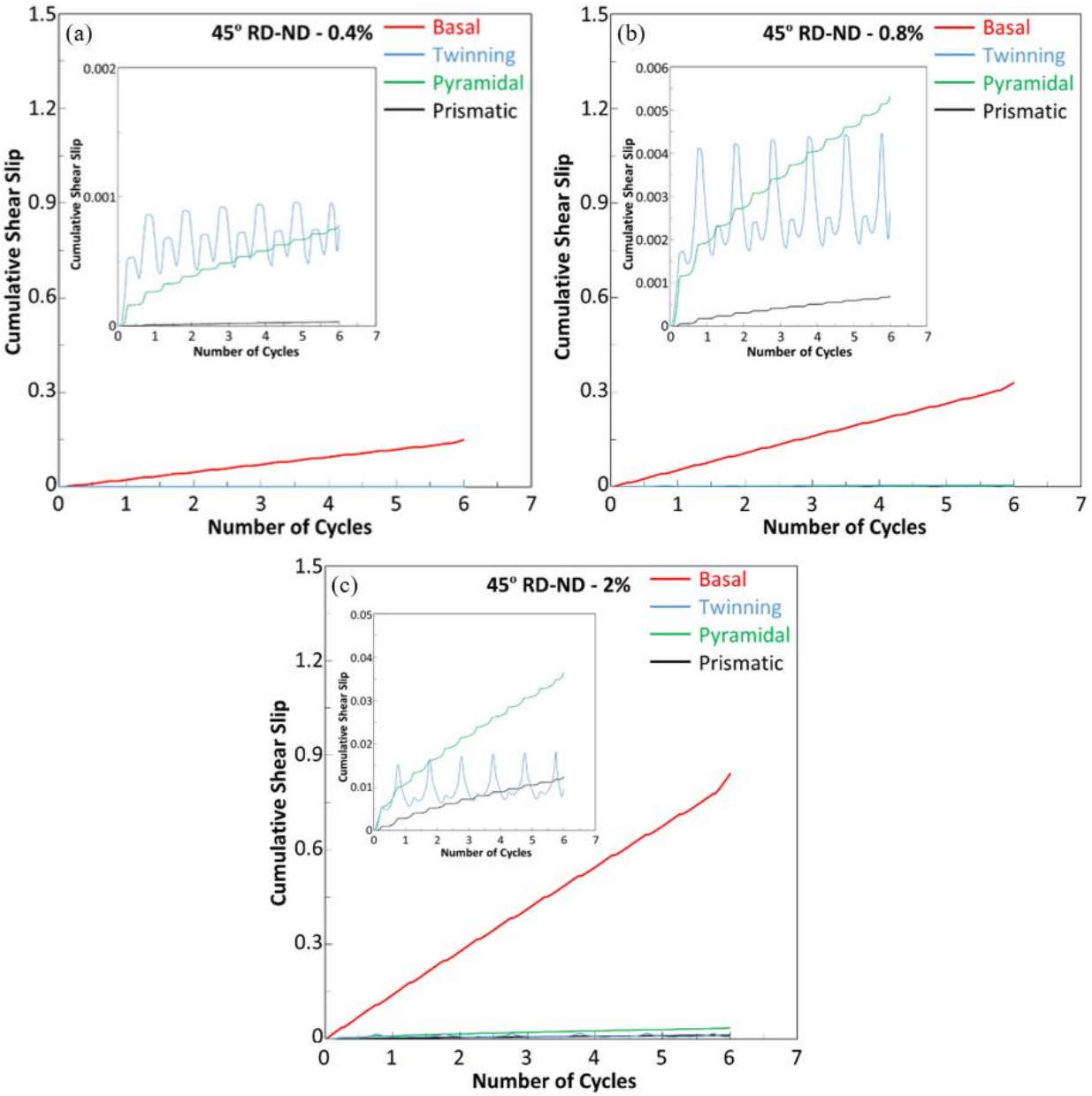

Figure 5.10 – Predictions of the accumulated plastic shear strains of different deformation mechanisms in the AZ31B Mg alloy subjected to the fatigue deformation along 45° RD-ND at (a) $\Delta\varepsilon/2 = 0.4\%$, (b) $\Delta\varepsilon/2 = 0.8\%$, and (c) $\Delta\varepsilon/2 = 2\%$. The accumulated shear slip by basal slip, pyramidal slip, prismatic slip, and twinning are shown with red, green, black, and blue lines, respectively, in all figures.

5.3. Prediction of Fatigue Life

The current approaches to predicting the fatigue life of polycrystalline materials involves the use of Fatigue Indicator Parameters (FIPs), according to Shenoy et al. [184]. These FIPs relate to the primary driving force that governs the formation of cracks, and

they can be determined from the local evolution of mechanical fields and internal variables within the RVE during each fatigue cycle [91]. The most common FIPs are based only on local plastic strain fields, such as the plastic shear strain that accumulates in a single fatigue cycle [169,170]. It should be noted that most of the fatigue life during low-cycle fatigue is dominated by the growth of small in cracks. However, most models that employ computational homogenization to predict fatigue life assume that FIPs obtained from RVEs without cracks can be used to make predictions [91,184]. This assumption is supported by the observation that many FIPs, including the accumulated plastic strain and the energy dissipated in each fatigue cycle, serve as reliable indicators of the driving force behind both fatigue crack initiation and fatigue crack propagation in small cracks.

As the plastic shear strain varies throughout the microstructure of the RVE, we assumed the deformation mechanism producing maximum amount of shear initiates a fatigue crack in Mg alloys which will propagate until failure occurs. Consequently, the definition of FIPs according to the average values for the plastic shear strain of a deformation mechanism cannot be used to prediction of fatigue life of Mg alloys using equation 1.13. At the same time, the maximum value of accumulated shear strain of one slip system was affected by the finite element discretization details. Castelluccio and McDowell [207] proposed various approaches to avoid fake stress concentrations and reduced mesh size effects. One option is to calculate the FIP by volume averaging within a region indicative of the crack incubation zone [184,207,208]. The dependence of FIP on mesh size can be avoided to some extent by considering the statistical distribution of accumulated shear amount inside the RVE.

As there are 27427 elements in the coarse Voronoi-type RVE, it is possible to calculate the cumulative probability of $\Delta\gamma_s^\alpha$ for any deformation mechanism during one saturated stress-strain hysteresis loop. The cumulative probabilities $\Delta\gamma_s^\alpha$ for $\Delta\varepsilon/2$ = 0.4%, 0.8%, and 2% along RD, ND, and 45° RD-ND are plotted in Figs. 5.11-5.13 for basal and pyramidal slip. The concept can be understood as follows: for instance, when the accumulated plastic shear strain corresponds to a cumulative probability of 1/27427, this represents the highest shear amount because only one element within the RVE has reached thisvalue. As the amount of accumulated shear increases, the likelihood of finding elements with this specific shear strain inside the RVE decreases.

After balancing the accumulated shear amount and its probability, the $\Delta\gamma_s^{\alpha}$ corresponds to a cumulative probability of 1000/27427 was chosen to define the FIP which will be used to predict the fatigue life in AZ31 Mg alloy for different loading cases. The values of accumulated plastic shear strain of basal and pyramidal slip systems for the samples deformed along RD, ND, and 45° RD-ND at $\Delta\varepsilon/2$ = 0.4%, 0.8%, and 2% are shown in Table 5.4 which are extracted from Figs. 5.11-5.13.

Calculating the cumulative probability of accumulated plastic shear strain in twins is difficult due to the occurrence of detwinning and twinning in one fatigue cycle. Therefore, the difference between the maximum and minimum shear strain produced by twinning in Figs. 5.6, 5.8, and 5.10 is considered as the accumulated plastic shear of twins, i.e., $\Delta\gamma^{Tw}$. For the samples deformed along RD, ND, and 45° RD-ND at $\Delta\varepsilon/2$ = 0.4%, 0.8%, and 2%, calculated $\Delta\gamma^{Tw}$ are listed in Table 5.5.

The accumulated plastic shear strains of different deformation mechanisms during one fatigue cycle were used to predict the fatigue life of AZ31 Mg alloy according to Equation 1.13.

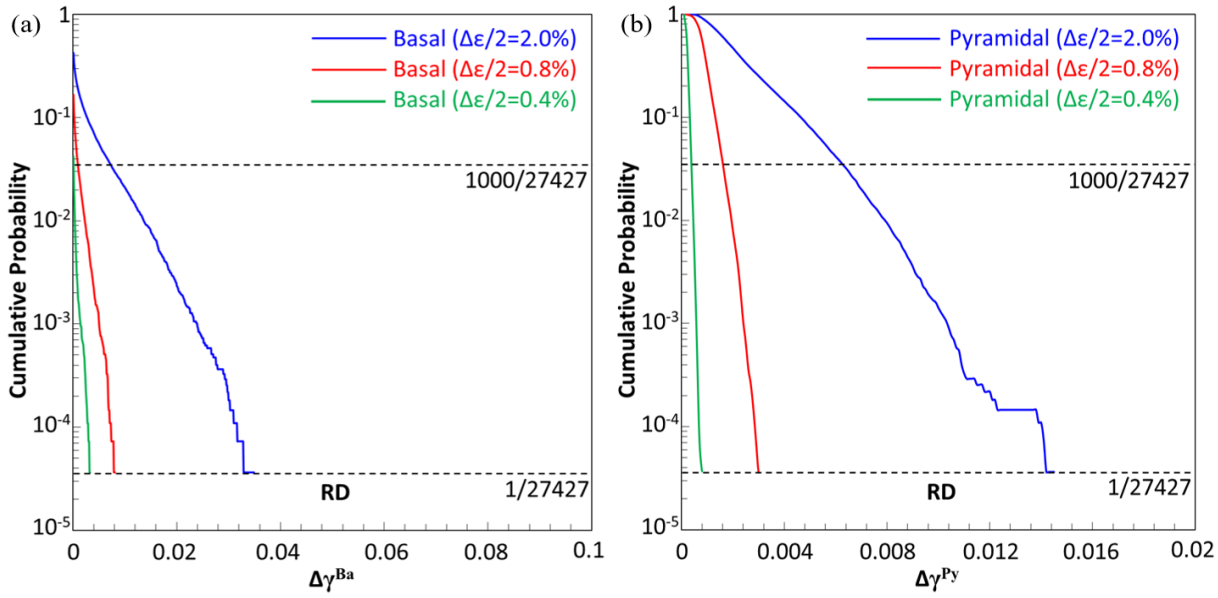

Figure 5.11 – Cumulative probability of accumulated plastic shear strain of (a) basal slip ($\Delta\gamma^{Ba}$) and (b) pyramidal slip ($\Delta\gamma^{Py}$), in the RVE of the AZ31 Mg alloy subjected to fatigue deformation along RD at different cyclic strain semi-amplitudes. Green, red, and blue lines represent $\Delta\varepsilon/2$ = 0.4%, 0.8%, and 2%, respectively.

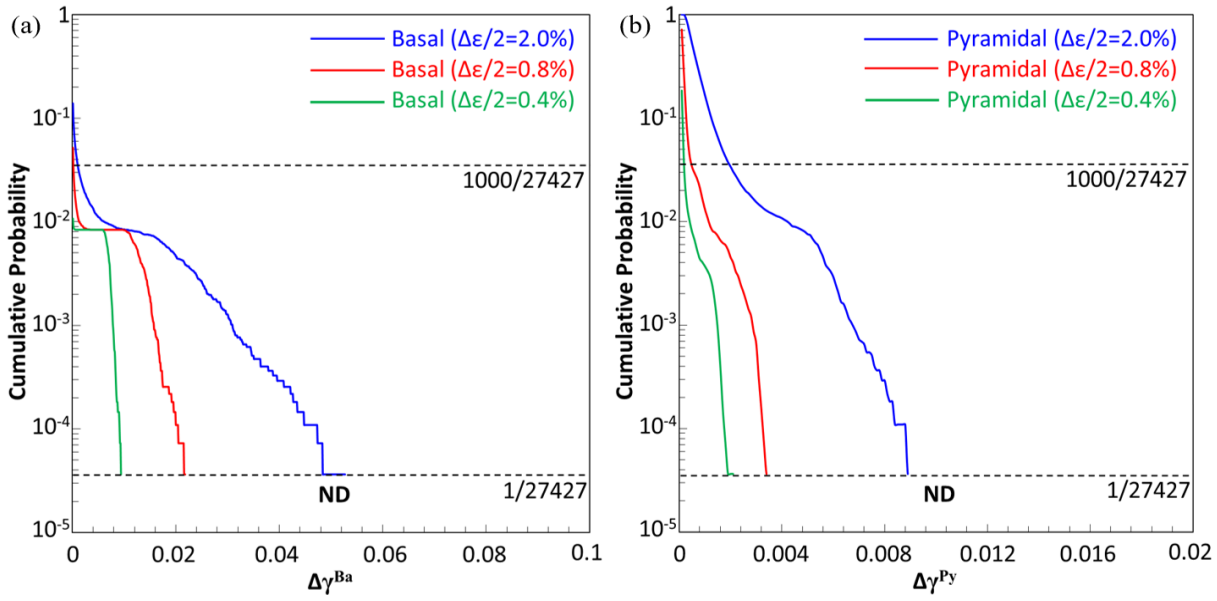

Figure 5.12 – Cumulative probability of accumulated plastic shear strain of (a) basal slip ($\Delta\gamma^{Ba}$) and (b) pyramidal slip ($\Delta\gamma^{Py}$), in the RVE of the AZ31 Mg alloy subjected to fatigue deformation along ND at different cyclic strain semi-amplitudes. Green, red, and blue lines represent $\Delta\varepsilon/2$ = 0.4%, 0.8%, and 2%, respectively.

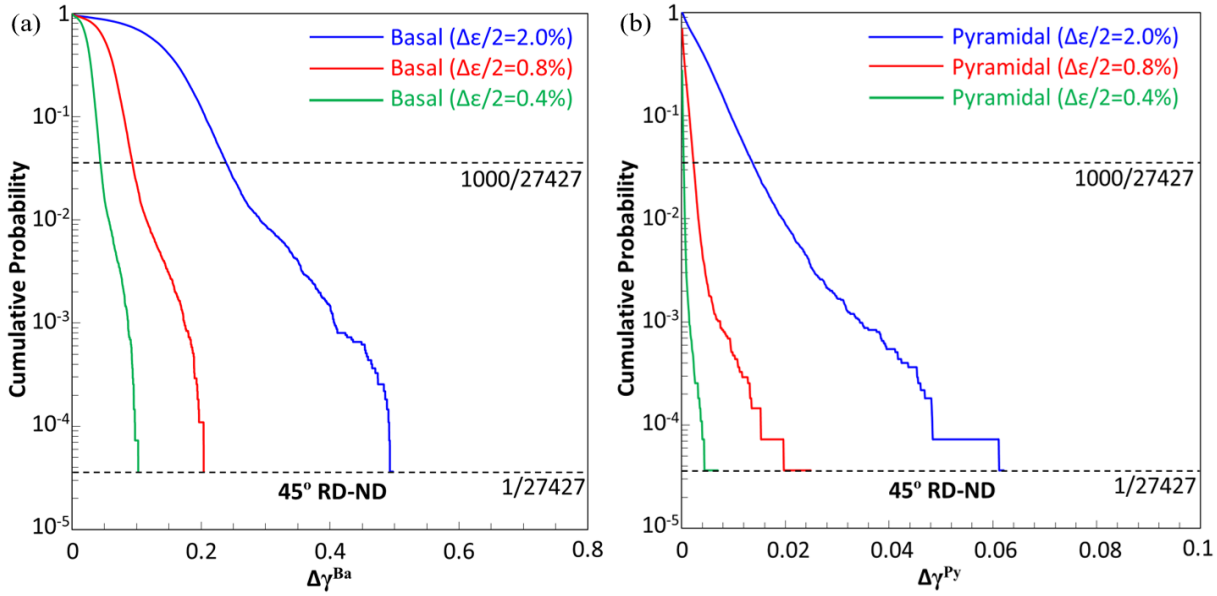

Figure 5.13 – Cumulative probability of accumulated plastic shear strain of (a) basal slip ($\Delta\gamma^{Ba}$) and (b) pyramidal slip ($\Delta\gamma^{Py}$), in the RVE of the AZ31 Mg alloy subjected to fatigue deformation along 45° RD-ND at different strain semi-amplitudes. Green, red, and blue lines represent $\Delta\varepsilon/2$ = 0.4%, 0.8%, and 2%, respectively.

Table 5.4 – Plastic shear strain accumulated in basal ($\Delta\gamma^{Ba}$) and pyramidal slip ($\Delta\gamma^{Py}$) in one fatigue cycle corresponds to a cumulative probability of 1000/27427.

	$\Delta\varepsilon/2 = 0.4\%$	$\Delta\varepsilon/2 = 0.8\%$	$\Delta\varepsilon/2 = 2.0\ \%$
RD	$\Delta\gamma^{Ba} = 0.0002$ $\Delta\gamma^{\mathrm{Py}} = 0.0004$	$\Delta\gamma^{Ba} = 0.001$ $\Delta\gamma^{Py} = 0.0016$	$\Delta\gamma^{Ba} = 0.0074$ $\Delta\gamma^{Py} = 0.0063$
ND	$\Delta\gamma^{Ba} = 0.0001$ $\Delta\gamma^{Py} = 0.0002$	$\Delta\gamma^{Ba} = 0.0002$ $\Delta\gamma^{Py} = 0.0005$	$\Delta\gamma^{Ba} = 0.0009$ $\Delta\gamma^{Py} = 0.002$
45º RD-ND	$\Delta\gamma^{Ba} = 0.0447$ $\Delta\gamma^{Py} = 0.0004$	$\Delta\gamma^{Ba} = 0.0938$ $\Delta\gamma^{Py} = 0.0023$	$\Delta\gamma^{Ba} = 0.241$ $\Delta\gamma^{Py} = 0.0138$

Table 5.5 – Accumulated plastic shear strain of twins ($\Delta\gamma^{Tw}$) in one fatigue cycle corresponding to the average of all elements.

	$\Delta\varepsilon/2 = 0.4\%$	$\Delta\varepsilon/2 = 0.8\%$	$\Delta\varepsilon/2 = 2.0\ \%$
RD	$\Delta\gamma^{Tw} = 0.007$	$\Delta\gamma^{Tw} = 0.0218$	$\Delta\gamma^{Tw} = 0.069$
ND	$\Delta\gamma^{Tw} = 0.0077$	$\Delta\gamma^{Tw} = 0.0225$	$\Delta\gamma^{Tw} = 0.0628$
45º RD-ND	$\Delta\gamma^{Tw} = 0.0004$	$\Delta\gamma^{Tw} = 0.0024$	$\Delta\gamma^{Tw} = 0.01$

It was shown in the experiments that the fatigue deformation of AZ31B sample was mainly accommodated by the pyramidal slip for the loading case of (RD, Δε/2=2%). However, basal slip and twinning were the main deformation mechanisms for loading case of (45º-RD-ND, Δε/2=0.4%).

In this work, the critical accumulated plastic shear strain $\Delta\gamma^{C}$ was treated as a material parameter. $\Delta\gamma^{C}$ of pyramidal slip was calculated from the loading case of (RD, Δε/2=2%), while $\Delta\gamma^{C}$ of basal slip and twinning were calculated from the loading case of (45º-RD-ND, Δε/2=0.4%) according to

$$\Delta\gamma^{c} = N.\Delta\gamma_{s}^{\alpha} \tag{5.1}$$

where N is the average fatigue life from experiments and $\Delta\gamma_s^\alpha$ is the plastic shear strain accumulated in the slip system α (which are shown for different conditions in Table 5.4 and 5.5). As a result, the calculated values of $\Delta\gamma^C$ for different deformation mechanisms are shown in Table 5.6.

Table 5.6 – Critical accumulated plastic shear strain of different deformartion mechanisms.

Deformation Mechanism	$\Delta\gamma^C$
Pyramidal Slip	0.9419
Basal Slip	278.1
Twinning	2.613

The experimental fatigue life shown in Fig. 3.10 can be fitted to Equation 1.13 using one set of $\Delta\gamma^C$ which are shown in Table 5.6. The prediction capabilities of different FIPs (plastic shear strain accumulated for basal slip FIP^{Ba}, pyramidal slip FIP^{Py}, and twinning FIP^{Tw}) for the samples deformed along RD, ND, and 45°-RD-ND at $\Delta\varepsilon/2$=0.4%, 0.8%, and 2% are compared in Fig. 5.14.

As shown in Figs. 5.14a and 5.14b, the FIP^{Py} and FIP^{Tw} give reasonable predictions of the fatigue life in RD and ND loading cases. None of them can be nominated as the best due to the limited number of experimental tests.

Moreover, the predicted fatigue lives by FIP^{Ba} along RD and ND are far from the experimental results. We found that the fatigue life of AZ31B along RD and ND directions can be predicted by FIP^{Py} and FIP^{Tw}. Furthermore, one should give FIP^{Tw} a higher weighting factor because the predcited fatigue lives according to FIP^{Tw} are lower than the other precited by other FIPs (Figs. 5.14a and 5.14b).

In addition, the predicted fatigue lives by FIP^{Tw} in the samples deformed along 45° RD-ND direction are in good agreement with the experimental results. The predicted fatigue lives by FIP^{Ba} were also reasonable (Fig. 5.14c). It should be noted that the FIP^{Py} was not considered for the samples deformed along 45° RD-ND because the contribution

of pyramidal slip was negligible in comparison with basal slip in this direction (Fig. 5.10). It can be concluded that the fatigue life of AZ31B along 45° RD-ND direction is controlled by twinning in each fatigue cycle.

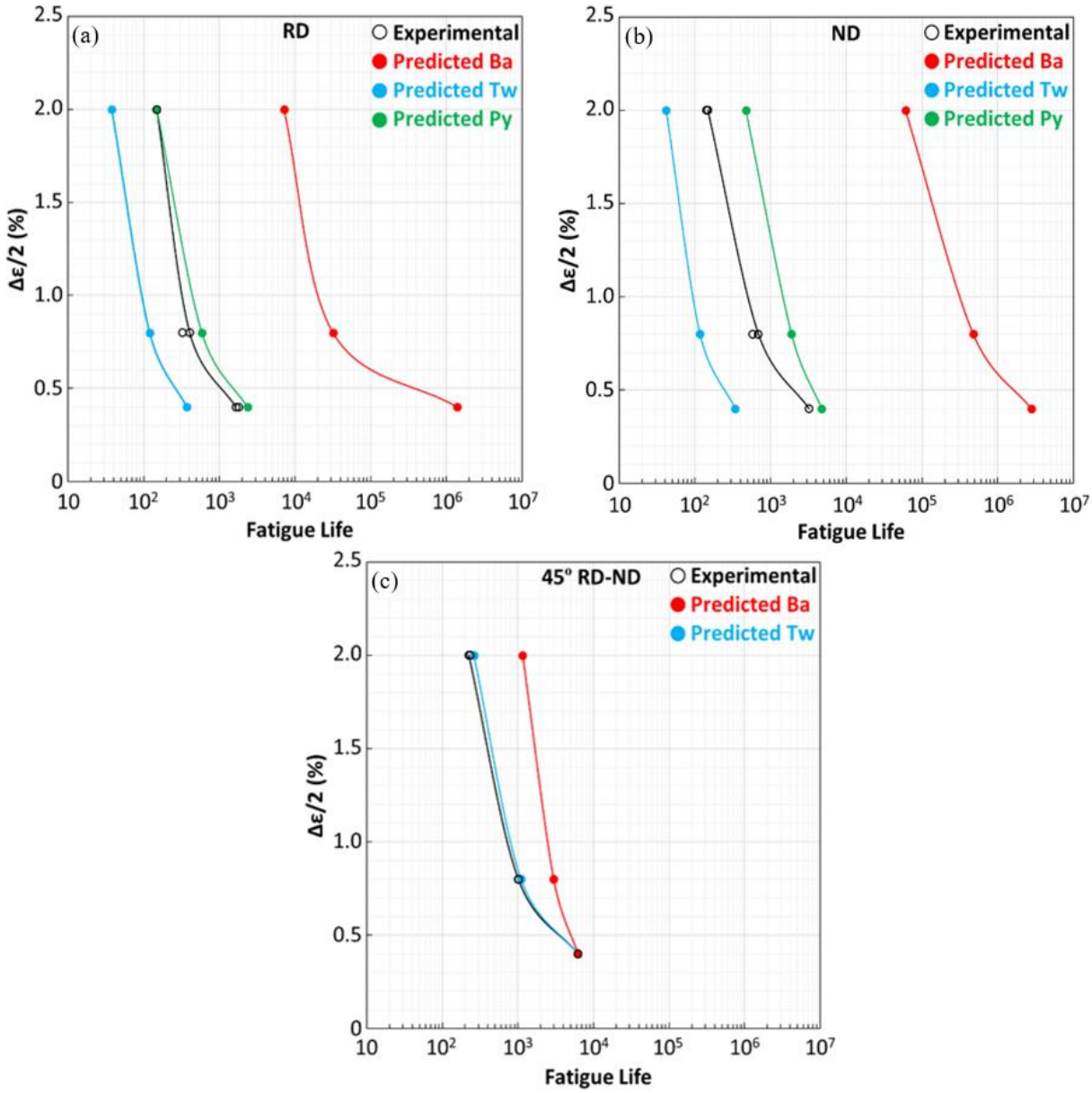

Figure 5.14 – Comparison between measured and predicted fatigue life in (a) RD, (b) ND, and (c) 45° RD-ND. The experimental results are marked with black color. The predicted fatigue life was from calculated from the FIPs associated with the accumulated plastic shear strain of basal slip, pyramidal slip, and twinning (colored with red, green, and blue lines, respectively).

6. CONCLUSIONS

The fatigue crack initiation mechanisms of textured AZ31B-O alloy under fully reversed strain-controlled fatigue strongly depend on the loading direction and strain semi-amplitude due to the activation of different deformation mechanisms.

- In the samples deformed along RD at $\Delta\varepsilon/2 = 2\%$, the dominant cracking mechanisms are grain boundary cracking at grain boundaries with large misorientation angles in small grains, and transgranular cracking (parallel to the pyramidal slip or twin) in large grains.
- Large cracks were found to have nucleated along twins in the sample deformed along RD at a strain amplitude of 0.4% in large grains. Furthermore, clusters of small grains that were suitably oriented for basal slip showed deformation localization, leading to the nucleation of large fatigue cracks in this sample. Although grain boundary cracks were also present in this sample, particularly around small grains, they were shorter and less critical from the viewpoint of fatigue failure.
- Specimens oriented at 45° RD-ND were suitably oriented for basal slip and twining/detwinning, which were the dominant deformation mechanisms. They are representative of Mg alloys with low texture. The most damaging fatigue cracks were initiated parallel to twins in large grains at $\Delta\varepsilon/2 = 0.4\%$ and 2%. Grain boundary cracks, particularly around small grains, were also found, and the intergranular fracture probability increased with the cyclic strain semi-amplitude, but these cracks are shorter and less critical from the viewpoint of fatigue failure.

The fatigue life of the textured AZ31 Mg alloy can be predicted along RD, ND, and 45° RD-ND from a fatigue indicator parameter based on the accumulated shear strain by slip/twinning in each fatigue cycle.

- The fatigue life of AZ31 Mg alloy along RD and ND can be predicted from the fatigue indicator parameters corresponding to pyramidal slip and twinning, but the last one predicts shorted fatigue life.

- The fatigue life of AZ31 Mg alloy along 45° RD-ND can be predicted from the fatigue indicator parameters corresponding to basal slip and twinning. Nevertheless, the fatigue indicator parameters corresponding to twinning predict shorter fatigue lives and are in better agreement with the experimental data.
- Thus, the results of simulations and experiments conclude that fatigue life of textured AZ31B Mg alloy is mainly controlled by the nucleation of fatigue cracks from extension twin boundaries.

7. FUTURE WORK

The following areas of future work are envisioned:

- This work showed that the fatigue crack initiation mechanisms in Mg alloys depend on the deformation mechanisms. The high-temperature fatigue behavior of Mg alloys should be investigated to see the effect of activating grain boundary sliding and more pyramidal slips on the fatigue crack initiation mechanisms.
- The predicted cyclic stress-strain curves in this study were not perfect, which can be attributed to the Bauschinger effect which cannot be fully captured by the back stress model used. To demonstrate the difference from the results of this study, a new crystal plasticity model with better back stress model should be developed.
- The predicted fatigue lives in this study were not perfect due to the limited number of experiments. More fatigue tests should be done along RD, ND, and 45° RD-ND at different strain semi-amplitudes (other than the ones were done in this study), and predict fatigue lives in Mg alloys in different orientations using machine learning models (machine learning models can be applied due to the large data set).

8. BIBLIOGRAPHY

[1] N.P. Gillett, V.K. Arora, K. Zickfeld, S.J. Marshall, W.J. Merryfield, Ongoing climate change following a complete cessation of carbon dioxide emissions, Nat. Geosci. 4 (2011) 83–87. https://doi.org/10.1038/ngeo1047.

[2] Tresa M. Pollock, Weight Loss with Magnesium Alloys, Science (80-.). 328 (2010) 985–986.

[3] M. Wise, K. Calvin, A. Thomson, L. Clarke, B. Bond-Lamberty, R. Sands, S.J. Smith, A. Janetos, J. Edmonds, Implications of limiting CO2 concentrations for land use and energy, Science (80-.). 324 (2009) 1183–1186. https://doi.org/10.1126/science.1168475.

[4] J. Murray, D. King, Climate policy: Oil's tipping point has passed, Nature. 481 (2012) 433–435. https://doi.org/10.1038/481433a.

[5] W.J. Joost, Reducing vehicle weight and improving U.S. energy efficiency using integrated computational materials engineering, Jom. 64 (2012) 1032–1038. https://doi.org/10.1007/s11837-012-0424-z.

[6] A.A. Luo, Magnesium: Current and potential automotive applications, Jom. 54 (2002) 42–48. https://doi.org/10.1007/BF02701073.

[7] Y.F. Zheng, X.N. Gu, F. Witte, Biodegradable metals, Mater. Sci. Eng. R Reports. 77 (2014) 1–34. https://doi.org/10.1016/j.mser.2014.01.001.

[8] M. Echeverry-Rendon, J.P. Allain, S.M. Robledo, F. Echeverria, M.C. Harmsen, Coatings for biodegradable magnesium-based supports for therapy of vascular disease: A general view, Mater. Sci. Eng. C. 102 (2019) 150–163. https://doi.org/10.1016/j.msec.2019.04.032.

[9] Engineering Materials: Properties and Applications of Metals and Alloys: Chandra P. Sharma: 9788120324480: Amazon.com: Books, (n.d.). https://www.amazon.com/Engineering-Materials-Properties-Applications-Metals/dp/812032448X (accessed November 14, 2020).

[10] Q. Peng, J. Wang, Y. Wu, L. Wang, Microstructures and tensile properties of Mg-8Gd-0.6Zr-xNd-yY (x + y = 3, mass%) alloys, Mater. Sci. Eng. A. 433 (2006) 133–138. https://doi.org/10.1016/j.msea.2006.06.043.

[11] Y. Gao, Q. Wang, J. Gu, Y. Zhao, Y. Tong, Behavior of Mg-15Gd-5Y-0.5Zr alloy during solution heat treatment from 500 to 540 °C, Mater. Sci. Eng. A. 459 (2007) 117–123. https://doi.org/10.1016/j.msea.2007.01.057.

[12] A. Akhtar, E. Teghtsoonian, Solid solution strengthening of magnesium single crystals-ii the effect of solute on the ease of prismatic slip, Acta Metall. 17 (1969) 1351–1356. https://doi.org/10.1016/0001-6160(69)90152-7.

[13] S. Li, A.C. Bacco, N. Birbilis, H. Cong, Passivation and potential fluctuation of Mg alloy AZ31B in alkaline environments, Corros. Sci. 112 (2016) 596–610. https://doi.org/10.1016/j.corsci.2016.08.022.

[14] K. Suzuki, Y. Chino, X. Huang, M. Mabuchi, Elastic and damping properties of AZ31 magnesium alloy sheet processed by high-temperature rolling, Mater. Trans. 52 (2011) 2040–2044. https://doi.org/10.2320/matertrans.L-M2011824.

[15] Y. Chino, K. Kimura, M. Mabuchi, Deformation characteristics at room temperature under biaxial tensile stress in textured AZ31 Mg alloy sheets, Acta Mater. 57 (2009) 1476–1485. https://doi.org/10.1016/j.actamat.2008.11.033.

[16] A. Chapuis, J.H. Driver, Temperature dependency of slip and twinning in plane strain compressed magnesium single crystals, Acta Mater. 59 (2011) 1986–1994. https://doi.org/10.1016/j.actamat.2010.11.064.

[17] S.R. Agnew, C.N. Tomé, D.W. Brown, T.M. Holden, S.C. Vogel, Study of slip mechanisms in a magnesium alloy by neutron diffraction and modeling, Scr. Mater. 48 (2003) 1003–1008. https://doi.org/10.1016/S1359-6462(02)00591-2.

[18] A. Orozco-Caballero, D. Lunt, J.D. Robson, J. Quinta da Fonseca, How magnesium accommodates local deformation incompatibility: A high-resolution digital image correlation study, Acta Mater. 133 (2017) 367–379. https://doi.org/10.1016/j.actamat.2017.05.040.

[19] M.R. Barnett, Twinning and the ductility of magnesium alloys. Part I: “Tension” twins, Mater. Sci. Eng. A. 464 (2007) 1–7. https://doi.org/10.1016/j.msea.2006.12.037.

[20] S.B. Yi, C.H.J. Davies, H.G. Brokmeier, R.E. Bolmaro, K.U. Kainer, J. Homeyer, Deformation and texture evolution in AZ31 magnesium alloy during uniaxial loading, Acta Mater. 54 (2006) 549–562. https://doi.org/10.1016/j.actamat.2005.09.024.

[21] S. Godet, L. Jiang, A.A. Luo, J.J. Jonas, Use of Schmid factors to select extension twin variants in extruded magnesium alloy tubes, Scr. Mater. 55 (2006) 1055–1058. https://doi.org/10.1016/j.scriptamat.2006.07.059.

[22] M.R. Barnett, Twinning and the ductility of magnesium alloys. Part II. “Contraction” twins, Mater. Sci. Eng. A. 464 (2007) 8–16. https://doi.org/10.1016/j.msea.2007.02.109.

[23] H. Fan, J.A. El-Awady, Molecular Dynamics Simulations of Orientation Effects during Tension, Compression, and Bending Deformations of Magnesium Nanocrystals, J. Appl. Mech. Trans. ASME. 82 (2015). https://doi.org/10.1115/1.4030930.

[24] S. Kleiner, P.J. Uggowitzer, Mechanical anisotropy of extruded Mg-6% Al-1% Zn alloy, Mater. Sci. Eng. A. 379 (2004) 258–263. https://doi.org/10.1016/j.msea.2004.02.020.

[25] S. Zheng, Q. Yu, Y. Jiang, An experimental study of fatigue crack propagation in extruded AZ31B magnesium alloy, Int. J. Fatigue. 47 (2013) 174–183. https://doi.org/10.1016/j.ijfatigue.2012.08.010.

[26] H.T. Jeong, T.K. Ha, Texture development in a warm rolled AZ31 magnesium alloy, J. Mater. Process. Technol. 187–188 (2007) 559–561. https://doi.org/10.1016/j.jmatprotec.2006.11.084.

[27] V. Herrera-Solaz, J. Llorca, E. Dogan, I. Karaman, J. Segurado, An inverse optimization strategy to determine single crystal mechanical behavior from

polycrystal tests: Application to AZ31 Mg alloy, Int. J. Plast. 57 (2014) 1–15. https://doi.org/10.1016/j.ijplas.2014.02.001.

[28] C.H.J. Davies, S.B. Yi, J. Bohlen, K.U. Kainer, H.G. Brokmeier, Synchrotron Radiation Investigation of Twinning in Extruded Magnesium Alloy AZ3l, Mater. Sci. Forum. 495–497 (2005) 1633–1638. https://doi.org/10.4028/www.scientific.net/msf.495-497.1633.

[29] F.A. Mirza, D.L. Chen, Fatigue of magnesium alloys, Aerosp. Mater. Handb. (2016) 647–698.

[30] X.Z. Lin, D.L. Chen, Strain controlled cyclic deformation behavior of an extruded magnesium alloy, Mater. Sci. Eng. A. 496 (2008) 106–113. https://doi.org/10.1016/j.msea.2008.05.016.

[31] S. Begum, D.L. Chen, S. Xu, A.A. Luo, Low cycle fatigue properties of an extruded AZ31 magnesium alloy, Int. J. Fatigue. 31 (2009) 726–735. https://doi.org/10.1016/j.ijfatigue.2008.03.009.

[32] Y. Lei, Z. Wang, G. Kang, Experimental investigation on uniaxial cyclic plasticity of cast AZ91 magnesium alloy, J. Magnes. Alloy. (2022). https://doi.org/10.1016/j.jma.2021.12.001.

[33] H.T. Kang, T. Ostrom, Mechanical behavior of cast and forged magnesium alloys and their microstructures, Mater. Sci. Eng. A. 490 (2008) 52–56. https://doi.org/10.1016/j.msea.2008.02.030.

[34] Z. Liu, H.T. Ji, L. Lin, L.J. Chen, W. Wu, L. Yang, Cyclic Deformation Behaviour and Potential Automobile Application of Magnesium Die Casting Alloys AZ91 and AM50, Mater. Sci. Forum. 539–543 (2007) 1626–1631. https://doi.org/10.4028/www.scientific.net/msf.539-543.1626.

[35] L.J. Chen, J. Shen, W. Wu, F. Li, Y. Wang, Z. Liu, Low-Cycle Fatigue Behavior of Magnesium Alloy AZ91, Mater. Sci. Forum. 488–489 (2005) 725–728. https://doi.org/10.4028/www.scientific.net/msf.488-489.725.

[36] Y. Xiong, Q. Yu, Y. Jiang, Cyclic deformation and fatigue of extruded AZ31B

magnesium alloy under different strain ratios, Mater. Sci. Eng. A. 649 (2016) 93–103. https://doi.org/10.1016/j.msea.2015.09.084.

[37] P. Zhang, Z.J. Zhang, L.L. Li, Z.F. Zhang, Twin boundary: Stronger or weaker interface to resist fatigue cracking?, Scr. Mater. 66 (2012) 854–859. https://doi.org/10.1016/j.scriptamat.2012.01.028.

[38] M. Matsuzuki, S. Horibe, Analysis of fatigue damage process in magnesium alloy AZ31, Mater. Sci. Eng. A. 504 (2009) 169–174. https://doi.org/10.1016/j.msea.2008.10.034.

[39] Q. Yu, J. Zhang, Y. Jiang, Q. Li, An experimental study on cyclic deformation and fatigue of extruded ZK60 magnesium alloy, Int. J. Fatigue. 36 (2012) 47–58. https://doi.org/10.1016/j.ijfatigue.2011.08.016.

[40] Z. Li, A.A. Luo, Q. Wang, H. Zou, J. Dai, L. Peng, Fatigue characteristics of sand-cast AZ91D magnesium alloy, J. Magnes. Alloy. 5 (2017) 1–12. https://doi.org/10.1016/j.jma.2017.03.001.

[41] S.M.A.K. Mohammed, D.J. Li, X.Q. Zeng, D.L. Chen, Cyclic deformation behavior of a high zinc-containing cast magnesium alloy, Int. J. Fatigue. 125 (2019) 1–10. https://doi.org/10.1016/j.ijfatigue.2019.03.015.

[42] S.M.H. Karparvarfard, S.K. Shaha, S.B. Behravesh, H. Jahed, B.W. Williams, Fatigue characteristics and modeling of cast and cast-forged ZK60 magnesium alloy, Int. J. Fatigue. 118 (2019) 282–297. https://doi.org/10.1016/j.ijfatigue.2018.03.019.

[43] D. Toscano, S.K. Shaha, B. Behravesh, H. Jahed, B. Williams, Effect of forging on the low cycle fatigue behavior of cast AZ31B alloy, Mater. Sci. Eng. A. 706 (2017) 342–356. https://doi.org/10.1016/j.msea.2017.08.086.

[44] Z. Li, Q. Wang, A.A. Luo, P. Fu, L. Peng, Y. Wang, G. Wu, High cycle fatigue of cast Mg-3Nd-0.2Zn magnesium alloys, Metall. Mater. Trans. A Phys. Metall. Mater. Sci. 44 (2013) 5202–5215. https://doi.org/10.1007/s11661-013-1843-3.

[45] H.A. Patel, N. Rashidi, D.L. Chen, S.D. Bhole, A.A. Luo, Cyclic deformation

behavior of a super-vacuum die cast magnesium alloy, Mater. Sci. Eng. A. 546 (2012) 72–81. https://doi.org/10.1016/j.msea.2012.03.028.

[46] C.H. Cáceres, T. Sumitomo, M. Veidt, Pseudoelastic behaviour of cast magnesium AZ91 alloy under cyclic loading-unloading, Acta Mater. 51 (2003) 6211–6218. https://doi.org/10.1016/S1359-6454(03)00444-0.

[47] A.D. Murphy-Leonard, D.C. Pagan, A. Beaudoin, M.P. Miller, J.E. Allison, Quantification of cyclic twinning-detwinning behavior during low-cycle fatigue of pure magnesium using high energy X-ray diffraction, Int. J. Fatigue. 125 (2019) 314–323. https://doi.org/10.1016/j.ijfatigue.2019.04.011.

[48] J. Koike, N. Fujiyama, D. Ando, Y. Sutou, Roles of deformation twinning and dislocation slip in the fatigue failure mechanism of AZ31 Mg alloys, Scr. Mater. 63 (2010) 747–750. https://doi.org/10.1016/j.scriptamat.2010.03.021.

[49] S.M. Yin, H.J. Yang, S.X. Li, S.D. Wu, F. Yang, Cyclic deformation behavior of as-extruded Mg-3%Al-1%Zn, Scr. Mater. 58 (2008) 751–754. https://doi.org/10.1016/j.scriptamat.2007.12.020.

[50] Z.M. Li, P.H. Fu, L.M. Peng, Y.X. Wang, H.Y. Jiang, G.H. Wu, Comparison of high cycle fatigue behaviors of Mg-3Nd-0.2Zn-Zr alloy prepared by different casting processes, Mater. Sci. Eng. A. 579 (2013) 170–179. https://doi.org/10.1016/j.msea.2013.05.040.

[51] Q.G. Wang, D. Apelian, D.A. Lados, Fatigue behavior of A356-T6 aluminum cast alloys. Part I. Effect of casting defects, J. Light Met. 1 (2001) 73–84. https://doi.org/10.1016/S1471-5317(00)00008-0.

[52] H. Mayer, M. Papakyriacou, B. Zettl, S.E. Stanzl-Tschegg, Influence of porosity on the fatigue limit of die cast magnesium and aluminium alloys, Int. J. Fatigue. 25 (2003) 245–256. https://doi.org/10.1016/S0142-1123(02)00054-3.

[53] M.F. Horstemeyer, N. Yang, K. Gall, D.L. McDowell, J. Fan, P.M. Gullett, High cycle fatigue of a die cast AZ91E-T4 magnesium alloy, Acta Mater. 52 (2004) 1327–1336. https://doi.org/10.1016/j.actamat.2003.11.018.

[54] D.K. Xu, L. Liu, Y.B. Xu, E.H. Han, The fatigue behavior of I-phase containing as-cast Mg-Zn-Y-Zr alloy, Acta Mater. 56 (2008) 985–994. https://doi.org/10.1016/j.actamat.2007.10.057.

[55] G. Eisenmeier, B. Holzwarth, H.W. Höppel, H. Mughrabi, Cyclic deformation and fatique behaviour of the magnesium alloy AZ91, Mater. Sci. Eng. A. 319–321 (2001) 578–582. https://doi.org/10.1016/S0921-5093(01)01105-4.

[56] M.F. Horstemeyer, N. Yang, K. Gall, D. McDowell, J. Fan, P. Gullett, High cycle fatigue mechanisms in a cast AM60B magnesium alloy, Fatigue Fract. Eng. Mater. Struct. 25 (2002) 1045–1056. https://doi.org/10.1046/j.1460-2695.2002.00594.x.

[57] Q.G. Wang, D. Apelian, D.A. Lados, Fatigue behavior of A356/357 aluminum cast alloys. Part II - Effect of microstructural constituents, J. Light Met. 1 (2001) 85–97. https://doi.org/10.1016/S1471-5317(00)00009-2.

[58] Z. Li, P. Fu, L. Peng, E.P. Becker, G. Wu, Influence of solution temperature on fatigue behavior of AM-SC1 cast magnesium alloy, Mater. Sci. Eng. A. 565 (2013) 250–257. https://doi.org/10.1016/j.msea.2012.12.035.

[59] R.A. Siddiqui, S.A. Abdul-Wahab, T. Pervez, Effect of aging time and aging temperature on fatigue and fracture behavior of 6063 aluminum alloy under seawater influence, Mater. Des. 29 (2008) 70–79. https://doi.org/10.1016/j.matdes.2006.12.003.

[60] L.M. Peng, P.H. Fu, Z.M. Li, H.Y. Yue, D.Y. Li, Y.X. Wang, High cycle fatigue behaviors of low pressure cast Mg-3Nd-0.2Zn-2Zr alloys, Mater. Sci. Eng. A. 611 (2014) 170–176. https://doi.org/10.1016/j.msea.2014.05.085.

[61] L. Peng, P. Fu, Z. Li, Y. Wang, H. Jiang, High cycle fatigue properties of cast Mg-xNd-0.2Zn-Zr alloys, J. Mater. Sci. 49 (2014) 7105–7115. https://doi.org/10.1007/s10853-014-8417-7.

[62] H. Yue, P. Fu, L. Peng, Z. Li, J. Pan, W. Ding, Damage morphology study of high cycle fatigued as-cast Mg-3.0Nd-0.2Zn-Zr (wt.%) alloy, Mater. Charact. 111 (2016) 93–105. https://doi.org/10.1016/j.matchar.2015.11.013.

[63] H. El Kadiri, M.F. Horstemeyer, J.B. Jordon, Y. Xue, Fatigue crack growth mechanisms in high-pressure die-cast magnesium alloys, Metall. Mater. Trans. A Phys. Metall. Mater. Sci. 39 (2008) 190–205. https://doi.org/10.1007/s11661-007-9328-x.

[64] S. Hasegawa, Y. Tsuchida, H. Yano, M. Matsui, Evaluation of low cycle fatigue life in AZ31 magnesium alloy, Int. J. Fatigue. 29 (2007) 1839–1845. https://doi.org/10.1016/j.ijfatigue.2006.12.003.

[65] Y. Wang, D. Culbertson, Y. Jiang, An experimental study of anisotropic fatigue behavior of rolled AZ31B magnesium alloy, Mater. Des. 186 (2020) 108266. https://doi.org/10.1016/j.matdes.2019.108266.

[66] Y. Wu, R. Zhu, X. Cai, L. Liu, Fatigue behavior of variable-plane-rolled AZ31 magnesium alloy, Mater. Sci. Eng. A. 650 (2016) 273–280. https://doi.org/10.1016/j.msea.2015.10.054.

[67] Q. Li, Q. Yu, J. Zhang, Y. Jiang, Effect of strain amplitude on tension-compression fatigue behavior of extruded Mg6Al1ZnA magnesium alloy, Scr. Mater. 62 (2010) 778–781. https://doi.org/10.1016/j.scriptamat.2010.01.052.

[68] Y. Xiong, Y. Jiang, Cyclic deformation and fatigue of rolled AZ80 magnesium alloy along different material orientations, Mater. Sci. Eng. A. 677 (2016) 58–67. https://doi.org/10.1016/j.msea.2016.09.031.

[69] C. Wang, T. Luo, Y. Yang, Low cycle fatigue behavior of the extruded AZ80 magnesium alloy under different strain amplitudes and strain rates, J. Magnes. Alloy. 4 (2016) 181–187. https://doi.org/10.1016/j.jma.2016.07.002.

[70] S. Begum, D.L. Chen, S. Xu, A.A. Luo, Strain-controlled low-cycle fatigue properties of a newly developed extruded magnesium alloy, Metall. Mater. Trans. A Phys. Metall. Mater. Sci. 39 (2008) 3014–3026. https://doi.org/10.1007/s11661-008-9677-0.

[71] J.B. Jordon, H.R. Brown, H. El Kadiri, H.M. Kistler, R.L. Lett, J.C. Baird, A.A. Luo, Investigation of fatigue anisotropy in an extruded magnesium alloy, Int. J. Fatigue.

51 (2013) 8–14. https://doi.org/10.1016/j.ijfatigue.2013.01.006.

[72] L. Chen, C. Wang, W. Wu, Z. Liu, G.M. Stoica, L. Wu, P.K. Liaw, Low-cycle fatigue behavior of an As-extruded AM50 magnesium alloy, Metall. Mater. Trans. A Phys. Metall. Mater. Sci. 38 A (2007) 2235–2241. https://doi.org/10.1007/s11661-007-9181-y.

[73] O. Kulyasova, R. Islamgaliev, B. Mingler, M. Zehetbauer, Microstructure and fatigue properties of the ultrafine-grained AM60 magnesium alloy processed by equal-channel angular pressing, Mater. Sci. Eng. A. 503 (2009) 176–180. https://doi.org/10.1016/j.msea.2008.03.057.

[74] F. Wang, J. Dong, Y. Jiang, W. Ding, Cyclic deformation and fatigue of extruded Mg-Gd-Y magnesium alloy, Mater. Sci. Eng. A. 561 (2013) 403–410. https://doi.org/10.1016/j.msea.2012.10.048.

[75] C. Wang, T.J. Luo, J.X. Zhou, Y.S. Yang, Anisotropic cyclic deformation behavior of extruded ZA81M magnesium alloy, Int. J. Fatigue. 96 (2017) 178–184. https://doi.org/10.1016/j.ijfatigue.2016.11.020.

[76] L. Wu, A. Jain, D.W. Brown, G.M. Stoica, S.R. Agnew, B. Clausen, D.E. Fielden, P.K. Liaw, Twinning-detwinning behavior during the strain-controlled low-cycle fatigue testing of a wrought magnesium alloy, ZK60A, Acta Mater. 56 (2008) 688–695. https://doi.org/10.1016/j.actamat.2007.10.030.

[77] Y. Ling, A.A. Roostaei, G. Glinka, H. Jahed, Fatigue of ZEK100-F magnesium alloy: Characterisation and modelling, Int. J. Fatigue. 125 (2019) 179–186. https://doi.org/10.1016/j.ijfatigue.2019.04.001.

[78] A. Jamali, A. Ma, J. Llorca, Scripta Materialia Influence of grain size and grain boundary misorientation on the fatigue crack initiation mechanisms of textured AZ31 Mg alloy, Scr. Mater. 207 (2022) 114304. https://doi.org/10.1016/j.scriptamat.2021.114304.

[79] Q. Yu, J. Zhang, Y. Jiang, Direct observation of twinning-detwinning-retwinning on magnesium single crystal subjected to strain-controlled cyclic tension-compression

in [0 0 0 1] direction, Philos. Mag. Lett. 91 (2011) 757–765. https://doi.org/10.1080/09500839.2011.617713.

[80] S.H. Park, S.G. Hong, W. Bang, C.S. Lee, Effect of anisotropy on the low-cycle fatigue behavior of rolled AZ31 magnesium alloy, Mater. Sci. Eng. A. 527 (2010) 417–423. https://doi.org/10.1016/j.msea.2009.08.044.

[81] S.H. Park, S.G. Hong, J. Yoon, C.S. Lee, Influence of loading direction on the anisotropic fatigue properties of rolled magnesium alloy, Int. J. Fatigue. 87 (2016) 210–215. https://doi.org/10.1016/j.ijfatigue.2016.01.026.

[82] S. Dong, Y. Jiang, J. Dong, F. Wang, W. Ding, Cyclic deformation and fatigue of extruded ZK60 magnesium alloy with aging effects, Mater. Sci. Eng. A. 615 (2014) 262–272. https://doi.org/10.1016/j.msea.2014.07.074.

[83] Y. Xiong, Q. Yu, Y. Jiang, An experimental study of cyclic plastic deformation of extruded ZK60 magnesium alloy under uniaxial loading at room temperature, Int. J. Plast. 53 (2014) 107–124. https://doi.org/10.1016/j.ijplas.2013.07.008.

[84] F. Lv, F. Yang, Q.Q. Duan, Y.S. Yang, S.D. Wu, S.X. Li, Z.F. Zhang, Fatigue properties of rolled magnesium alloy (AZ31) sheet: Influence of specimen orientation, Int. J. Fatigue. 33 (2011) 672–682. https://doi.org/10.1016/j.ijfatigue.2010.10.013.

[85] D.D. Yin, C.J. Boehlert, L.J. Long, G.H. Huang, H. Zhou, J. Zheng, Q.D. Wang, D. Wang, Tension-compression asymmetry and the underlying slip/twinning activity in extruded Mg-Y sheets, Int. J. Plast. 136 (2021) 102878. https://doi.org/10.1016/j.ijplas.2020.102878.

[86] E. Dogan, I. Karaman, G. Ayoub, G. Kridli, Reduction in tension-compression asymmetry via grain refinement and texture design in Mg-3Al-1Zn sheets, Mater. Sci. Eng. A. 610 (2014) 220–227. https://doi.org/10.1016/j.msea.2014.04.112.

[87] Z. Zachariah, S.S. V. Tatiparti, S.K. Mishra, N. Ramakrishnan, U. Ramamurty, Tension-compression asymmetry in an extruded Mg alloy AM30: Temperature and strain rate effects, Mater. Sci. Eng. A. 572 (2013) 8–18.

https://doi.org/10.1016/j.msea.2013.02.023.

[88] H. Zhang, A. Jérusalem, E. Salvati, C. Papadaki, K.S. Fong, X. Song, A.M. Korsunsky, Multi-scale mechanisms of twinning-detwinning in magnesium alloy AZ31B simulated by crystal plasticity modeling and validated via in situ synchrotron XRD and in situ SEM-EBSD, Int. J. Plast. 119 (2019) 43–56. https://doi.org/10.1016/j.ijplas.2019.02.018.

[89] B. Wen, F. Wang, L. Jin, J. Dong, Fatigue damage development in extruded Mg-3Al-Zn magnesium alloy, Mater. Sci. Eng. A. 667 (2016) 171–178. https://doi.org/10.1016/j.msea.2016.05.009.

[90] Q. Yu, J. Zhang, Y. Jiang, Fatigue damage development in pure polycrystalline magnesium under cyclic tension – compression loading, Mater. Sci. Eng. A. 528 (2011) 7816–7826. https://doi.org/10.1016/j.msea.2011.06.064.

[91] J. Segurado, R.A. Lebensohn, J. Llorca, Computational Homogenization of Polycrystals, 1st ed., Elsevier Inc., 2018. https://doi.org/10.1016/bs.aams.2018.07.001.

[92] R. Shi, J. Zheng, T. Li, H. Shou, D. Yin, J. Rao, Quantitative analysis of the deformation modes and cracking modes during low-cycle fatigue of a rolled AZ31B magnesium alloy: The influence of texture, Mater. Sci. Eng. A. 844 (2022) 143103. https://doi.org/10.1016/j.msea.2022.143103.

[93] T. Li, J. Rao, J. Zheng, D. Yin, H. Shou, Y. Zhang, Anisotropic cyclic deformation behavior of an extruded Mg-3Y alloy sheet with rare earth texture, J. Magnes. Alloy. (2022). https://doi.org/10.1016/j.jma.2022.05.010.

[94] F. Wang, J. Dong, M. Feng, J. Sun, W. Ding, Y. Jiang, A study of fatigue damage development in extruded Mg–Gd–Y magnesium alloy, Mater. Sci. Eng. A. 589 (2014) 209–216. https://doi.org/10.1016/j.msea.2013.09.089.

[95] F. Yang, S.M. Yin, S.X. Li, Z.F. Zhang, Crack initiation mechanism of extruded AZ31 magnesium alloy in the very high cycle fatigue regime, Mater. Sci. Eng. A. 491 (2008) 131–136. https://doi.org/10.1016/j.msea.2008.02.003.

[96] Z. Wang, S. Wu, G. Kang, H. Li, Z. Wu, Y. Fu, P.J. Withers, In-situ synchrotron X-ray tomography investigation of damage mechanism of an extruded magnesium alloy in uniaxial low-cycle fatigue with ratchetting, Acta Mater. 211 (2021) 116881. https://doi.org/10.1016/j.actamat.2021.116881.

[97] J.D. Bernard, J.B. Jordon, M.F. Horstemeyer, H. El Kadiri, J. Baird, A.A. Luo, Structure – property relations of cyclic damage in a wrought magnesium alloy, Scr. Mater. 63 (2010) 751–756. https://doi.org/10.1016/j.scriptamat.2010.05.048.

[98] Y.C. Deng, Z.J. Huang, T.J. Li, D.D. Yin, J. Zheng, Quantitative Investigation on the Slip / Twinning Activity and Cracking Behavior During Low-Cycle Fatigue of an Extruded Mg-3Y Sheet, Metall. Mater. Trans. A. 52 (2021) 332–349. https://doi.org/10.1007/s11661-020-06083-7.

[99] Y. Xiong, Y. Jiang, Fatigue of ZK60 magnesium alloy under uniaxial loading, Int. J. Fatigue. 64 (2014) 74–83. https://doi.org/10.1016/j.ijfatigue.2014.02.019.

[100] S. Nemat-Nasser, M. Hori, J.D. Achenbach, Micromechanics: Overall Properties of Heterogeneous Materials, Elsevier Science, 1993. https://books.google.es/books?id=wm8vBQAAQBAJ.

[101] S. Torquato, Random Heterogeneous Materials, 1st ed., Springer New York, NY, 2001. https://doi.org/https://doi.org/10.1007/978-1-4757-6355-3.

[102] J.D. Eshelby, The determination of the elastic field of an ellipsoidal inclusion, and related problems: Proceedings of the Royal Society of London, Series A PRLAAZ 1364-5021, 241, 375–396, Crossref Web Sci. (1957).

[103] Z. Hashin, S. Shtrikman, A variational approach to the theory of the elastic behaviour of multiphase materials, J. Mech. Phys. Solids. 11 (1963) 127–140. https://doi.org/10.1016/0022-5096(63)90060-7.

[104] R. Hill, A self-consistent mechanics of composite materials, J. Mech. Phys. Solids. 13 (1965) 213–222. https://doi.org/10.1016/0022-5096(65)90010-4.

[105] E. Kröner, Berechnung der elastischen Konstanten des Vielkristalls aus den Konstanten des Einkristalls, Zeitschrift Für Phys. 151 (1958) 504–518.

[106] T. Mori, K. Tanaka, Average stress in matrix and average elastic energy of materials with misfitting inclusions, Acta Metall. 21 (1973) 571–574. https://doi.org/10.1016/0001-6160(73)90064-3.

[107] M. Berveiller, A. Zaoui, An extension of the self-consistent scheme to plastically-flowing polycrystals, J. Mech. Phys. Solids. 26 (1978) 325–344. https://doi.org/10.1016/0022-5096(78)90003-0.

[108] R. Hill, Continuum micro-mechanics of elastoplastic polycrystals, J. Mech. Phys. Solids. 13 (1965) 89–101. https://doi.org/10.1016/0022-5096(65)90023-2.

[109] P.P. Castañeda, The effective mechanical properties of nonlinear isotropic composites, J. Mech. Phys. Solids. 39 (1991) 45–71. https://doi.org/10.1016/0022-5096(91)90030-R.

[110] P.P. Castañeda, Exact second-order estimates for the effective mechanical properties of nonlinear composite materials, J. Mech. Phys. Solids. 44 (1996) 827–862. https://doi.org/10.1016/0022-5096(96)00015-4.

[111] G.P. Tandon, G.J. Weng, A Theory of Particle-Reinforced Plasticity, J. Appl. Mech. 55 (1988) 126–135. https://doi.org/10.1115/1.3173618.

[112] J. LLorca, J. Segurado, Three-dimensional multiparticle cell simulations of deformation and damage in sphere-reinforced composites, Mater. Sci. Eng. A. 365 (2004) 267–274. https://doi.org/10.1016/j.msea.2003.09.035.

[113] J. Segurado, C. González, J. LLorca, A numerical investigation of the effect of particle clustering on the mechanical properties of composites, Acta Mater. 51 (2003) 2355–2369. https://doi.org/10.1016/S1359-6454(03)00043-0.

[114] J. Segurado, J. LLorca, Computational micromechanics of composites: The effect of particle spatial distribution, Mech. Mater. 38 (2006) 873–883. https://doi.org/10.1016/j.mechmat.2005.06.026.

[115] C. González, J. LLorca, Mechanical behavior of unidirectional fiber-reinforced polymers under transverse compression: Microscopic mechanisms and modeling, Compos. Sci. Technol. 67 (2007) 2795–2806.

https://doi.org/10.1016/j.compscitech.2007.02.001.

[116] C. González, J. Segurado, J. LLorca, Numerical simulation of elasto-plastic deformation of composites: Evolution of stress microfields and implications for homogenization models, J. Mech. Phys. Solids. 52 (2004) 1573–1593. https://doi.org/10.1016/j.jmps.2004.01.002.

[117] E. Totry, C. González, J. LLorca, Failure locus of fiber-reinforced composites under transverse compression and out-of-plane shear, Compos. Sci. Technol. 68 (2008) 829–839. https://doi.org/10.1016/j.compscitech.2007.08.023.

[118] Y. Liu, P. Ponte Castañeda, Second-order theory for the effective behavior and field fluctuations in viscoplastic polycrystals, J. Mech. Phys. Solids. 52 (2004) 467–495. https://doi.org/10.1016/S0022-5096(03)00078-4.

[119] G. DeBotton, P. Ponte Castaneda, Variational estimates for the creep behaviour of polycrystals, Proc. R. Soc. London, Ser. A Math. Phys. Sci. 448 (1995) 121–142. https://doi.org/10.1098/rspa.1995.0009.

[120] D. Peirce, R.J. Asaro, A. Needleman, An analysis of nonuniform and localized deformation in ductile single crystals, Acta Metall. 30 (1982) 1087–1119. https://doi.org/10.1016/0001-6160(82)90005-0.

[121] R. Quey, L. Renversade, Optimal polyhedral description of 3D polycrystals: Method and application to statistical and synchrotron X-ray diffraction data, Comput. Methods Appl. Mech. Eng. 330 (2018) 308–333. https://doi.org/10.1016/j.cma.2017.10.029.

[122] R. Quey, P.R. Dawson, F. Barbe, Large-scale 3D random polycrystals for the finite element method: Generation, meshing and remeshing, Comput. Methods Appl. Mech. Eng. 200 (2011) 1729–1745. https://doi.org/10.1016/j.cma.2011.01.002.

[123] Romain Quey, Neper, (n.d.). https://neper.info/.

[124] Dream3D, (2018). https://damask.mpie.de.

[125] G.I. Taylor, C.F. Elam, The plastic extension and fracture of aluminium crystals, Proc. R. Soc. London. Ser. A, Contain. Pap. a Math. Phys. Character. 108 (1925) 28–

51. https://doi.org/10.1098/rspa.1925.0057.

[126] G.I. Taylor, C.F. Elam, Bakerian Lecture: The distortion of an aluminium crystal during a tensile test, Proc. R. Soc. London. Ser. A, Contain. Pap. a Math. Phys. Character. 102 (1923) 643–667. https://doi.org/10.1098/rspa.1923.0023.

[127] G.I. Taylor, Plastic Strain in Metals, 1938. https://books.google.es/books?id=I50lAQAAIAAJ.

[128] R. Hill, Generalized constitutive relations for incremental deformation of metal crystals by multislip, J. Mech. Phys. Solids. 14 (1966) 95–102. https://doi.org/10.1016/0022-5096(66)90040-8.

[129] R. Hill, J.R. Rice, Constitutive analysis of elastic-plastic crystals at arbitrary strain, J. Mech. Phys. Solids. 20 (1972) 401–413. https://doi.org/10.1016/0022-5096(72)90017-8.

[130] J.R. Rice, Inelastic constitutive relations for solids: An internal-variable theory and its application to metal plasticity, J. Mech. Phys. Solids. 19 (1971) 433–455. https://doi.org/10.1038/nbt0910-877.

[131] E.H. Lee, D.T. Liu, Finite-strain elastic - Plastic theory with application to plane-wave analysis, J. Appl. Phys. 38 (1967) 19–27. https://doi.org/10.1063/1.1708953.

[132] R.J. Asaro, A. Needleman, Overview no. 42 Texture development and strain hardening in rate dependent polycrystals, Acta Metall. 33 (1985) 923–953. https://doi.org/10.1016/0001-6160(85)90188-9.

[133] D. Peirce, Shear band bifurcations in ductile single crystals, J. Mech. Phys. Solids. 31 (1983) 133–153. https://doi.org/10.1016/0022-5096(83)90047-9.

[134] A. Cuitiño, M. Ortiz, Stress Update Algorithms From Small-Strain, Eng. Comput. 9 (1992) 437–451.

[135] C. Miehe, Exponential map algorithm for stress updates in anisotropic multiplicative elastoplasticity for single crystals, Int. J. Numer. Methods Eng. 39 (1996) 3367–3390.

[136] A. Arsenlis, D.M. Parks, Modeling the evolution of crystallographic dislocation density in crystal plasticity, J. Mech. Phys. Solids. 50 (2002) 1979–2009. https://doi.org/10.1016/S0022-5096(01)00134-X.

[137] K.S. Cheong, E.P. Busso, Discrete dislocation density modelling of single phase FCC polycrystal aggregates, Acta Mater. 52 (2004) 5665–5675. https://doi.org/10.1016/j.actamat.2004.08.044.

[138] A. Ma, F. Roters, D. Raabe, A dislocation density based constitutive model for crystal plasticity FEM including geometrically necessary dislocations, Acta Mater. 54 (2006) 2169–2179. https://doi.org/10.1016/j.actamat.2006.01.005.

[139] D. Peirce, R.J. Asaro, A. Needleman, Material rate dependence and localized deformation in crystalline solids, Acta Metall. 31 (1983) 1951–1976. https://doi.org/10.1016/0001-6160(83)90014-7.

[140] L. Méric, P. Poubanne, G. Cailletaud, Single crystal modeling for structural calculations: Part 1-model presentation, J. Eng. Mater. Technol. Trans. ASME. 113 (1991) 162–170. https://doi.org/10.1115/1.2903374.

[141] G. Cailletaud, A micromechanical approach to inelastic behaviour of metals, Int. J. Plast. 8 (1992) 55–73. https://doi.org/10.1016/0749-6419(92)90038-E.

[142] Z. Hu, E.F. Rauch, C. Teodosiu, Work-hardening behavior of mild steel under stress reversal at large strains, Int. J. Plast. 8 (1992) 839–856. https://doi.org/10.1016/0749-6419(92)90006-X.

[143] S. Mahajan, D.F. Williams, Deformation Twinning in Metals and Alloys, Int. Mater. Rev. 18 (1973) 43–61. https://doi.org/10.1179/imr.1973.18.2.43.

[144] S.R. Kalidindi, Incorporation of Deformation Twinning in Models, Int. J. Plast. 46 (1998) 267–290.

[145] J. Zhang, S.P. Joshi, Phenomenological crystal plasticity modeling and detailed micromechanical investigations of pure magnesium, J. Mech. Phys. Solids. 60 (2012) 945–972. https://doi.org/10.1016/j.jmps.2012.01.005.

[146] G. Proust, C.N. Tomé, G.C. Kaschner, Modeling texture, twinning and hardening

evolution during deformation of hexagonal materials, Acta Mater. 55 (2007) 2137–2148. https://doi.org/10.1016/j.actamat.2006.11.017.

[147] G. Proust, C.N. Tomé, A. Jain, S.R. Agnew, Modeling the effect of twinning and detwinning during strain-path changes of magnesium alloy AZ31, Int. J. Plast. 25 (2009) 861–880. https://doi.org/10.1016/j.ijplas.2008.05.005.

[148] C. Guillemer, M. Clavel, G. Cailletaud, Cyclic behavior of extruded magnesium: Experimental, microstructural and numerical approach, Int. J. Plast. 27 (2011) 2068–2084. https://doi.org/10.1016/j.ijplas.2011.06.002.

[149] H. Qiao, S.R. Agnew, P.D. Wu, Modeling twinning and detwinning behavior of Mg alloy ZK60A during monotonic and cyclic loading, Int. J. Plast. 65 (2015) 61–84. https://doi.org/10.1016/j.ijplas.2014.08.010.

[150] S.R. Kalidindi, C.A. Bronkhorst, L. Anand, Crystallographic texture evolution in bulk deformation processing of FCC metals, J. Mech. Phys. Solids. 40 (1992) 537–569. https://doi.org/10.1007/BF01176030.

[151] N. Ohno, J.D. Wang, Kinematic hardening rules with critical state of dynamic recovery, part I: formulation and basic features for ratchetting behavior, Int. J. Plast. 9 (1993) 375–390. https://doi.org/10.1016/0749-6419(93)90042-O.

[152] F. Briffod, T. Shiraiwa, M. Enoki, Numerical investigation of the influence of twinning/detwinning on fatigue crack initiation in AZ31 magnesium alloy, Mater. Sci. Eng. A. 753 (2019) 79–90. https://doi.org/10.1016/j.msea.2019.03.030.

[153] M. Yaghoobi, J.E. Allison, V. Sundararaghavan, Multiscale modeling of twinning and detwinning behavior of HCP polycrystals, Int. J. Plast. 127 (2020) 102653. https://doi.org/10.1016/j.ijplas.2019.102653.

[154] M. Zhang, H. Zhang, A. Ma, J. Llorca, Experimental and numerical analysis of cyclic deformation and fatigue behavior of a Mg-RE alloy, Int. J. Plast. 139 (2021) 102885. https://doi.org/10.1016/j.ijplas.2020.102885.

[155] H. Wang, P.D. Wu, J. Wang, C.N. Tomé, A crystal plasticity model for hexagonal close packed (HCP) crystals including twinning and de-twinning mechanisms, Int.

J. Plast. 49 (2013) 36–52. https://doi.org/10.1016/j.ijplas.2013.02.016.

[156] C. Paramatmuni, A.K. Kanjarla, A crystal plasticity FFT based study of deformation twinning, anisotropy and micromechanics in HCP materials: Application to AZ31 alloy, Int. J. Plast. 113 (2019) 269–290. https://doi.org/10.1016/j.ijplas.2018.10.007.

[157] T. Tang, G. Zhou, Z. Li, D. Li, L. Peng, Y. Peng, P. Wu, H. Wang, M.G. Lee, A polycrystal plasticity based thermo-mechanical-dynamic recrystallization coupled modeling method and its application to light weight alloys, Int. J. Plast. 116 (2019) 159–191. https://doi.org/10.1016/j.ijplas.2019.01.001.

[158] P.P. Indurkar, S. Baweja, R. Perez, S.P. Joshi, Predicting textural variability effects in the anisotropic plasticity and stability of hexagonal metals: Application to magnesium and its alloys, Int. J. Plast. 132 (2020) 102762. https://doi.org/10.1016/j.ijplas.2020.102762.

[159] M. Yaghoobi, Z. Chen, A.D. Murphy-Leonard, V. Sundararaghavan, S. Daly, J.E. Allison, Deformation twinning and detwinning in extruded Mg-4Al: In-situ experiment and crystal plasticity simulation, Int. J. Plast. 155 (2022) 103345. https://doi.org/10.1016/j.ijplas.2022.103345.

[160] C.F. Gu, L.S. Toth, M. Hoffman, Twinning effects in a polycrystalline magnesium alloy under cyclic deformation, Acta Mater. 62 (2014) 212–224. https://doi.org/10.1016/j.actamat.2013.09.048.

[161] C.F. Gu, L.S. Tóth, Polycrystal modeling of tensile twinning in a Mg alloy during cyclic loading, Scr. Mater. 67 (2012) 673–676. https://doi.org/10.1016/j.scriptamat.2012.07.008.

[162] C. Yu, G. Kang, Q. Kan, Crystal plasticity based constitutive model for uniaxial ratchetting of polycrystalline magnesium alloy, Comput. Mater. Sci. 84 (2014) 63–73. https://doi.org/10.1016/j.commatsci.2013.11.054.

[163] H. Li, C. Yu, G. Kang, Crystal plasticity modeling of the multiaxial ratchetting of extruded AZ31 Mg alloy, Int. J. Plast. 152 (2022) 103242.

https://doi.org/10.1016/j.ijplas.2022.103242.

[164] X. Guo, Y. Cheng, Y. Xin, W. Wu, C. Ma, K. An, P.K. Liaw, P. Wu, Q. Liu, Crystal plasticity modeling of low-cycle fatigue behavior of an Mg-3Al-1Zn alloy based on a model, including twinning and detwinning mechanisms, J. Mech. Phys. Solids. 168 (2022) 1–16. https://doi.org/10.1016/j.jmps.2022.105030.

[165] M. Yaghoobi, S. Ganesan, S. Sundar, A. Lakshmanan, S. Rudraraju, J.E. Allison, V. Sundararaghavan, PRISMS-Plasticity: An open-source crystal plasticity finite element software, Comput. Mater. Sci. 169 (2019) 109078. https://doi.org/10.1016/j.commatsci.2019.109078.

[166] D.L. McDowell, F.P.E. Dunne, Microstructure-sensitive computational modeling of fatigue crack formation, Int. J. Fatigue. 32 (2010) 1521–1542. https://doi.org/10.1016/j.ijfatigue.2010.01.003.

[167] A. Pineau, D.L. McDowell, E.P. Busso, S.D. Antolovich, Failure of metals II: Fatigue, Acta Mater. 107 (2016) 484–507. https://doi.org/10.1016/j.actamat.2015.05.050.

[168] A. Cruzado, J. LLorca, J. Segurado, Modeling cyclic deformation of inconel 718 superalloy by means of crystal plasticity and computational homogenization, Int. J. Solids Struct. 122–123 (2017) 148–161. https://doi.org/10.1016/j.ijsolstr.2017.06.014.

[169] A. Manonukul, F.P.E. Dunne, High- and low-cycle fatigue crack initiation using polycrystal plasticity, Proc. R. Soc. A Math. Phys. Eng. Sci. 460 (2004) 1881–1903. https://doi.org/10.1098/rspa.2003.1258.

[170] D.L. McDowell, K. Gall, M.F. Horstemeyer, J. Fan, Microstructure-based fatigue modeling of cast A356-T6 alloy, Eng. Fract. Mech. 70 (2003) 49–80. https://doi.org/10.1016/S0013-7944(02)00021-8.

[171] C.A. Sweeney, B. O'Brien, P.E. McHugh, S.B. Leen, Experimental characterisation for micromechanical modelling of CoCr stent fatigue, Biomaterials. 35 (2014) 36–48. https://doi.org/10.1016/j.biomaterials.2013.09.087.

[172] C.A. Sweeney, B. O'Brien, F.P.E. Dunne, P.E. McHugh, S.B. Leen, Strain-gradient

modelling of grain size effects on fatigue of CoCr alloy, Acta Mater. 78 (2014) 341–353. https://doi.org/10.1016/j.actamat.2014.06.044.

[173] C.A. Sweeney, P.E. McHugh, J.P. McGarry, S.B. Leen, Micromechanical methodology for fatigue in cardiovascular stents, Int. J. Fatigue. 44 (2012) 202–216. https://doi.org/10.1016/j.ijfatigue.2012.04.022.

[174] A.M. Korsunsky, D. Dini, F.P.E. Dunne, M.J. Walsh, Comparative assessment of dissipated energy and other fatigue criteria, Int. J. Fatigue. 29 (2007) 1990–1995. https://doi.org/10.1016/j.ijfatigue.2007.01.007.

[175] V.V.C. Wan, J. Jiang, D.W. MacLachlan, F.P.E. Dunne, Microstructure-sensitive fatigue crack nucleation in a polycrystalline Ni superalloy, Int. J. Fatigue. 90 (2016) 181–190. https://doi.org/10.1016/j.ijfatigue.2016.04.013.

[176] M. Anahid, M.K. Samal, S. Ghosh, Dwell fatigue crack nucleation model based on crystal plasticity finite element simulations of polycrystalline titanium alloys, J. Mech. Phys. Solids. 59 (2011) 2157–2176. https://doi.org/10.1016/j.jmps.2011.05.003.

[177] M.D. Sangid, H.J. Maier, H. Sehitoglu, An energy-based microstructure model to account for fatigue scatter in polycrystals, J. Mech. Phys. Solids. 59 (2011) 595–609. https://doi.org/10.1016/j.jmps.2010.12.014.

[178] D. Ozturk, A. Shahba, S. Ghosh, Crystal plasticity FE study of the effect of thermo-mechanical loading on fatigue crack nucleation in titanium alloys, Fatigue Fract. Eng. Mater. Struct. 39 (2016) 752–769. https://doi.org/10.1111/ffe.12410.

[179] V.P. Bennett, D.L. McDowell, Polycrystal orientation distribution effects on microslip in high cycle fatigue, Int. J. Fatigue. 25 (2002) 27–39. https://doi.org/10.1016/S0142-1123(02)00057-9.

[180] G.M. Castelluccio, D.L. McDowell, Mesoscale modeling of microstructurally small fatigue cracks in metallic polycrystals, Mater. Sci. Eng. A. 598 (2014) 34–55. https://doi.org/10.1016/j.msea.2014.01.015.

[181] G.M. Castelluccio, D.L. McDowell, A mesoscale approach for growth of 3D

microstructurally small fatigue cracks in polycrystals, Int. J. Damage Mech. 23 (2014) 791–818. https://doi.org/10.1177/1056789513513916.

[182] W.D. Musinski, D.L. McDowell, Microstructure-sensitive probabilistic modeling of HCF crack initiation and early crack growth in Ni-base superalloy IN100 notched components, Int. J. Fatigue. 37 (2012) 41–53. https://doi.org/10.1016/j.ijfatigue.2011.09.014.

[183] E. CHARKALUK, B. A, C. A, D. VAN K, Fatigue design of structures under thermomechanical loadings, Fatigue Fract. Eng. Mater. Struct. 26 (2003) 661–661. https://doi.org/10.1046/j.1460-2695.2002.00613.x-i1.

[184] M. Shenoy, J. Zhang, D.L. Mcdowell, Estimating fatigue sensitivity to polycrystalline Ni-base superalloy microstructures using a computational approach, (2007) 889–904. https://doi.org/10.1111/j.1460-2695.2007.01159.x.

[185] F.J. Humphreys, Characterisation of fine-scale microstructures by electron backscatter diffraction (EBSD), Scr. Mater. 51 (2004) 771–776. https://doi.org/10.1016/j.scriptamat.2004.05.016.

[186] A.J. Schwartz, M. Kumar, B.L. Adams, D.P. Field, Electron backscatter diffraction in materials science, 2009. https://doi.org/10.1007/978-0-387-88136-2.

[187] F. Bachmann, R. Hielscher, H. Schaeben, Texture analysis with MTEX- Free and open source software toolbox, Solid State Phenom. 160 (2010) 63–68. https://doi.org/10.4028/www.scientific.net/SSP.160.63.

[188] C.M. Cepeda-Jiménez, J.M. Molina-Aldareguia, M.T. Pérez-Prado, EBSD-Assisted Slip Trace Analysis During In Situ SEM Mechanical Testing: Application to Unravel Grain Size Effects on Plasticity of Pure Mg Polycrystals, Jom. 68 (2016) 116–126. https://doi.org/10.1007/s11837-015-1521-6.

[189] T.R. Bieler, R. Alizadeh, M. Peña-Ortega, J. Llorca, An analysis of (the lack of) slip transfer between near-cube oriented grains in pure Al, Int. J. Plast. 118 (2019) 269–290. https://doi.org/10.1016/j.ijplas.2019.02.014.

[190] R. Alizadeh, M. Peña-ortega, T.R. Bieler, J. LLorca, Scripta Materialia A criterion

for slip transfer at grain boundaries in Al, Scr. Mater. 178 (2020) 408–412. https://doi.org/10.1016/j.scriptamat.2019.12.010.

[191] T.R. Bieler, P. Eisenlohr, F. Roters, D. Kumar, D.E. Mason, M.A. Crimp, D. Raabe, The role of heterogeneous deformation on damage nucleation at grain boundaries in single phase metals, Int. J. Plast. 25 (2009) 1655–1683. https://doi.org/10.1016/j.ijplas.2008.09.002.

[192] D. Xia, X. Chen, G. Huang, B. Jiang, A. Tang, H. Yang, S. Gavras, Y. Huang, N. Hort, F. Pan, Calculation of Schmid factor in Mg alloys: Influence of stress state, Scr. Mater. 171 (2019) 31–35. https://doi.org/10.1016/j.scriptamat.2019.06.014.

[193] A. Javaid, F. Czerwinski, Effect of hot rolling on microstructure and properties of the ZEK100 alloy, J. Magnes. Alloy. 7 (2019) 27–37. https://doi.org/10.1016/j.jma.2019.02.001.

[194] L.L.C. Catorceno, H.F.G. de Abreu, A.F. Padilha, Effects of cold and warm cross-rolling on microstructure and texture evolution of AZ31B magnesium alloy sheet, J. Magnes. Alloy. 6 (2018) 121–133. https://doi.org/10.1016/j.jma.2018.04.004.

[195] Y.N. Wang, C.I. Chang, C.J. Lee, H.K. Lin, J.C. Huang, Texture and weak grain size dependence in friction stir processed Mg-Al-Zn alloy, Scr. Mater. 55 (2006) 637–640. https://doi.org/10.1016/j.scriptamat.2006.06.005.

[196] Y. Uematsu, T. Kakiuchi, S. Tamano, S. Mizuno, K. Tamada, Fatigue behavior of AZ31 magnesium alloy evaluated using single crystal micro cantilever specimen, Int. J. Fatigue. 93 (2016) 30–37. https://doi.org/10.1016/j.ijfatigue.2016.08.008.

[197] Z. Xing, H. Fan, J. Tang, B. Wang, G. Kang, Molecular dynamics simulation on the cyclic deformation of magnesium single crystals, Comput. Mater. Sci. 186 (2021) 110003. https://doi.org/10.1016/j.commatsci.2020.110003.

[198] T. Li, J. Zheng, H. Shou, R. Shi, Y. Zhang, G. Wen, K. Huang, D. Yin, J. Rao, The deformation modes and transferability during low-cycle fatigue of Mg and Mg–3Y alloy, Mater. Sci. Eng. A. 839 (2022) 142838. https://doi.org/10.1016/j.msea.2022.142838.

[199] D.D. Yin, Q.D. Wang, C.J. Boehlert, Z. Chen, H.M. Li, R.K. Mishra, A. Chakkedath, In-Situ Study of the Tensile Deformation and Fracture Modes in Peak-Aged Cast Mg-11Y-5Gd-2Zn-0.5Zr (Weight Percent), Metall. Mater. Trans. A Phys. Metall. Mater. Sci. 47 (2016) 6438–6452. https://doi.org/10.1007/s11661-016-3709-y.

[200] Q. Yu, J. Zhang, Y. Jiang, Fatigue damage development in pure polycrystalline magnesium under cyclic tension-compression loading, Mater. Sci. Eng. A. 528 (2011) 7816–7826. https://doi.org/10.1016/j.msea.2011.06.064.

[201] C. Geuzaine, J.-F. Remacle, Gmsh: A 3-D finite element mesh generator with built-in pre- and post-processing facilities, Int. J. Numer. Methods Eng. 79 (2009) 1309–1331. https://doi.org/https://doi.org/10.1002/nme.2579.

[202] A. Fernández, M.T. Pérez Prado, Y. Wei, A. Jérusalem, Continuum modeling of the response of a Mg alloy AZ31 rolled sheet during uniaxial deformation, Int. J. Plast. 27 (2011) 1739–1757. https://doi.org/10.1016/j.ijplas.2011.05.002.

[203] V. Herrera-Solaz, P. Hidalgo-Manrique, M.T. Pérez-Prado, D. Letzig, J. Llorca, J. Segurado, Effect of rare earth additions on the critical resolved shear stresses of magnesium alloys, Mater. Lett. 128 (2014) 199–203. https://doi.org/10.1016/j.matlet.2014.04.144.

[204] L. Song, B. Wu, L. Zhang, X. Du, Y. Wang, C. Esling, M.J. Philippe, Detwinning-related Bauschinger effect of an extruded magnesium alloy AZ31B, Mater. Charact. 148 (2019) 63–70. https://doi.org/10.1016/j.matchar.2018.12.005.

[205] B.L. Wu, G.S. Duan, X.H. Du, L.H. Song, Y.D. Zhang, M.J. Philippe, C. Esling, In situ investigation of extension twinning-detwinning and its effect on the mechanical behavior of AZ31B magnesium alloy, Mater. Des. 132 (2017) 57–65. https://doi.org/10.1016/j.matdes.2017.06.023.

[206] L. Wu, S.R. Agnew, D.W. Brown, G.M. Stoica, B. Clausen, A. Jain, Internal stress relaxation and load redistribution during the twinning – detwinning-dominated cyclic deformation of a wrought magnesium alloy , ZK60A, 56 (2008) 3699–3707. https://doi.org/10.1016/j.actamat.2008.04.006.

[207] G.M. Castelluccio, D.L. Mcdowell, Microstructure and mesh sensitivities of mesoscale surrogate driving force measures for transgranular fatigue cracks in polycrystals, Mater. Sci. Eng. A. 639 (2015) 626–639. https://doi.org/10.1016/j.msea.2015.05.048.

[208] A. Cruzado, S. Lucarini, J. LLorca, J. Segurado, Microstructure-based fatigue life model of metallic alloys with bilinear Coffin-Manson behavior, Int. J. Fatigue. 107 (2018) 40–48. https://doi.org/10.1016/j.ijfatigue.2017.10.014.